

Award Accounts

The Chemical Society of Japan Award for 2002

"Mechanics" of Molecular Assembly: Real-Time and In-Situ Analysis of Nano-to-Mesoscopic Scale Hierarchical Structures and Nonequilibrium Phenomena

Takeji Hashimoto

Department of Polymer Chemistry, Graduate School of Engineering, Kyoto University, Katsura, Kyoto 615-8510

Received May 12, 2004; E-mail: hashimoto@alloy.polym.kyoto-u.ac.jp

We have presented studies of the mechanics of molecular assembly for multicomponent molecular systems in the context of nonlinear and nonequilibrium phenomena. The studies cover the following three themes: (i) elucidation of space-time self-assembly of hierarchical structures, in the length scale ranging from nm to μm, of binary molecular mixtures via phase transition by means of real-time and in-situ analyses with various scattering methods and microscopy methods; (ii) elucidation of self-assembly of molecular mixtures under shear flow in the context of open nonequilibrium phenomena by means of newly developed rheo-optical methods, leading us to discover new dissipative structures as well as shear-induced phase transitions both from single-phase to two-phase and from two-phase to single-phase; (iii) elucidation of the influences of chemical bonds between different component polymers in block copolymers on microphase transition and ordered microdomain structures with nano-scale periodicity and various space-group symmetries and exploration of nano-fabrication methods of microdomain structures as templates in the context of nano-science and nano-technology of block copolymers. In each of the three themes, we highlight and emphasize the fact that polymer systems provide very good model systems for basic studies of nonlinear and nonequilibrium phenomena because of the fact that large structures evolve very slowly in polymer systems. The studies may give perspectives for creating advanced soft materials responsive to environmental stimuli and for understanding activities, adaptation, and evolution of living organisms.

1. Introduction and Objectives of This Study

Chemistry is a science of matter concerned with studies of reactions and syntheses of new molecules, characterization of molecules themselves, and studies of the structure-properties relationships of matter comprised of molecules. In this article we are concerned with structures and properties of a class of matter called "**soft-matters**" (or "**complex liquids**") such as polymers, liquid crystals, membranes, gels, micelles, colloids, supercooled liquids, multi-component liquids, etc. The soft matters are assemblies of molecules and/or supramolecules which commonly have characteristic self-assembled structures and have properties in between solids and liquids, depending on a space-time scale of observations. The self-assembled structures generally have **hierarchical structures** with a length scale ranging from nm to mm; they have various levels of structures which change in response to changes in relatively weak physical interactions among their constituent molecules (typically less than $\sim$20 k_BT or $\sim$10 kcal/mol), caused by changes in environmental variables such as temperature (T), pressure (P), pH, etc. The changes in various level of structures are well expected to be intricately coupled, the cooperativity of which involves dynamics with a time scale ranging from nano seconds to seconds or periods even longer than hours.

We focus on **in-situ** and **real-time** analysis of dynamics and patterns of hierarchical structures at the various space-time scales described above by means of various Fourier-space (scattering) analyses and real-space (microscopic) analyses, as will be detailed later. It is still very important to explore and clarify the dynamics and pattern formation of each level of structure in the hierarchy. However we believe it is more important, as future work, to unveil general principles underlying the cooperative dynamics and pattern formation of various levels of structures and the hierarchical structure as a whole. Explorations of the principles will eventually lead us to establish **mechanics (dynamics, kinematics, statics) of molecular assemblies** having various hierarchical structures.

The mechanics of molecular assembly may predict a series of space-time events in the structure, which is induced by changes in environmental parameters. The mechanics, which belongs to **nonlinear and nonequilibrium sciences**, will give fundamental information to develop soft materials responsive to environmental stimuli and to understand some activities of living organisms and bodies.

Figure 1 schematically summarizes an outline of our objec-

Published on the web January 13, 2005; DOI 10.1246/bcsj.78.1

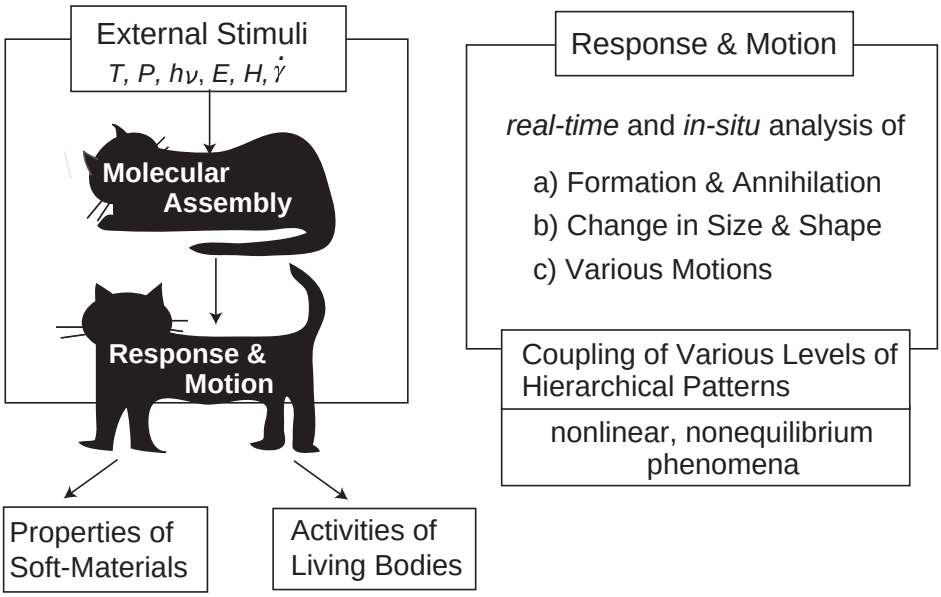

Fig. 1. Schematic representation of a concept on mechanics of molecular assembly.

tives as described above. The molecular assembly self-organizes and responds not only to changes in the environmental variables (T, P) but also to various external stimuli such as flow and deformation (strain rate $\dot{\gamma}$ and strain γ) chemical reactions, electric (E) and magnetic (H) fields, light ($h\nu$), etc. Information concerning the self-organization, the response and the motion of the molecular assembly provides a key for understanding not only adaptation and evolution of living organisms and bodies but also properties of soft-materials. Fundamental studies along this line would make a contribution to the physical science of "**open nonequilibrium systems**", i.e., systems open to various external energy flows as described above. As for the response and motion of the molecular assembly, we explore formation and annihilation of the assembly, changes in size and shape of the assembly, and various motions of the assembly in the light of *real-time* and *in-situ* experiments and of recently developed theories and computational methods.

2. Scope and Background

We shall focus on the following three research themes in this article:

(a) self-assembly of molecular mixtures,
(b) self-assembly of molecular mixtures under external fields,
(c) self-assembly of block copolymer systems.

The themes are schematically summarized in Figs. 2a to c. Theme (a) involves explorations of phase separation processes and time-evolution of phase-separated structures. Compared to equilibrium structures (single-phase and two-phase structures), the nonequilibrium structures and processes have been left relatively unexplored, except for a series of studies limited to very near critical points, which are known as **critical phenomena**. We have started to explore unsolved problems by using "symmetric" **polymer mixtures as a model system** and have succeeded in obtaining much new information, some of which shall be discussed in sec. 3.

Theme (b) involves explorations of effects of external fields, specifically applied simple shear flow, on equilibrium mixtures either at single-phase states or two-phase states. Almost no quantitative and systematic studies have been reported on **dissipative structures**, which are defined as ordered structures developed in open nonequilibrium systems, except for pioneering works by Silverberg et al.,[1] Verstrate et al.,[2] and Beysens et al.[3] We have elucidated shear-induced two-phase to single-phase transitions for "**symmetric mixtures**" as well as single-phase to two-phase transitions for "**asymmetric mixtures**". We have elucidated the dissipative structures developed in each system as well, through a series of pioneering rheo-optical works, as will be discussed in sec. 4.

The block copolymers, for example A-*b*-B diblock copolymers, to be discussed in theme (c) are comprised of A and B macromolecules covalently bonded at one of their chain ends. Here we focus on **effects of the single covalent bonds** in A-*b*-B on the self-assembly of two component systems of A and B block polymers. Owing to this single covalent bond, the block polymers A and B can be phase-separated only in the microscopic scale, but not in the macroscopic scale. Hence the phase separations in block copolymers have been traditionally called "microphase separations". The microphase-separated (ordered) states appear, in macroscopic scale, to be identical to single-phase (disordered) states, where A and B block copolymers are molecularly mixed. The differences of the two states are discerned only in the microscopic scale as shown schematically in part (c), which is quite different from macroscopic phase separation of mixtures of A and B polymers, as shown schematically in part (a). Since the copolymerization into block copolymers was first reported by Szwarc in 1956,[4] block copolymer research on structures and properties has been directed toward industrial applications until about 1966. No fundamental and systematic studies have been reported on the microphase-separated structures and microphase transitions. We shall illuminate the influences of the single covalent bond in block copolymers on the microphase transitions and micro-

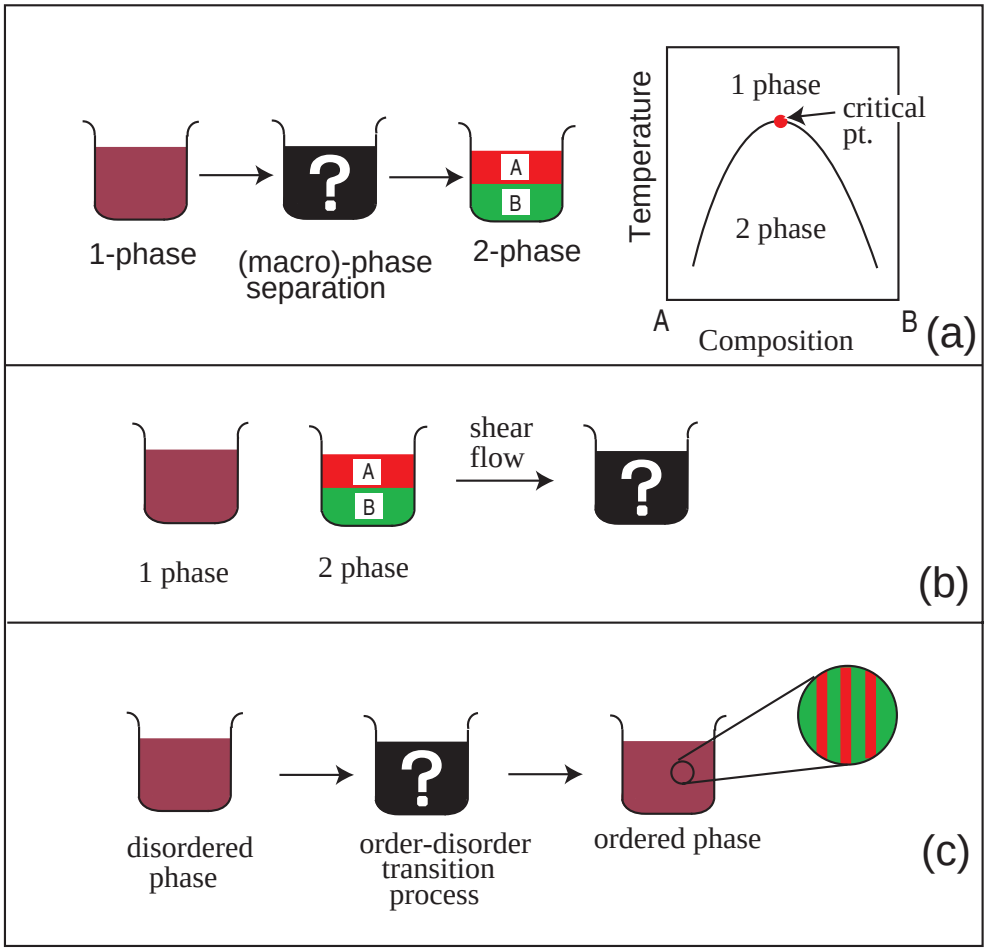

Fig. 2. Three research items to be covered; (a) self-assembly of molecular mixtures, (b) self-assembly of molecular mixtures under simple shear flow, and (c) self-assembly of block copolymer systems.

phase-separated structures in sec. 5.

3. Self-Assembly of Molecular Mixtures

3.1 Motivation. Phase separation processes of two-component molecular mixtures via **spinodal decomposition**[5–7] (SD) involve intriguing fundamental nonequilibrium problems, in chemical physics and physical chemistry, concerning time-evolution of phase-separated structures for thermodynamically unstable systems. Nevertheless, the studies have faced experimental difficulties attributed to the fact that the time evolution is generally too fast to be precisely followed. Some difficulties, however, have been *partially* solved by applying principles established in **critical phenomena**[8,9] to the experiments. The space-time scale of mixtures depends on ΔT, which is defined to be the difference between experimental temperature T and critical temperature T_c,

$$\Delta T \equiv |T - T_c|. \tag{1}$$

As ΔT decreases, as shown in the direction of the large arrows in Fig. 3, the space-time scale of mixtures expands so that large-scale structures evolve or relax slowly with time in the case when $T < T_c$ or $T > T_c$, respectively.[8–10] This is well known as **critical divergence** in space and **critical slowing down** in time.

The space and time scales of mixtures, defined by ξ and t_c, respectively, are related to those of the molecules themselves comprising the mixtures, defined by ξ_0 and t_0 respectively,[8–10]

$$\xi = \xi_0 \varepsilon_T^{-\nu}, \quad t_c = t_0 \varepsilon_T^{-\gamma} \tag{2}$$

where ν and γ are the critical exponents, e.g., $\nu = 1/2$ and $\gamma = 2$ for the mean-field approximation.[9] Here we assume that the component molecules are symmetric in terms of size (ξ_0) and dynamics (self-diffusion coefficient related to t_0). ε_T is defined by

$$\begin{aligned} \varepsilon_T &= |\chi - \chi_s|/\chi_s, \\ &= \begin{cases} \sim \Delta T & \text{when } T \cong T_c, \\ \sim 1 & \text{when } T \gg T_c \quad \text{or} \quad T \ll T_c. \end{cases} \end{aligned} \tag{3}$$

Here χ is a thermodynamic interaction parameter of the component molecules for low molecular weight molecules or segments for polymers[11] and is given by $\chi = s + h/T$, with s and h being constants independent of T.

Figure 4 shows time evolution of light scattering (LS) profiles during phase separation for critical mixtures of simple liquids of 2,6-lutidine and water (L/W) reported by Chou-Goldburg;[12] this is one of the famous experimental results in the field of critical phenomena. Very near critical points, e.g., at the temperature lower than critical point by only 0.6

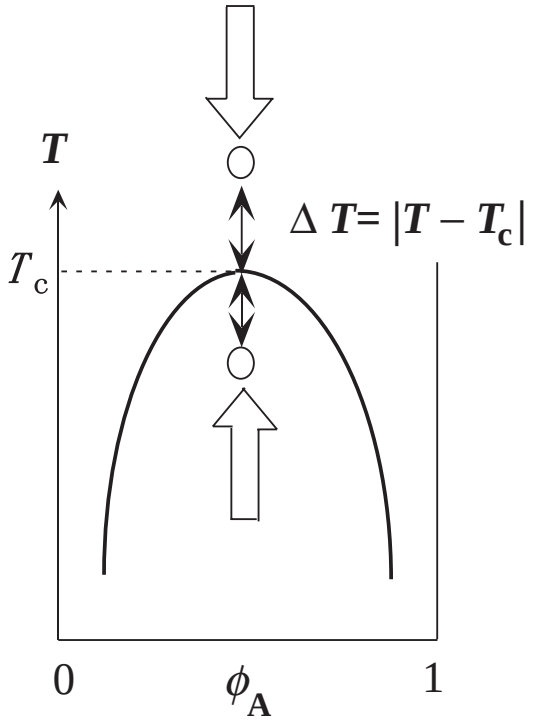

Fig. 3. Schematic phase diagram for symmetric binary molecular mixtures. The arrows indicate directions toward critical temperature T_c, along which the space-time scale of mixtures expands, leading to critical divergence in space-wise and critical slowing down in time-wise.

mK, the phase separation occurs at a large length scale, from about 8 to 30 μm, and a sufficiently slow temporal scale so that one can follow the process through time changes in LS profiles, $I(q,t)$, in the time scale of 45 s to 455 s, as shown in part (a). As the phase-separating structure grows and its characteristic length Λ_m grows with t, the magnitude of the scattering vector defined by $q = (4\pi/\lambda)\sin(\theta/2)$ (where λ and θ are the wavelength of light and the scattering angle in the medium, respectively) at the maximum scattering intensity, q_m ($= 2\pi/\Lambda_m$), decreases with time, as shown in part (a). If only the length scale changes but the shape of the structure is kept unchanged in the phase separation process, the scattering function obtained at various t values (part a) can be scaled with this length scale Λ_m or with the wave number q_m. The structure factor scaled with $q_m(t)$, $F(x) \equiv q_m{}^3(t)I(q,t)$ with $x \equiv q/q_m(t)$, should then becomes universal with time t, as shown in part (b). This "**universal scaled structure factor**" $F(x)$ characterizes the shape of the structure growing with **dynamical self-similarity**.[13] This is typically found in the late stage SD process[8,10,13–16] where each of existing domains attains the equilibrium composition in the system.

The results and conclusion described above serve as a milestone for the nonequilibrium phenomenon, suggesting the existence of general laws in the nonequilibrium process. One can further advance the analysis by raising and solving the following questions: (i) what are the universal form of phase-separating structures inferred by $F(x)$?; (ii) Can one obtain $F(x)$ over a much wider range of reduced scattering vector x in order to unveil the phase-separating structures very precisely at various length scales, global structures to local structures? (iii) Is the law applicable to systems apart from the critical point? To address point (i), it is crucial to construct 3d real-

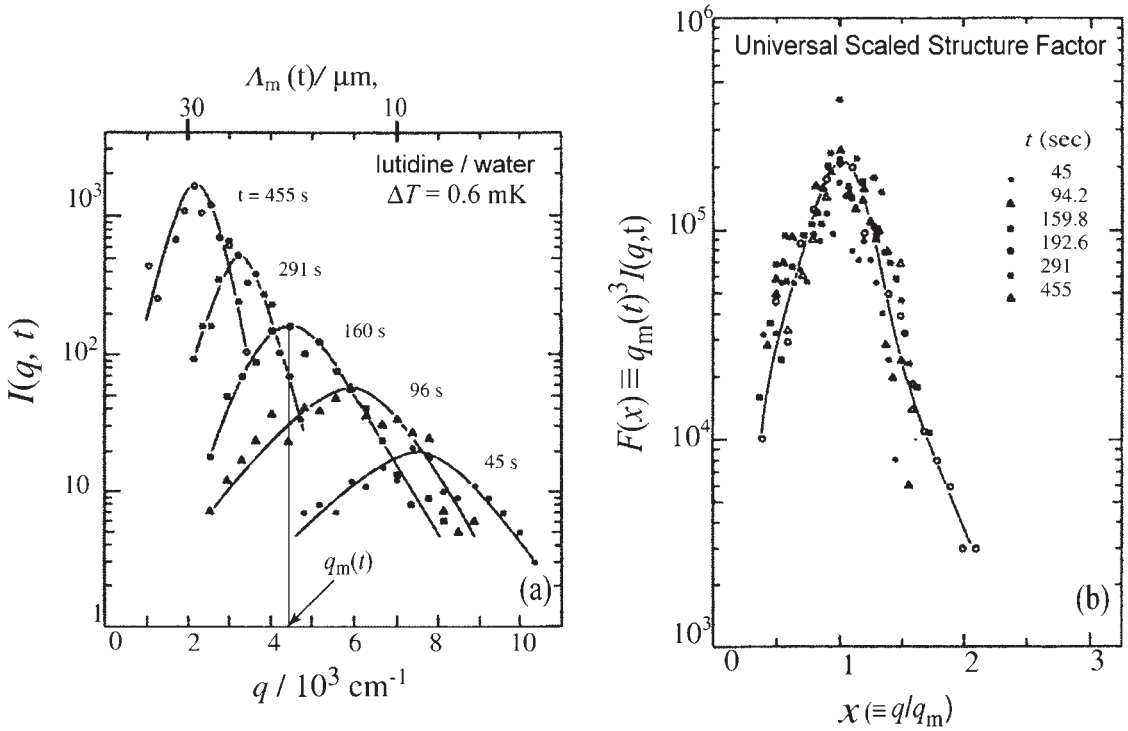

Fig. 4. Time-evolution of light scattering profiles $I(q,t)$ in the late stage spinodal decomposition for the critical mixture of 2,6-lutidine and water (a) and the corresponding scaled structure factor $F(x)$ (b) (data based on the work by Chou–Goldburg[12]).

space phase-separating structures. To address point (ii), one needs to measure scattering over a much wider q by changing θ and λ, which invariably requires experimentation on systems having slow dynamics. The same requirement should be satisfied to address point (iii), because small structures grow very rapidly under conditions apart from critical point in two-phase region, e.g., as T decreases from T_c, as is clear from Eqs. 2 and 3. In order to solve these problems or difficulties, one can select polymers as model systems.

3.2 Strategy of Using Polymers. Let us assume a symmetric polymer pair with equal statistical segment length a, segment number N, and self-diffusion coefficient D_p. Let us define ξ_0 and t_0 for polymers as $\xi_{0,p}$ and $t_{0,p}$, respectively, and for small molecular as $\xi_{0,s}$ and $t_{0,s}$, respectively. Based upon Gaussian chain statistics of single polymer chains[11] in melt and reptation dynamics for entangled polymer melts,[17,18]

$$\xi_{0,p} = N^{1/2}a = N^{1/2}\xi_{0,s}, \tag{4}$$

$$D_p = D_s N_e N^{-2}, \tag{5}$$

where D_s is the self-diffusion coefficient of the segment, and N_e is the number of segments between entanglement couplings.[19] From Eqs. 4 and 5, we obtain

$$t_{0,p} = {\xi_{0,p}}^2/D_p = (N^3/N_e)t_{0,s}, \quad t_{0,s} = a^2/D_s. \tag{6}$$

In the case when $N = 10^4$ and $N_e = 10^2$ as may be typical for high polymers, we obtain

$$\xi_{0,p} = 10^2\xi_{0,s}, \quad t_{0,p} = 10^{10}t_{0,s}, \tag{7}$$

which is highlighted schematically in Fig. 5. Note that $N = N_e = 1$ for small molecules. Hence $\xi_{0,p}$, $t_{0,p}$, and D_p are reduced to $\xi_{0,s}$, $t_{0,s}$, and D_s, respectively, the quantities relevant to small molecules.

Thus the space-time scale of typical polymer systems is extremely large compared with that of small-molecule systems, which gives an important consequence: that in polymer mixtures "**larger structures evolve very slowly**" at a given ΔT. This result would facilitate quantitative and precise experimental investigation of nonequilibrium dynamics and processes for molecular mixtures by using polymer systems as model systems even in regions apart from critical points.

If we set our experimental conditions with polymer systems such that the space-time scale of our observation is much larger than that of polymer molecules themselves, we anticipate that the dynamics and pattern formation processes of polymer mixtures would be similar to those of small-molecule mixtures, except for the extraordinary expansion of the space-time

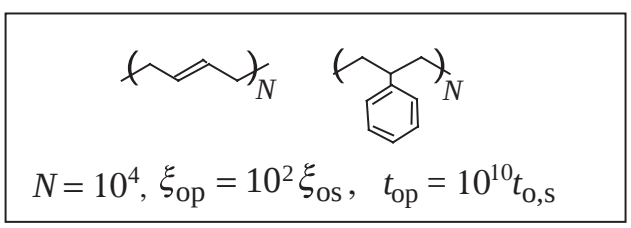

Fig. 5. Characteristic length scale and time scale of symmetric molecules (ξ_0, t_0): comparison of (ξ_0, t_0) for polymers defined by (ξ_{0p}, t_{0p}) and that for small molecules defined by (ξ_{0s}, t_{0s}).

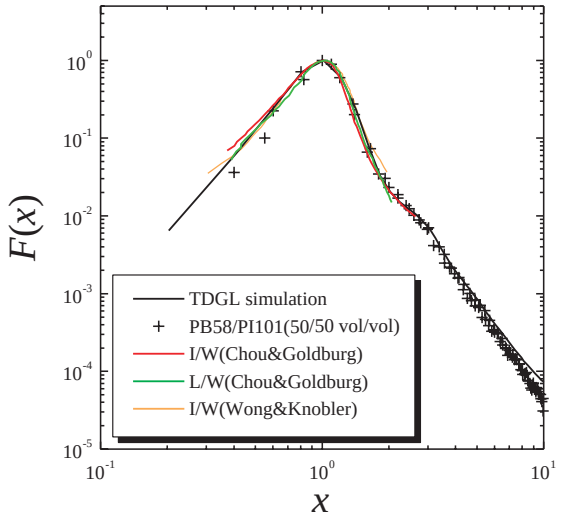

Fig. 6. Comparisons of scaled structure factors, $F(x)$, obtained for critical mixtures of simple liquids (I/W and L/W), polymer mixture (PB/PI, 50/50 vol/vol), and 3d simulation based upon the generalized TDGL equation with a system size of 128^3 (data based on the work of Ref. 10).

scale in polymers. If we set the space-time scale of observation to be comparable with or less than that of polymer molecules, we would anticipate unique features of polymers that cannot be expected for small molecules. A good example of the latter case is a q-dependence of the Onsager kinetic coefficient at $r \leq R_g$ or $q \geq 1/R_g$ as elaborated by de Gennes–Pincus,[20,21] Binder,[22] and Akcasu[23] where R_g is the radius of gyration of a polymer.[11]

The scaled structure factors $F(x)$ were obtained also for nearly symmetric polymer mixtures.[10,24–26] Figure 6[27] shows a typical scaled structure factor reported for a critical mixture of deuterated polybutadiene (DPB) and protonated polyisoprene (HPI) at $\Delta T = 3.9$ K in the late stage SD process (shown by + markers), together with $F(x)$'s obtained for L/W (green line)[12] and the critical mixture of isobutyric acid and water (I/W) (red line[28] and yellow line[29,30]). Also shown is $F(x)$ obtained by 3d computer simulation (solid line)[31] based upon a generalized time-dependent Ginzburg Landau (TDGL) theory[9] that incorporates the hydrodynamic interactions elaborated by Kawasaki–Ohta.[32]

The polymer mixture DPB/HPI has a lower-critical-solution-temperature-type phase diagram as in the case of L/W. Small-angle neutron scattering (SANS) studies as a function of temperature in single-phase state allowed us to determine the following characteristics of the mixture:[33–35] (i) It has spinodal temperature $T_s = 309.1$ K, which is well above the glass transition temperature $T_g = -95$ °C for DPB and -72 °C for HPI; (ii) the mean-field Flory interaction parameter per monomer unit χ_{eff} was evaluated as a function of T; and (iii) this result gives the parameter ε_T characterizing the thermodynamic driving force for the phase separation at the experimental temperature of $T = 313$ K,

$$\varepsilon_T \equiv (\chi_{eff} - \chi_s)/\chi_s = 0.0668. \tag{8a}$$

The fact that $\varepsilon_T \ll 1$ indicates that the system is in a *weak seg-*

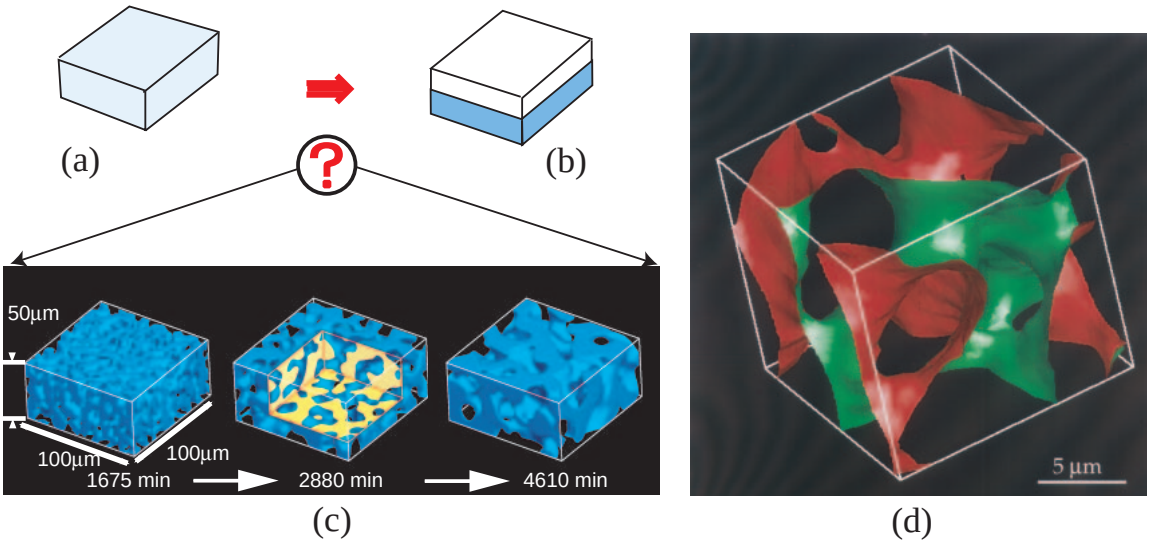

Fig. 7. Time-evolution of 3d real-space structures constructed by using LSCM for the critical mixture of DPB and PB-AN in the late stage SD (part c); Part (a) and (b) schematically show the initially homogeneous mixture before phase separation and the final equilibrium structure after phase separation, respectively (data based on Ref. 37). Part (d) shows a close-up image of 3d real space structure of the interface constructed with LSCM for the PB/SBR mixture developed in the late stage SD; Edge length of the bright cube corresponds to the characteristic (periodic) length Λ_m (from Ref. 40).

regation limit, as is true in the case of the critical mixture of simple liquids. This situation is also confirmed by a *large characteristic interfacial thickness* t_1,[25,26,36]

$$t_1 \cong 7R_g \tag{8b}$$

where R_g is the radius of gyration of DPB and of HPI, separately estimated to be approximately identical to 11.6 nm; (iv) thermal correlation length ξ_T was estimated to be 25 nm. This value is larger than R_g, reflecting again a weak segregation limit; and (v) $\varepsilon_T = 0.0668 \gg 1/N$ ($\cong 5 \times 10^{-4}$) so that the system is outside the critical region as specified by the Ginzburg criterion,[17] and hence the system is anticipated to follow the mean-field behavior. Such behavior is quite different from that of the critical mixtures in simple liquids, which will not follow the mean-field behavior.[17]

The fine agreement in $F(x)$'s obtained for various systems in Fig. 6 is impressive. However it is also important to note here a striking difference in the time scale and the quench depth ΔT of the systems: $F(x)$'s for the polymer system were obtained in the time scale of 300 to 6000 min, instead of order of 100 s for the simple-liquid mixtures, and at ΔT of order of 1 K, instead of order of the 1 mK for the simple-liquid mixtures. Both factors are larger in the polymer system than in the small-molecule system by a factor of about 1000! Despite the facts that the real length scale and real time scale for the self-organizing structures are very different in these two systems, we can conclude that the growing structures for the simple-liquid mixtures and the polymer mixture have the same form. We can further conclude that these structures can be theoretically predicted very well by the generalized TDGL equation.

Note that the structure factor for the polymer mixture is obtained over a much wider reduced q-range (up to about 10) than that for the simple liquid mixture (up to about 2). Thus we can explore further details of phase-separating structure, especially the hierarchical structures by using polymers as a model system.

3.3 Visualization of Universal Structure. What is the real-space structure corresponding to the universal scaled structure factor shown in Fig. 6? Generally, three dimensional (3d) phase-separating structures can be detected by laser scanning confocal microscopy (LSCM) for polymer mixtures, because the rate of phase separation in polymer mixtures can be much slower than the data acquisition rate of LSCM to construct the 3d volume objects. From this point of view, the quantitative detection seems to be almost impossible for simple-liquid mixtures at present. Figure 7 presents typical 3d structures constructed with LSCM (part c) during a phase separation process of a binary polymer mixture of DPB/PB-AN with equal phase volumes from a single-phase state (part a) to a macroscopically phase-separated state (part b).[37] Each 3d structure was obtained with the data acquisition time of ~6 min. The images were obtained at particular times in the late stage SD. PB-AN is polybutadiene (PB) labeled by a small amount of anthracene for a contrast enhancement under the fluorescence LSCM, and DPB is deuterated polybutadiene. This mixture has various advantages: (i) it fulfills satisfactorily dynamical symmetry because the dynamical-asymmetry parameter is very small ($\alpha_a = 0.16$), as will be detailed later in sec. 3.6; (ii) it has a weak LS contrast arising from a small refractive index difference due to an isotope effect so that the large phase-separated structure in the late stage SD would not cause significant multiple scattering effects; but (iii) it still has a clear contrast difference between the two phases under LSCM with the fluorescence mode.

The two phases shown in Fig. 7c consist of the PB-An rich phase indicated by blue color and the DPB-rich phase left empty. The two-phases are periodic and co-continuous, as highlighted by the cross sectional images displaced in the three orthogonal sections (in the middle image of part c). This kind of structure is called a **sponge-like structure** in the field of

differential geometry.[38] A quantitative comparison was made between the scaled structure factor obtained by time-resolved LS experiments and that obtained by the time-resolved LSCM experiments, the latter of which was obtained by 3d Fourier transform of the real-space images, as shown in Fig. 7c. A complete agreement of the two scaled structure factors over a wide q-scale and intensity scale assures that the 3d structure captured here represents the real structures developed in the mixture.[27,37,39] Moreover, this structure factor is found to be identical to the universal structure factor shown in Fig. 6. Therefore it must represent those evolved in the late stage SD for the critical mixtures of simple liquids as well, though the real-space 3d images of this kind have never been captured for small molecules, simply because the phase separation is too fast.

Figure 7d highlights an interface structure also obtained by using LSCM for PB/SBR (poly(styrene-*ran*-butadiene)) in the late stage SD.[40] The interface appears to be hyperbolic (saddle-shaped). The distribution of the interface curvature and its time evolution were analyzed from the 3d real-space structures, and these results were compared with those obtained by 3d computer simulations with the generalized TDGL equation.[41] The results are found to give a very good agreement, unveiling that the interface is saddle-shaped almost everywhere, having a negative Gaussian curvature K defined by

$$K \equiv k_1 k_2 \tag{9}$$

where k_i ($i = 1$ or 2) is a principal curvature of the interface. It is essential for the co-continuous structure to have the saddle-shaped interface, because both sides of space divided by the saddle interface can be continuous as opposed to the ellipsoidal interface for which the space inside the interface is isolated from that outside the interface.

3.4 Unveiled Hierarchical Structures. As elucidated in sec. 3.2, one can study scattering structure factors $F(x)$ for phase-separating structures over a much wider range of reduced scattering vector x by using polymer mixtures than by using simple-liquid mixtures (see Fig. 6). This suggests that polymer mixtures provide a good model system for exploring space-time organizations of hierarchical structures developed in the phase separation process. One can further enlarge the range of the scattering vector q over which the structures are investigated by using incident beams with different wavelengths (632.8 nm for He–Ne laser beam and 0.3–1 nm for neutron beam, for example). The slow dynamics of polymers enabled one to apply the combined time-resolved LS and SANS to explore the phase-separating structures over a wide length scale ranging from about 1 nm to 10 μm.[25,26,35] This corresponds to the possibility that the reduced scattering vector x can be covered from 0.1 to 10^3 (by considering the case of the q-range covered being from $(2\pi/10)$ μm^{-1} to $(2\pi/1)$ nm^{-1} and of the minimum attainable q_m being $(2\pi/1)$ μm^{-1}; cf. Fig. 6).

The investigation of the scattering structure factor for a given phase-separating system of the nearly symmetric dPB/HPI mixture with critical composition over the expanded q or x scale unveiled the hierarchical structure developed in the late stage SD, which is schematically summarized in Fig. 8.[35] We can observe the **global structure** as elaborated already in secs. 3.1 to 3.3 in the large length scale r of observation, $r > \Lambda_m$, or in the small wave number scale q of observation, $q \leq q_m$. Upon reducing r or increasing q such that $t_1 < r < R_m$ or $(2\pi/R_m) < q < (2\pi/t_1)$, we can zoom in on the global structure and observe the interface between the two phases;

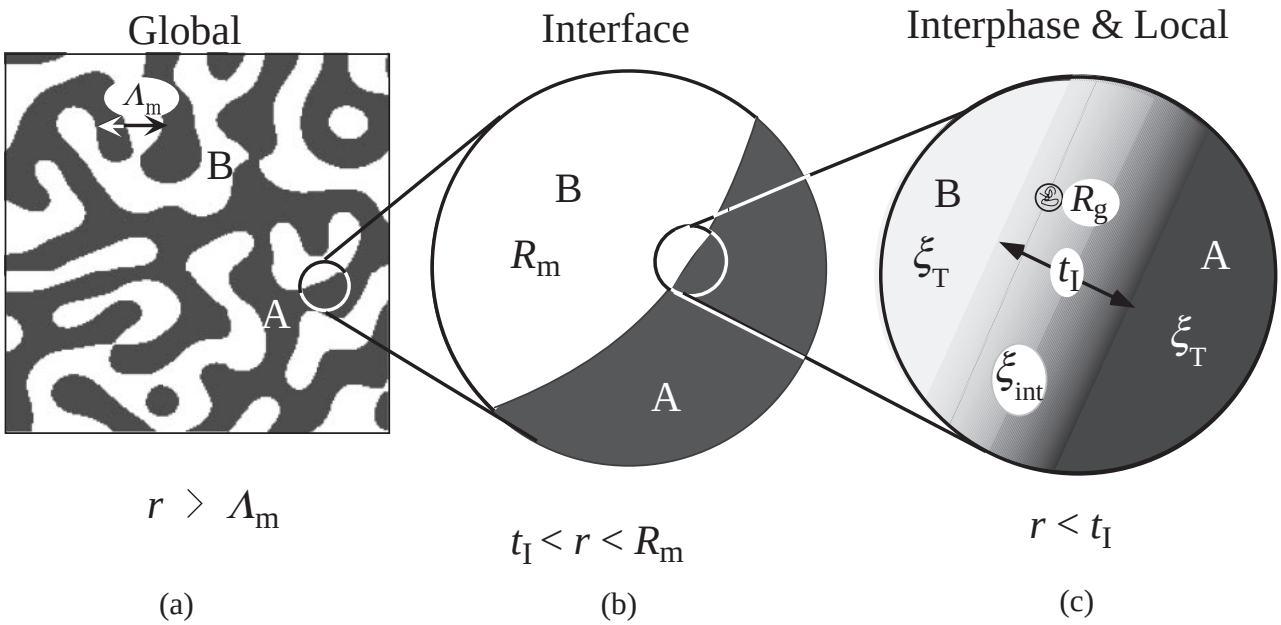

Fig. 8. Schematic representation of hierarchical structures developed by binary mixtures of A and B molecules (A/B) in a phase-separation process of the late stage SD. Note that the two components here have the dynamical symmetry and equal volume fraction. (a) to (c) refers to Global, Asymptotic (or Interface), and Interphase-and-Local scales, respectively, where r, Λ_m, R_m, t_1, ξ_{int}, ξ_T and R_g refer to length-scale of observation, characteristic length of the phase-separating domain structures, a mean radius of curvature, thickness of diffuse boundary (interphase), thermal correlation length within interphase, thermal correlation length within phase-separated domains, and radius of gyration, respectively. From Ref. 35.

rich in A polymer (for example, dPB) or B polymer (HPI). The characteristic parameter in this regime is **interface area per unit volume** $\Sigma(t)$ or **scattering mean radius of curvature** $R_m(t)$ defined by[42,43]

$$R_m^{-2} \equiv (3\langle H^2\rangle - \langle K\rangle)/2 \tag{10}$$

where H and K are respectively mean and Gassian curvature defined by

$$H \equiv (k_1 + k_2)/2, \tag{11}$$

and Eq. 9, respectively. The quantity $\langle I\rangle$ ($I = H^2$ or K) is defined by

$$\langle I\rangle \equiv \int I da / \int da \tag{12}$$

with $\int da$ being the integral over all interface area. The quantity t_1 is the characteristic interface thickness, as will be defined below. Upon further reducing r or increasing q such that $r < t_1$ and $q > 2\pi/t_1$, we can further zoom in the structure and observe an "**interphase**", an interfacial region of a finite thickness, where the composition of A changes from $\phi^e_{A,A}$ to $\phi^e_{A,B}$ across the interface, and "**local structure**". Here ϕ^e_{KJ} is equilibrium average local composition of K (K = A or B) in J-rich phase (J = A or B). The local structure is characterized by thermal composition fluctuations of A and B and their **thermal correlation length** ξ_T in A- and B-rich phases. The interphase structure can be characterized by the **interface thickness** t_1 and the **correlation length** ξ_{int} of the composition fluctuations **in the interphase**.

The self-organization of the structures was found to be characterized by at least five independent length scales which evolve with time: (i) $\Lambda_m(t) = 2\pi/q_m(t)$, the characteristic length scale for the global structure; (ii) $R_m(t)$, the scattering mean radius of the interface curvature or $\Sigma(t)^{-1}$, the volume occupied by unit interface area; (iii) $t_1(t)$, the characteristic interface thickness, (iv) the thermal correlation length ξ_T within each phase-separated domain; and (v) the thermal correlation length ξ_{int} characterizing thermal composition fluctuation in the interphase. The evaluation of all these quantities were discussed elsewhere.[16,25,26,35] It should be noted that ξ_{int} is relevant in the case when $t_1 > R_g$ as in the case of weak segregation limit but becomes irrelevant in a strong segregation limit of $t_1 \cong a < R_g$. It should be also noted that the concepts of dynamical scaling of the scattering structure factor with the single length parameter of $\Lambda_m(t)$ and of the universal scaled structure $F(x)$ are valid only for the global structure. $F(x)$ was found to be nonuniversal at $x > 2$, where the length parameters other than $\Lambda_m(t)$ come into play.[25,26] The nonuniversality is a manifestation of the hierarchical structures existing in the system.[35]

As for time-sequences of various events in the self-organization process, the following points have been elucidated.[25,35] (i) The local composition $\phi_{KJ}(t)$ first reaches equilibrium values $\phi_{KJ}{}^e$ in the beginning of the late stage SD at $t = t_{cr,1}$ (late stage I).[16] (ii) t_1 subsequently reaches the equilibrium value $t_1{}^e$ at $t \geq t_{cr,2}$, i.e., at a later time in the late stage SD (late stage II).[36] However the characteristic "local wave number" $\Sigma(t)$ and the characteristic "global wave number" $q_m(t)$ keep decreasing with t, which results in reducing the interfacial free energy of the system. These trends found are consistent with the general law anticipated for the ordering process described by the TDGL theory that Fourier modes with larger q's relax faster than those with smaller q's.

The author recommends his readers to go over references 10, 15, 25, and 35 for the various conclusions (conclusions 1 to 9) as well as for new pieces of evidence recently disclosed on the global structures such as the "**very early stage SD**", **scaling postulate**, "**N-branching**", etc.

3.5 Universality of Sponge-Like Structure. The sponge-like structure, unveiled for the critical mixtures of small molecules and symmetric polymers (Fig. 7), was found to be a universal structure for various nonequilibrium and equilibrium systems having characteristics of periodicity and continuity in 3d space. As for the case of nonequilibrium systems, in addition to the phase-separating structures discussed in sec. 3.3, we found the sponge-like structure as a transient microdomain structure of block copolymers developed in the ordering process of lamellae from disordered state[44] and as the one in chemical gels with fixed or static internal heterogeneities prepared by crosslinking reactions of monomers and crosslinkers in a solvent, e.g., crosslinked *N*-isopropylacrylamide gels (NIPAM) in water which are prepared at relatively high temperatures.[45] As for the case of equilibrium systems, we found the structure in a microemulsion composed of water, oil, and surfactant at hydrophile–lipophile balance,[46–48] in ternary mixtures of A-*b*-B diblock copolymer/A-homopolymer/B-homopolymer[49] and in mixtures of (a) (PS–PB)$_n$ starblock copolymer comprised of polystyrene (PS) blocks and PB blocks and poly(vinyl methyl ether).[50]

Figure 9 compares the sponge-like structure for a microemulsion (parts a and b) and for a phase-separating polymer mixture in the late stage SD (parts c and d). Both 3d real space structures shown in parts (a) and (c) were constructed[46–48] from measured small-angle X-ray scattering (SAXS) and LS intensity distributions, respectively, based upon Gaussian random field (GRF) theory.[6,51,52] Although the length scales of the two structures are very different (by a factor of about 300), the structures are almost identical. In the case of the polymer mixture one can construct 3d real space structure, without using the GRF theory, by using LSCM as described earlier and as demonstrated in part (d). The 3d structures (c) and (d) were quantitatively compared[48] in terms of distributions of local Gaussian and mean curvatures. Although there are some quantitative disparities between them, they are consistent on qualitative features in the curvature distributions, as is also evident from a visual comparison between (c) and (d). This conclusion obtained for the polymer mixture implicitly demonstrates the accuracy or reliability of the 3d structure constructed for the microemulsion based on GRF. In this sense also, we found that **polymer systems serve as good model systems** for small-molecule systems.

In order to really verify the accuracy of the structure in part (a), one has to first construct the real space structure to be displayed in part (b) by some means, e.g., by means of tomography in transmission electron microscopy on ultrathin sections of vitrified microemulsion specimens which are cryomicrotomed and then placed in a cryostage. The disparities between the two structures (c) and (d) reflect a small disparity between measured scattering profiles and scattering profiles predicted

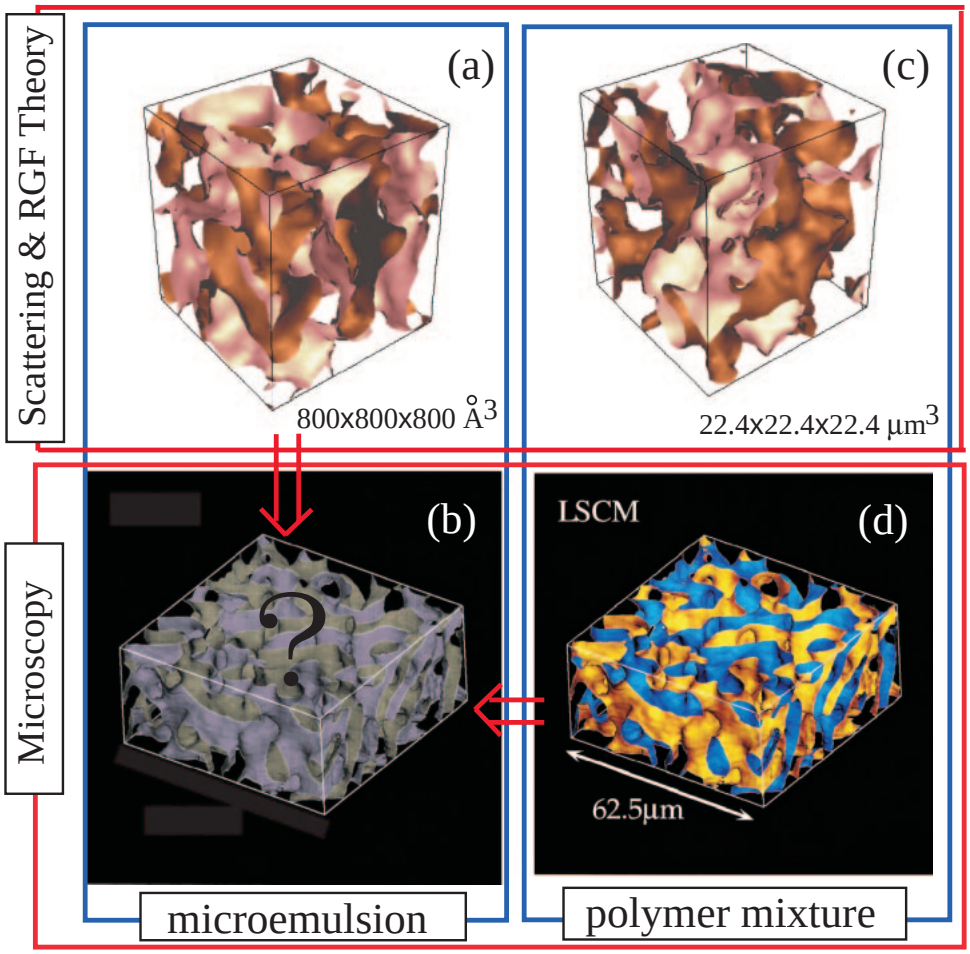

Fig. 9. 3d real space images of the interface structure for the microemulsion (oil/water/surfactant system) (a) and for the phase separating polymer mixtures (c), both constructed from respective scattering profiles in the context of the RGF theory, while part (d) shows the 3d real space image directly constructed with LSCM for the same polymer specimen as in part (c). The part (b) is the real space image expected and to be directly measured in future for the microemulsion. The characteristic length of the image (b) is ~1/300 of that of the image (d).

by the RGF theory at small q-region of $q < q_m$. In this sense, the TDGL theory predicts the phase-separating polymer system better than the GRF theory does.

3.6 Perspectives: Self-Assembly in Dynamically Asymmetric Systems. A. Uniqueness and Generality: Up to now we have focused on self-assembly of the hierarchical structures developed for mixtures comprised of either dynamically symmetric polymers or small molecules, as illustrated schematically in the left part or right part of Fig. 10a, respectively. In **dynamically symmetric mixtures**, component molecules A and B have equal self-diffusion coefficients (D_p for polymers and D_s for small-molecules). Many small-molecule systems belong to this family. Hence the nonequilibrium dynamics and processes for this family have been relatively well explored. Polymer pairs having about equal DP values and monomeric frictional coefficients (or D_s) also belong to this family.

In **dynamically asymmetric mixtures**, component molecules have different mobility values (self-diffusivity) as in the case of mixtures of polymers having different molecular weights, an extreme case of which is obtained for a high molecular weight polymer in a solvent as schematically shown in the left part of Fig. 10b, or a dispersion of colloidal particles in a solvent, as shown in the right part of Fig. 10b. Although the colloids themselves are not molecules, they are considered as one type of supramolecules. The dynamically asymmetric systems have been relatively less explored than their counterparts, despite of the fact that the systems should be more frequently found in nature and hence more general.

Structure formation involves growth of spatial composition fluctuations, which naturally involves local stress and stress relaxation. In the dynamically symmetric systems, this stress is equally divided into the two components, and the stress relaxes at equal rates in the course of structure growth. However, in the dynamically asymmetric systems, the component having larger mobility relaxes faster than its counterpart, so that the local stress is primarily borne by the smaller mobility component. This "imbalancely" borne local stress variation and relaxation affect free energy functional and cooperative diffusivity of the slower mobility component of the systems, which should be reflected back to the dynamics of the composition fluctuations and the form of growing patterns in the systems, as summarized in the bottom part of Fig. 10. This **stress-diffusion** coupling inherent in the asymmetric systems is anticipated to give intriguing effects on the dynamics and pattern for-

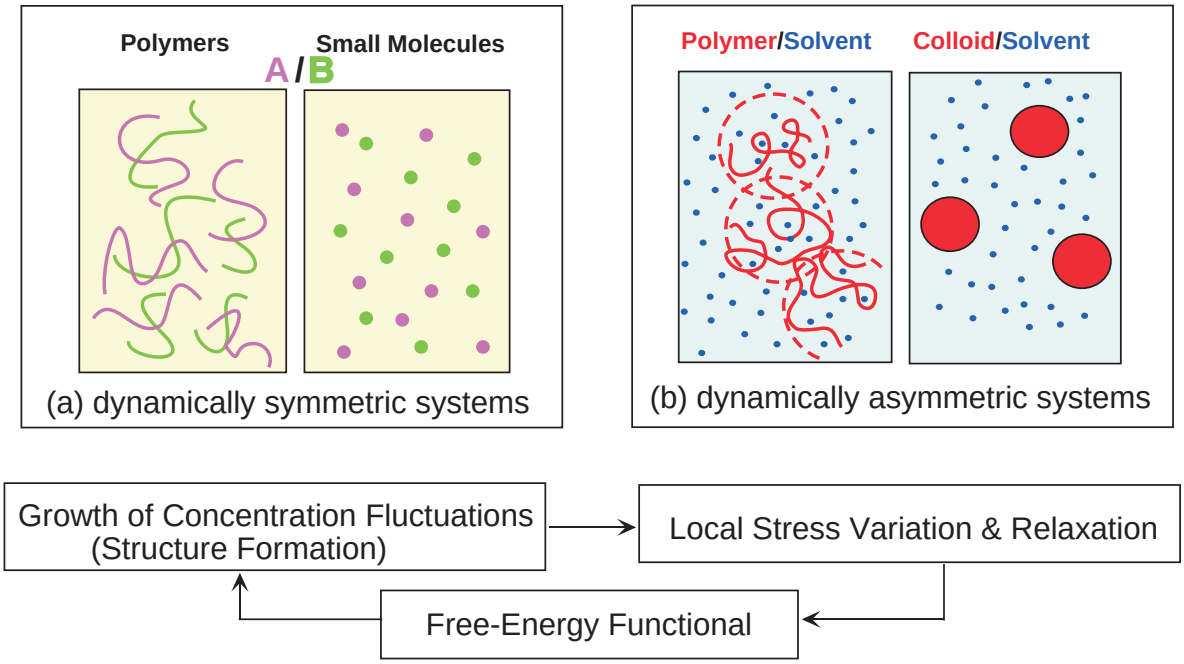

Fig. 10. Schematic representation of (a) dynamically symmetric binary mixtures of polymers A and B (left half) and small molecules A and B (right half) and of (b) dynamically asymmetric systems of polymer and solvent (left half) and colloidal particle and solvent (right half).

mation, theories of which have been pioneered by Onuki[53] for various systems. It is believed that various pattern formations in nature, including various materials and various systems of living bodies, may involve the stress-diffusion coupling. It is expected to be one of the most important future problems to unveil, both experimentally and theoretically, the unique pattern formation due to the effects. Below we shall present one example of the unique pattern formation.

B. Network Structure Formed by Minority and Slow Component: Figure 11 shows void formation of charged colloidal particles in water as observed by LSCM.[54] The system states were explored in the parameter space of salt concentration, charge density of the particles, and particle concentration. The void formation was discovered under a special condition of a very small or almost zero salt concentration, a high charge density (e.g., 4.8 $\mu C/cm^2$ per particle or the effective charge number of 1.4×10^3/particle), and a small particle concentration (e.g., 0.1 wt %). The density of the particles was carefully matched to water to avoid gravitational effects on the pattern formation. The particle diameter is 0.12 μm, and they appear as bright dots in the sliced images of depth resolution of 0.5 μm, because of scattering from the particles in liquid-like state. The series of patterns were obtained two months after homogenization of the dispersion via vigorous shaking of the cell. These sliced images were taken in the same area of the sample but by changing the slicing position along incident beam axis, i.e., the depth direction of the dispersion. Statistically identical patterns are observed everywhere in the sample cell, indicating that the pattern was not formed by gravitational effects but rather by long range electrostatic interactions. The patterns are comprised of regions rich in the particles, where the particles are in liquid state, and voids where no particles are observed. A careful tracing of a series of the sliced images reveals that the voids are not isolated but are interconnected along the depth and hence co-continuous with the network-type particle-rich regions. For example two voids A and B in slice (d) are separated, but they are interconnected in the focal planes located at 6 μm (slice (c)) and 13 μm (slice (b)) above slice (d).

It is quite striking to note that such a very dilute charged colloidal dispersion forms a **network structure** rich in particles in the matrix of the void phase under the field of long-range electrostatic interactions, regardless of the origin of the interactions, either DLVO-type repulsive interactions[55,56] or net attractive interactions.[54] If the repulsive interactions play a role, our intuition may predict a homogeneous liquid-like spatial distribution of the particles or clusters of the particles isolated in water (see Fig. 12c later). Even in the case when the net attractive interactions exist, formation of the isolated clusters as in Fig. 12c seems to be more reasonable than the network formation.

Figure 12 shows very schematically a model for the pattern formation. When the systems (part a) start to build up concentration fluctuations of the particles, the particles tend to form the network structures (part b) rather than clusters (part c), because they are interacting each other in the electrostatic field where the stresses built up by the fluctuations are borne only by the particles. In the stress relaxation process, solvent-rich regions may be created via a local solvent-squeezing process, i.e., a process involving squeezing of solvents from the regions rich in the particles, i.e., the regions where the local concentration of the particles is higher than the average concentration, into the regions poor in the particles, resulting in the network structure formation. The network structure coarsens with time. In the long time (hydrodynamic) limit, the network shown in part (b) will be eventually transformed into clusters shown

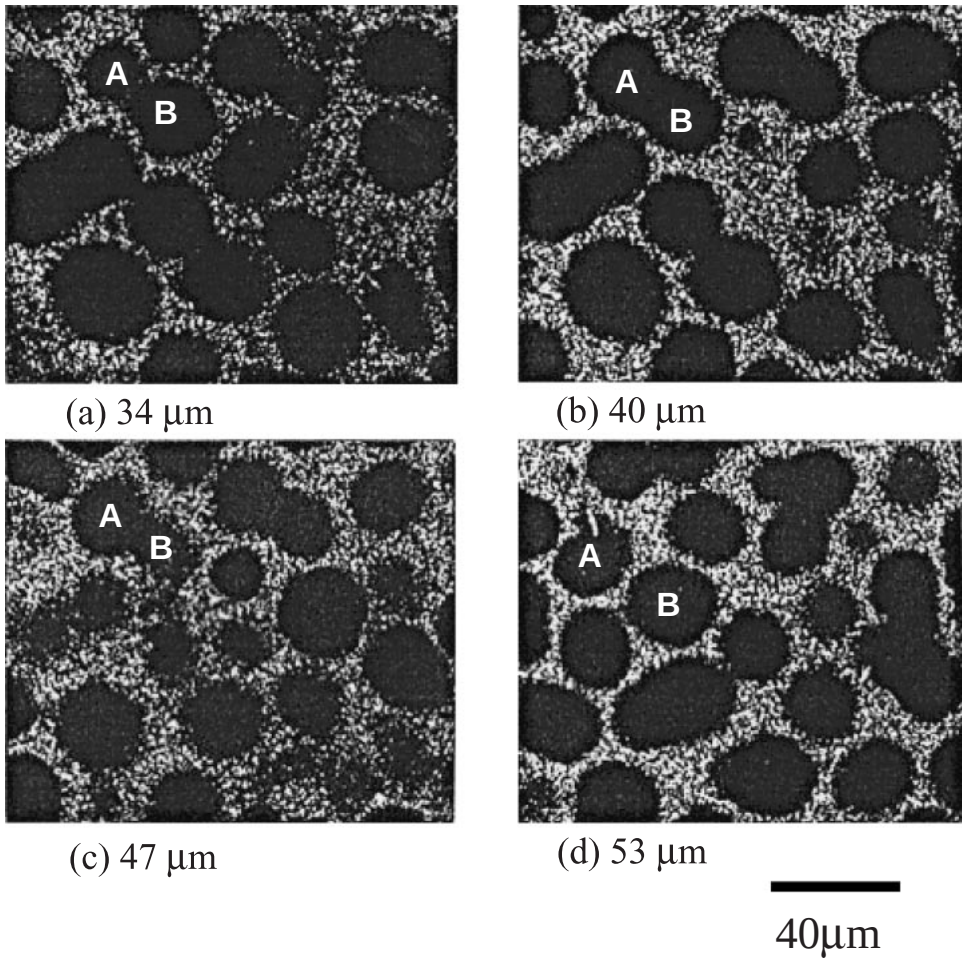

Fig. 11. Unique pattern formation in dilute suspension of charged colloidal particles in density-matched H_2O/D_2O medium as observed by a series of LSCM images on the same area of the sample but sliced at different depths along incident beam (the depth) direction (data based on Ref. 54).

in part (c). We may treat this phenomenon as phase separation coupled by the viscoelastic relaxation of the colloidal particles.

A similar network formation was reported in a phase-separation process of polymer solutions. For example, poly(vinyl methyl ether) in water, a highly dynamically asymmetric system, showed a network type structure rich in polymers in the matrix of water as a consequence of stress-diffusion coupling and visoelastic phase separation.[57] The network structures grow via the break-up processes of a part of the network or thread that bridges neighboring networks and the absorption or degeneration processes of the broken networks to the neighboring network. The break-up and absorption (degeneration) processes cause coarsening of the network structure so as to reduce total interface area and hence interfacial free energy of the threads. The break-up processes involve built-up local stress, and the absorption processes involve stress relaxation. In the growth process, the entangled polymer chains in the threads are pulled against each other by **rubber-like elastic force** and thinner parts of the thread will be broken. As a consequence, threads between the network junctions do not have either uniform diameters or smooth interfaces with water and the mesh size of the network has a broad distribution. Furthermore, growth of networks does not have self-similarity. These characteristics are believed to be a consequence of the threads being comprised of entangled polymer solution where the entangled polymer chains are in the field of **rubber-like elastic forces** in the course of this pattern formation. This elastic force field extends over a large length scale through the network structures of threads.

Note that the patterns reported here are already very large and macroscopic ($\geq$50 μm), reflecting a very late stage of phase separation. What happens in much earlier stages of the phase separation? What can we learn from a very early stage phase separation of such systems? How different is the behavior from that for a dynamically symmetric system? These fundamental issues have not yet been well explored and are not well understood. We have therefore been conducting a series of work along this line.[58,59]

C. Early-Stage Self-Assembly: Figure 13 represents time-resolved light scattering profiles in the course of phase separation via spinodal decomposition processes for (a) a semi-dilute solution of very high molecular weight PS in DOP, a typical system having the dynamical asymmetry,[58] and (b) a binary polymer mixture of PB and SBR, a dynamically symmetric system.[60] PS has a weight-average molecular weight ($\bar{M}_w$) of 5.48×10^6, and the PS concentration is 6 wt %, equal to 6.7

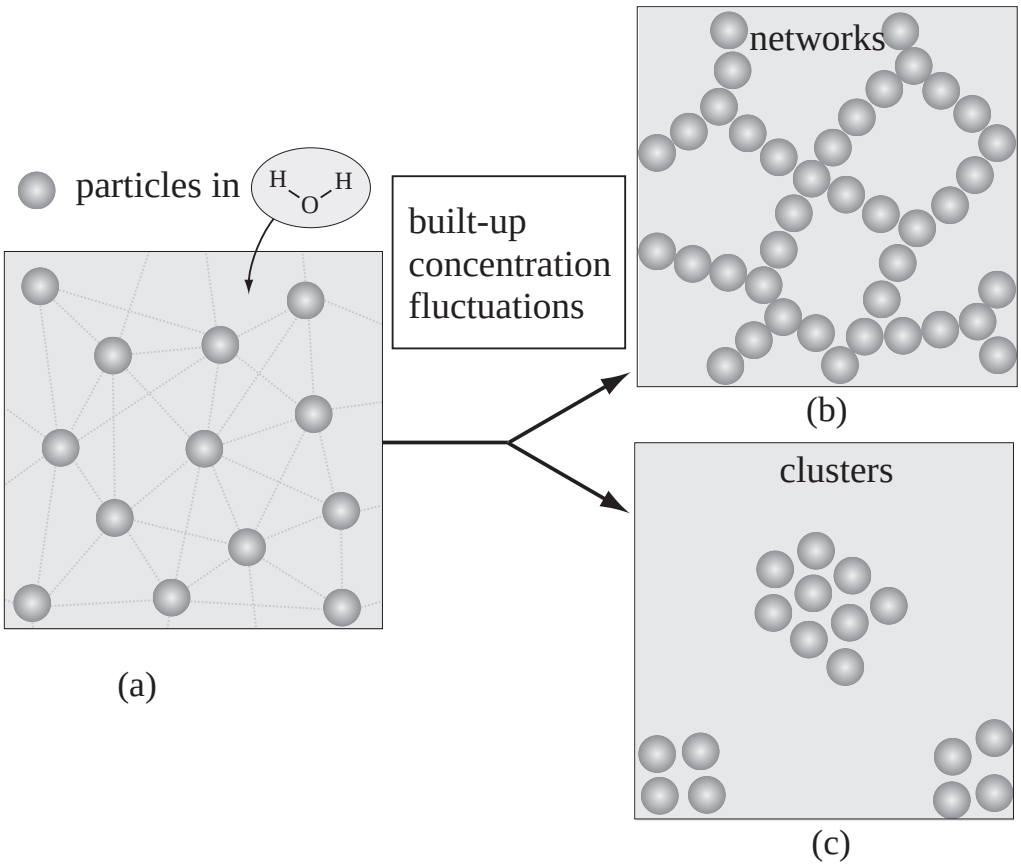

Fig. 12. Schematic illustrations of possible spatial distribution of charged colloidal particles in the density-matched H_2O/D_2O medium; (a) uniform distribution of the particles and (b) network type and (c) cluster-type inhomogeneous distribution of the particles.

times overlap concentration.[17] Figure 13a shows the result at quench depths of $\Delta T = 3.0\ ^\circ$C. In the early stage, shortly after the quench (see the top part of (a)), a very broad scattering maximum appears; the maximum intensity increases with time with the peak position almost unchanged, indicative of an early stage SD[6,10,15] where concentration fluctuations of a very large characteristic length of about 3 μm are developed for this system. As time elapses, the peak rapidly shifts toward small q and peak intensity further increases (see the bottom part of part a). It is quite striking to note that the low q modes increase their intensity but the high q modes do not. We note here that this time evolution behavior is very different from that observed for dynamically symmetric mixtures of simple liquids or polymers, as will be described below.

Figure 13b shows typical results for nearly dynamically symmetric polymer mixtures. In the early stage SD (top part), particular Fourier modes are selected to grow so that the scattering peak becomes sharper with time without changing q_m, in contrast to *the asymmetric system* where the peak tends to become broader with time. In the late stage (bottom part), the mode-coupling occurs so that high q-modes decay and low q-modes grow; consequently, the peak shifts toward low q. In contrast to this trend, for the asymmetric mixture only the low q modes grow and as a consequence the peak becomes broad and shifts toward small q. Apparently the profiles at different times in the bottom part of Fig. 13a cannot be scaled with the time-dependent q_m so that the domain-growth is not self-similar, albeit the time-evolution of the profiles in the bottom part of Fig. 13b clearly scales with the time-dependent q_m.[24] What do these unique characteristics mean? In order to understand the fundamental differences in the two systems, we theoretically analyzed the growth rate of various Fourier modes in the early stage SD as a function of q.

Suppose we have entangled polymer networks swollen by solvents and having a uniform concentration of polymers with average mesh size ξ_0, as shown in Fig. 14a where polymers are schematically illustrated by lines, and solvents are represented by small open circles and the gray medium.[58] Let us consider the case where concentration fluctuations with a characteristic length r are built up in the system by thermal excitation (see Fig. 14b), so that the system has regions slightly rich in polymers and regions slightly poor in polymers, represented respectively by the darker and brighter gray regions.

The concentration fluctuations will build up stress, and this stress is borne only by the polymers, since solvent molecules relax much faster than polymers. The built-up spatial variations of local stress will contribute to the free energy functional and hence to the cooperative diffusion of polymers, which in turn will affect the concentration fluctuations of polymers and hence the pattern formation of the system, suppressing the dynamics of the fluctuations. This intuition about the suppression will be proven to be correct later in Eq. 16. Let us consider the case where the concentration fluctuations of large-length scale as shown in Fig. 14c are thermally excited so that we have net-

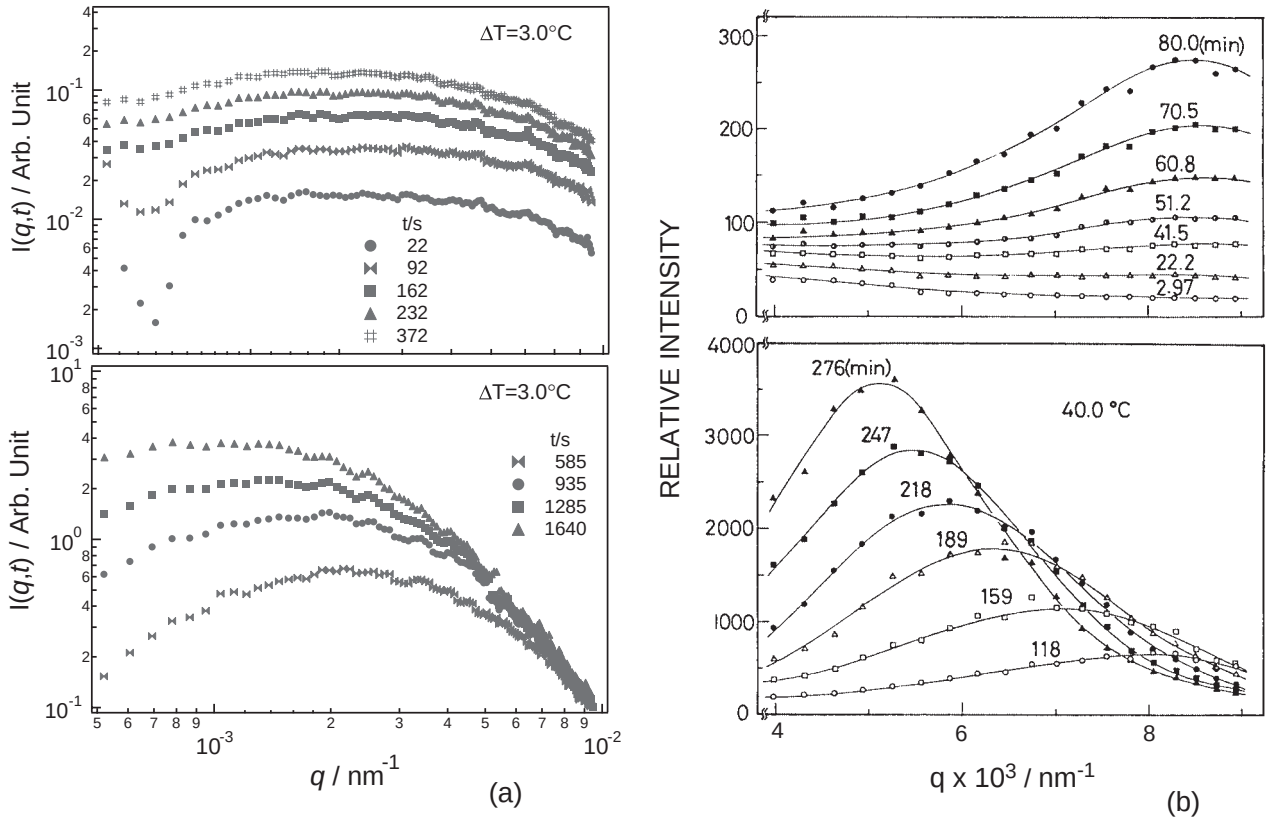

Fig. 13. Typical time-evolution of light scattering profiles for (a) the dynamically asymmetric system of PS548/DOP 6.0 wt % and (b) the dynamically symmetric mixture of SBR1/PB19 30 wt %/70 wt %. The top and bottom parts in (a) and (b) correspond to the early stage SD and the late stage SD, respectively. The data based on Refs. 58 and 60, respectively.

works with mesh size ξ smaller than ξ_0 in polymer-rich regions and networks with mesh size ξ large than ξ_0 in polymer-poor regions. Such fluctuations will be developed only after a very large length-scale molecular rearrangements and will inevitably occur very slowly. Under this situation, the stress developed will be completely relaxed at the time when such concentration fluctuations are built up via the long-range rearrangement of entangled polymers. Thus the stress-diffusion coupling is completely screened out in this case, leading to the concept of a "**screening length**" for the stress-diffusion coupling effects. This screening length was named **viscoelastic length**[53] ξ_{ve}: the stress-diffusion coupling is screened out if $r > \xi_{ve}$, but if $r < \xi_{ve}$ the coupling is effective. This length should depend on dynamical properties of component elements.

D. Theoretical Analysis of the Early-Stage Self-Assembly: Doi and Onuki[53,61,62] formulated a general time-evolution equation for composition fluctuations for dynamically asymmetric systems:

$$\frac{\partial}{\partial t}\delta\phi(\mathbf{r},t) = -\Lambda\nabla\cdot\left[\nabla\frac{\delta F}{\delta\phi} - \alpha_a\nabla\cdot\overleftrightarrow{\sigma}(\mathrm{r},t)\right] + \zeta(\mathrm{r},t) + (\text{Hydrodynamic Term}), \quad (13)$$

where $\delta\phi(\mathbf{r},t) \equiv \phi(\mathbf{r},t) - \phi_0$ represents fluctuations of local composition $\phi(\mathbf{r},t)$ of a component (e.g., A) in mixtures at position $\mathbf{r}$ and time t away from its average value ϕ_0. $F = F\{\delta\phi\}$ is the free energy functional of $\delta\phi(\mathbf{r},t)$, and $\delta F/\delta\phi$ is the variational derivative of F with respect to $\delta\phi(\mathbf{r},t)$. α_a is the so-called dynamical-asymmetry parameter defined by

$$\alpha_a = |D_A N_A - D_B N_B|/(D_A N_A \phi_B + D_B N_B \phi_A) \quad (14)$$

where D_K, N_K, and ϕ_K are self-diffusivity, DP, and volume fraction of K-th component in mixtures (K = A or B). In Eq. 14, $\alpha_a = {\phi_A}^{-1}$ for polymer solutions with ϕ_A being the volume fraction of polymer in the solution, $\overleftrightarrow{\sigma}(\mathbf{r},t)$ is the local stress tensor, and $\zeta(\mathbf{r},t)$ is the random thermal force expressed by the following fluctuation-dissipation theorem:

$$\langle\zeta(\mathbf{r},t)\zeta(\mathbf{r}',t')\rangle = 2k_B T\Lambda\nabla^2\delta(\mathbf{r}-\mathbf{r}')\delta(t-t') \quad (15)$$

where k_B and T are Boltzmann constant and absolute temperature, and $\langle x\rangle$ denoted the thermal average of quantity x. Cahn–Hilliard–Cook (CHC)[5–7] and Ginzburg–Landau (GL)[9] originally introduced the first and third terms on the right-hand side (rhs) of Eq. 13, while Kawasaki–Ohta introduced the hydrodynamic term.[32] Doi–Onuki further generalized the equation by incorporating the stress term associated with the dynamical asymmetry and the stress-diffusion coupling (the second term on the rhs of Eq. 13).[61]

If systems to be considered are dynamically symmetric, $D_A N_A = D_B N_B$, and hence $\alpha_a = 0$, the second term on the rhs of Eq. 13 vanishes. Consequently the equation reduces to the well-known **CHC equation or time-dependent GL (TDGL) equation**.[63] If $\delta\phi(\mathbf{r},t)$ is small and the hydrodynamic term can be neglected, Eq. 13 can be linearized, and the linearized equation in q-space is given by

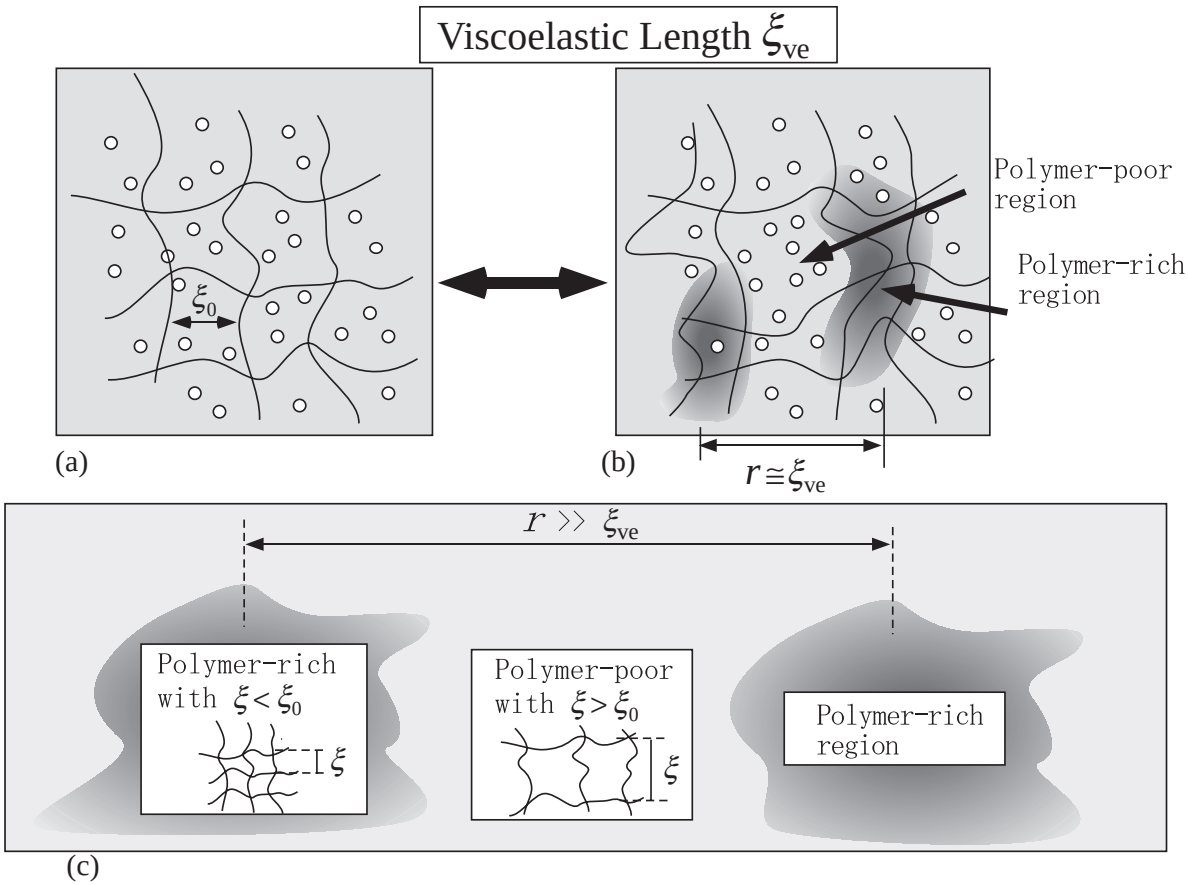

Fig. 14. Schematic representation of concept of stress-diffusion coupling and the viscoelastic effects in polymer solution. The lines and circles in parts (a) and (b) respectively designate polymer chains and solvents. Part (a) represents semi-dilute solutions with relatively homogeneous concentration, while parts (b) and (c) represent those with concentration fluctuations at a short length scale and at a large length scale, respectively. ξ_0 designates an average mesh size of entangled polymer networks for statistically homogeneous semi-dilute solution. In parts (b) and (c), the shaded regions designate polymer-rich regions with the average mesh size $\xi < \xi_0$, while the unshaded region designate polymer-poor regions with $\xi > \xi_0$. Parts (b) and (c) differ in the characteristic length r for the concentration fluctuations. In part (c) solvents were not shown. Based on Ref. 58.

$$\frac{\partial}{\partial t}\delta\phi(q,t) = \Lambda(q)q^2\Bigg[(r_0 - Cq^2)\delta\phi(q,t) - \frac{4}{3}\alpha_a^2\int_0^t \mathrm{d}t' G(t-t')\frac{\partial}{\partial t'}\delta\phi(q,t')\Bigg] + \zeta(q,t). \quad (16)$$

Here the first term on the rhs of Eq. 16 was obtained on the basis of GL expansion of the free energy functional. In Eq. 16 we assumed that the systems to be considered are isotropic so that **q** is replaced by q. $r_0 \equiv -(\partial^2 f/\partial\phi^2)_0$ (with f being the free energy density of the mixture) is a parameter related to thermodynamic driving force for composition fluctuations. The driving force is positive in a phase-separation condition, which therefore tends to grow fluctuations, while it is negative for mixtures in a single-phase state, which hence tends to decay thermally activated fluctuations. C is a positive constant related to the gradient free energy due to the nonlocality of interactions.[5,17] $G(t)$ is a relaxation function for shear modulus given by

$$G(t) = \sum_{i=1}^{n} G_i \exp(-t/\tau_i). \quad (17)$$

Here G_i and τ_i are the strength and relaxation time for the i-th relaxation process.

$$\langle\zeta(q,t)\zeta(q',t')\rangle = 2k_B T\Lambda(q)q^2\delta(t-t')(2\pi)^3\delta(q+q'). \quad (18)$$

The second term on the rhs of Eq. 16 represents the stress built up by the increase of composition fluctuations, $\partial\delta\phi(q,t')/\partial t'$. Since the integral is always positive, the stress term tends to suppress the growth rate of composition fluctuations or the relaxation rate of the fluctuations in single-phase mixtures, as we naturally anticipate. Thus interestingly enough, the dynamics is affected by the stress-relaxation process and hence by the mechanical properties of the system. In the case when the stress relaxes faster than the composition fluctuations, which is usually the case near the spinodal line, this integral is simplified such that the term $\partial\delta\phi(q,t')/\partial t' \cong \partial\delta\phi(q,t)/\partial t$ is put out side the integral. Under this situation we obtain,

$$\frac{\partial}{\partial t}\delta\phi(q,t) = \frac{\Lambda(q)}{1+\xi_{ve}{}^2 q^2}q^2(r_0 - Cq^2)\delta\phi(q,t) + \zeta(q,t) \quad (19)$$

where ξ_{ve} is the **viscoelastic length** defined by

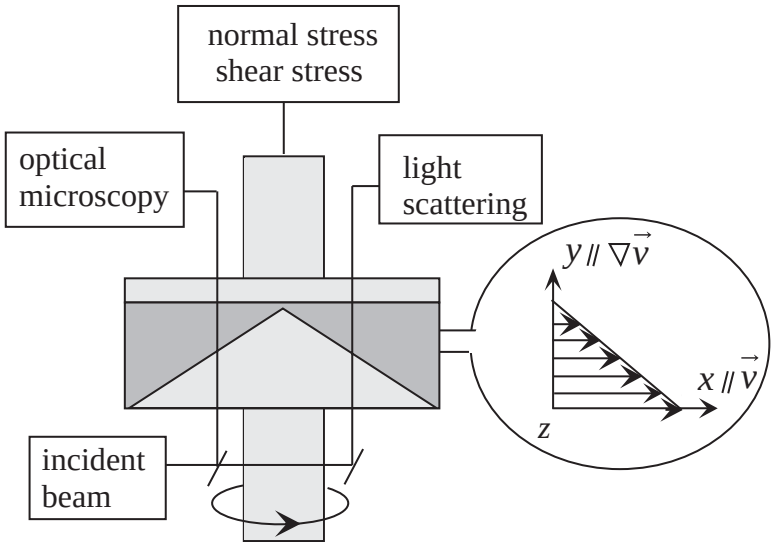

Fig. 15. Schematic representation of a rheo-optical apparatus for simultaneous measurements of shear and normal stresses, transmission optical microscopy, and light scattering, and definition of Cartesian coordinate axes of x, y, and z.

$$\xi_{ve} \equiv \left[\frac{4}{3}\alpha_a \Lambda(0)\eta_0\right]^{1/2} \tag{20}$$

and η_0 is zero-shear viscosity given by

$$\eta_0 \equiv \sum_{i=1}^{n} G_i \tau_i. \tag{21}$$

$\Lambda(0)$ in Eq. 20 is expressed by

$$\Lambda(0) = \phi_A \phi_B (D_A N_A \phi_B + D_B N_B \phi_A) \nu_0 / k_B T \tag{22}$$

where ν_0 is defined by

$$\nu_0 \equiv (\phi_A/\nu_A + \phi_B/\nu_B)^{-1} \tag{23}$$

with ν_K (K = A or B) being the molar volume of K-th monomeric unit.

The viscoelastic effect gives a renormalization effect on the Onsager kinetic coefficient $\Lambda(q)$ via the term of $(1 + \xi_{ve}^2 q^2)^{-1}$, giving rise to an effective suppression of $\Lambda(q)$. This suppression depends on a product of the viscoelastic length ξ_{ve} and q; the larger the value is, the larger is the suppression. This explains the **anomalous time-evolution behavior** as already discussed in Fig. 13a in comparison with the normal behavior in Fig. 13b. ξ_{ve} for the system in Fig. 13a was found to be very large,[58] $\xi_{ve}/R_g = 15.6$. ξ_{ve} is a unique and important characteristic length of the system which depends on the dynamical properties, most importantly on the dynamical-asymmetry parameter α_a, but it also depends on the zero shear viscosity and the small q-limit of the Onsager coefficient, $\Lambda(0)$.

It is important to note that the effects of dynamical asymmetry disappears in the case when $q \ll 1/\xi_{ve}$, or $r \gg \xi_{ve}$ or $t \gg \tau_{ve} \equiv \xi_{ve}^2/D$ (τ_{ve} and D being the relaxation time for the viscoelastic effects, **viscoelastic time**, and cooperative diffusion coefficient). In other words, the dynamically asymmetric effects are insignificant in the hydrodynamic regime of a large space-time scale of observation.

4. Self-Assembly of Molecular Mixtures under Shear Flow: Dissipative Structures Formed in Open Nonequilibrium Systems

4.1 General Background. We explored both dynamically symmetric mixtures and asymmetric mixtures under shear flow by **shear rheo-optical apparatuses** as detailed elsewhere[64–68] in order to elucidate, *in-situ* and at *real time*, dissipative structures developed in the systems and **shear-flow-induced phase transitions**. Figure 15 schematically presents a principle of the apparatuses for shear light scattering and optical microscopy.[68] We observe systems under simple shear flow in the shear cell made out of transparent cone-and-plate (or parallel-plate) fixtures simultaneously by light scattering and transmission light microscopy as well as by shear and normal stress as a function of shear rate $\dot{\gamma}$ and time after imposing $\dot{\gamma}$. In order to expand the q-range of our observation, we apply simultaneous observations of SANS[69–71] and/or SAXS.[66,67] In this case, the incident laser beam is replaced by a neutron beam or an X-ray beam. We set the Cartesian coordinate in such a way that x is parallel to flow direction, y to velocity gradient direction and z to neutral (or vorticity) direction, as also shown in Fig. 15. In most of the cases, the incident beam is parallel to the x axis and the scattering is observed on xz plane.

A series of our systematic studies of shear-flow effects on various systems revealed that shear flow changes the equilibrium state of systems: In one case, shear flow brings two-phase systems into single-phase (**shear-induced single-phase formation**) but in other cases shear flow brings single-phase into two-phase (**shear-induced phase separation**); Interestingly enough, these two effects are quite opposite. We propose, from a series of our studies, that the shear-induced single-phase formation occurs in dynamically symmetric systems with sufficiently weak interfacial tension, while the shear-induced phase separation occurs in dynamically asymmetric systems. We shall discuss below each of the two cases.

There are two important basic parameters for the shear flow effects on system state: (i) the shear rate $\dot{\gamma}$ that we can exter-

nally vary and (ii) the characteristic relaxation rate Γ inherent in the systems. Γ is the relaxation rate for concentration (or composition) fluctuations ($\Gamma_{\text{conc.}}$), for dynamically symmetric systems, while Γ is the relaxation rate for the viscoelastic effect ($\Gamma_{\text{ve}} \sim \tau_{\text{ve}}^{-1}$) and/or the longest relaxation rate of polymer chains (Γ_ℓ) for dynamically asymmetric systems. If $\dot{\gamma} < \Gamma$, there will be no effects of shear, because the fluctuations decay before shear affects and deforms the fluctuations. However if $\dot{\gamma} > \Gamma$, the shear deforms the fluctuations and hence alters the system state. Unique points in polymers are anticipated to arise from Γ being very small compared with the values for small molecules. Hence even **very small shear rates affect polymer systems** compared to the case of small-molecule systems.

4.2 Dynamically Symmetric Systems. A. Shear Rate-Dependent Dissipative Structures: As an example of the symmetric system, we show the results obtained for a 50/50 mixture of PS/PB in a solvent of DOP. DOP is a neutral solvent equally partitioned between the two polymers and acts as a continuous matrix that weakens repulsive interactions of two polymers. Total polymer concentration is small so that polymers are weakly overlapped and entangled. We found various steady state dissipative structures as a function of shear rate as summarized in Fig. 16.[65,72–74,77–79]

In quiescent state, we found a macroscopic phase separation into two phases comprised of the solution rich in PB and the solution rich in PS (regime I in the left corner of Fig. 16). Upon applying shear, the interface is broken so that nearly isotropic domains are formed (regime II in part a). Domains become smaller and become deformed into ellipsoidal shapes, having a very narrow size distribution along the neutral axis with $\sigma_{\text{R}}/\bar{R} = 0.04$ where σ_{R} and $\bar{R}$ are the standard deviation and the average size (part b in regime III).[73,74] They are aligned along the flow direction and eventually percolate along the flow; the process is called **shear-induced cluster-to-percolation transition** (C-P trans.) as shown in part (c).[73,75,76] Although the overall structure is stationary, it shows irregularities with time such as frequent break-up, branching, interconnections, and exchanges among the percolated domains. The interface fluctuations are suppressed with increasing $\dot{\gamma}$. The system eventually formed a stable "**string**" oriented along the flow direction, as shown in part (d) in regime IV.[65,68,77] Upon further increase of $\dot{\gamma}$, the composition of each phase deviates from the equilibrium one in such a way that the composition difference between the two phases decreases, as shown in part (e) in regime IV,[72,78] and eventually diminishes to result in shear-induced single-phase state, as shown in part (f), regime V.[75,78,79]

It is very important to note that, even in the high shear rates in regime V, the polymers coils are essentially in a relaxed state so that the stress-diffusion coupling does not come into play. The mechanical energy imposed to the system gives only the following effects: It breaks up domains and hence increases the interface at low shear rates and suppresses composition fluctuations of PS and PB at high shear rates. All these effects occur even in very small shear rates that would not cause elastic deformation of polymer chains, simply because the two-phase system shown in the left corner of Fig. 16 has only a weak interfacial tension.[77] If we could further increase the shear rate in regime V, the polymer chains should deform and hence the elastic deformation effects on the system state would come into play, as will be discussed in sec. 4.3. However, before approaching this state, this system exhibited instability against the simple shear flow, so that this state has not been practically realized so far.

B. A Law on Shear-Induced Phase Transition: The shear-induced single phase formation at a given T below the critical temperature $T_{\text{c}}(0)$ of the system at $\dot{\gamma} = 0$ occurs at shear rate larger than critical shear rate $\dot{\gamma}_{\text{c}}$ (see Fig. 17a). This situation is considered to be equivalent to a critical temperature drop from $T_{\text{c}}(0)$ to T by an amount of $\Delta T_{\text{c}}(\dot{\gamma}) \equiv T_{\text{c}}(0) - T$ under a given shear rate of $\dot{\gamma} = \dot{\gamma}_{\text{c}}$ (see Fig. 17b). The $\Delta T_{\text{c}}(\dot{\gamma})$ found experimentally was of order of 1 mK for the small-molecule system[3] and 10 K for the polymer system over the shear-range experimentally covered.[75,79] A law on the shear-rate dependence of critical temperature drop $\Delta T_{\text{c}}(\dot{\gamma})$ was first found to be given by Eq. 24 below for a small molecule system by Beysens et al.[3] and to be given by Eq. 25 for the symmetric polymer system by Hashimoto et al.[75,79]

$$\frac{\Delta T_{\text{c}}(\dot{\gamma})}{T_{\text{c}}(0)} = (5.9 \pm 0.7) \times 10^{-7} \dot{\gamma}^{0.53 \pm 0.3}, \tag{24}$$

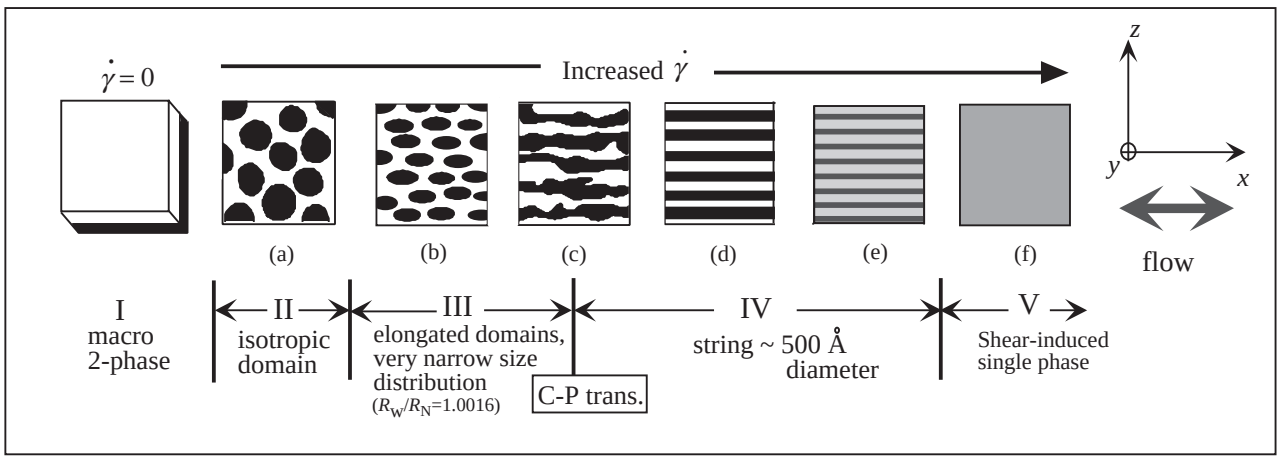

Fig. 16. Schematic illustrations of various shear-rate dependent steady-state dissipative structures found for the dynamically symmetric systems of PS/PB (50/50) 3.3 wt % in DOP at $\Delta T = 8$ K (based on Ref. 65).

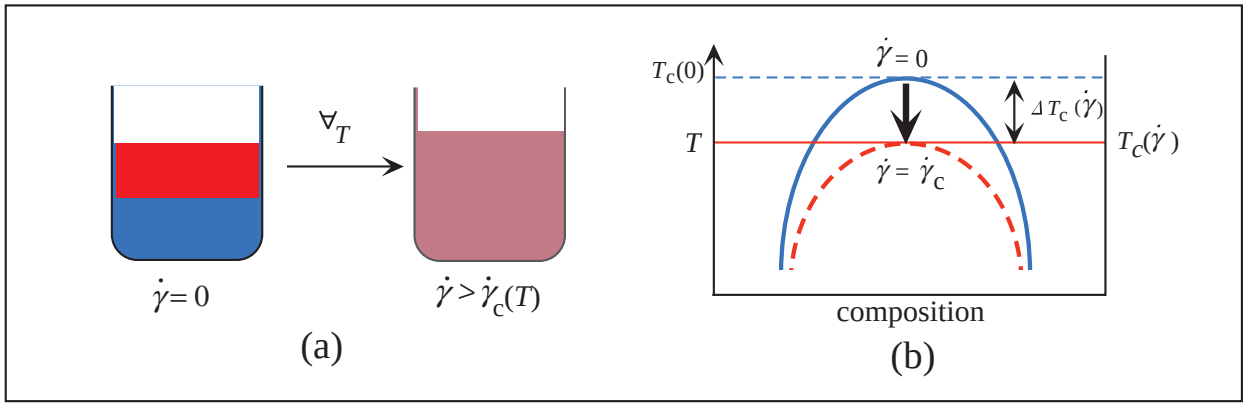

Fig. 17. (a) Shear-induced single-phase formation at shear rates greater than critical shear rate $\dot{\gamma}_c$ for a dynamically symmetric system (a) at a given T below critical temperature $T_c(0)$ in quiescent state and (b) temperature-induced single-phase formation at T under a given shear rate of $\dot{\gamma}=\dot{\gamma}_c$. The shear flow at $\dot{\gamma}$ apparently drop the critical temperature from $T_c(0)$ to T.

$$\frac{\Delta T_c(\dot{\gamma})}{T_c(0)} = (2.6 \pm 0.6) \times 10^{-3} \dot{\gamma}^{0.50\pm0.02}, \tag{25}$$

with $\dot{\gamma}$ in the units of s^{-1}. Rigorous assessment of the phase transition point under shear flow will be discussed later in sec. 4.2.E.

These laws are quite similar except for a very large difference in the prefactor of the shear-rate dependent term $\dot{\gamma}^n$ ($n = 0.53 \pm 0.3$ or 0.50 ± 0.02). The prefactor is the characteristic time τ_s to the power 0.53 for small-molecule system and the characteristic time τ_p to the power 0.5 for the polymer system. Since $\tau_p \gg \tau_s$ it is quite reasonable, though striking, that the prefactor of the polymer system is very much larger than that of the small-molecule system **by a factor of about 10^4**!

Based on the general principle introduced in sec. 4.1, we find that the law on $\Delta T_c(\dot{\gamma})$ can be qualitatively explained as follows. If $\dot{\gamma} < \Gamma_{conc}$, phase separation proceeds and domains grow over the time of order of $\dot{\gamma}^{-1}$. In the time scale longer than this, the shear deforms and destroy overgrown domains but destroyed small domains tend to grow, driven by thermodynamic driving force for the growth, giving rise to shear-rate dependent steady-state domain structure. However in the case when $\dot{\gamma} > \Gamma_{conc}$, there is no time available for concentration fluctuations to grow into the domains. Thus the system would be forced to stay in its single-phase state. The critical shear rate is the one at which shear rate is equal to Γ_{conc}. This concept together with physics of critical phenomena predicts

$$\dot{\gamma}_c \sim \Gamma_{conc} \sim \Delta T^n \quad \text{or} \quad \Delta T_c \sim \dot{\gamma}^{1/n}, \tag{26}$$

simply because $\Gamma_{conc} \sim \Delta T^n$. The first line of Eq. 26 predicts critical shear rate as a function of quench depth $\Delta T = T_c - T$, while the second line predicts the critical temperature drop $\Delta T_c(\dot{\gamma})$ as a function of shear rate. If the systems under consideration belong to 3d Ising universality class,[8] the value n is equal to 1.93. If the systems belong to mean-field universality class,[8] the value of n is equal to 2. These values of n together with Eq. 26 predict respectively Eq. 24 and 25.

C. Principle of Equivalence: Shear Plays Back Time-Evolution of Phase-Separated Structures in Quiescent State: The same principle discussed in the preceding section leads us to a prediction that shear flow will **"play back" the history** of time-evolution of the domain growth in the course of phase separation under quiescent state, simply by increasing $\dot{\gamma}$ from zero. This is simply because $\dot{\gamma}$ controls the time period $\dot{\gamma}^{-1}$ over which the domain grows under shear flow, as discussed in the preceding paragraph. This concept applies for the domain structure along the neutral axis (z-axis), as the shear deformation effects on the structure are expected to be minimum along this direction. Thus there exists a **principle of equivalence** between the domain structure at $\dot{\gamma}$ and that evolved at $t \cong \dot{\gamma}^{-1}$ in quiescent state.[78]

D. String Structure: The string structure in parts (d) and (e) in Fig. 16 is unique, for this structure has never been reported before. This string structure becomes unstable after cessation of the shear flow. Figure 18 presents time evolution of the structure after cessation of the shear flow. The time evolution was observed, simultaneously, *in situ* and *at real-time*, by the shear microscopy and light scattering method, as discussed earlier.[68,80] For this particular system, the stable string aligned parallel to flow can be observed at steady state directly under transmission light microscopy.[77] The strings give the sharp streak-like LS pattern oriented normal to flow direction, as seen in Fig. 18a.

After cessation of the shear flow, the string becomes unstable and is broken into a series of droplets aligned along the string, as shown in the left column of Figs. 18b and c. As a consequence it is transformed into a **pearl-necklace structure**, as seen under light microscopy. The droplet diameter is the same order as the string diameter. The droplets give rise to extra diffuse scattering superposed on the streak-like scattering arising from the oriented necklaces. A regular inter-droplet distance in the necklaces gives a scattering maximum along the original flow direction in the diffuse scattering from droplets. The "nematic" alignments of droplet centers parallel to the original flow direction give a "butterfly-type scattering" superposed on the sharp streak, as shown in the right column of Figs. 18b and c. The butterfly wings orient parallel to the original flow direction, while the streak orients normal to it. As time elapses, the nematic alignments of the droplets fade away because of the Brownian motions of the droplets, as evidenced by the decrease of streak-like scattering intensity. At the same time, droplets coalesce into large droplets to relax excess interfacial free energy, as evidenced by the increase of

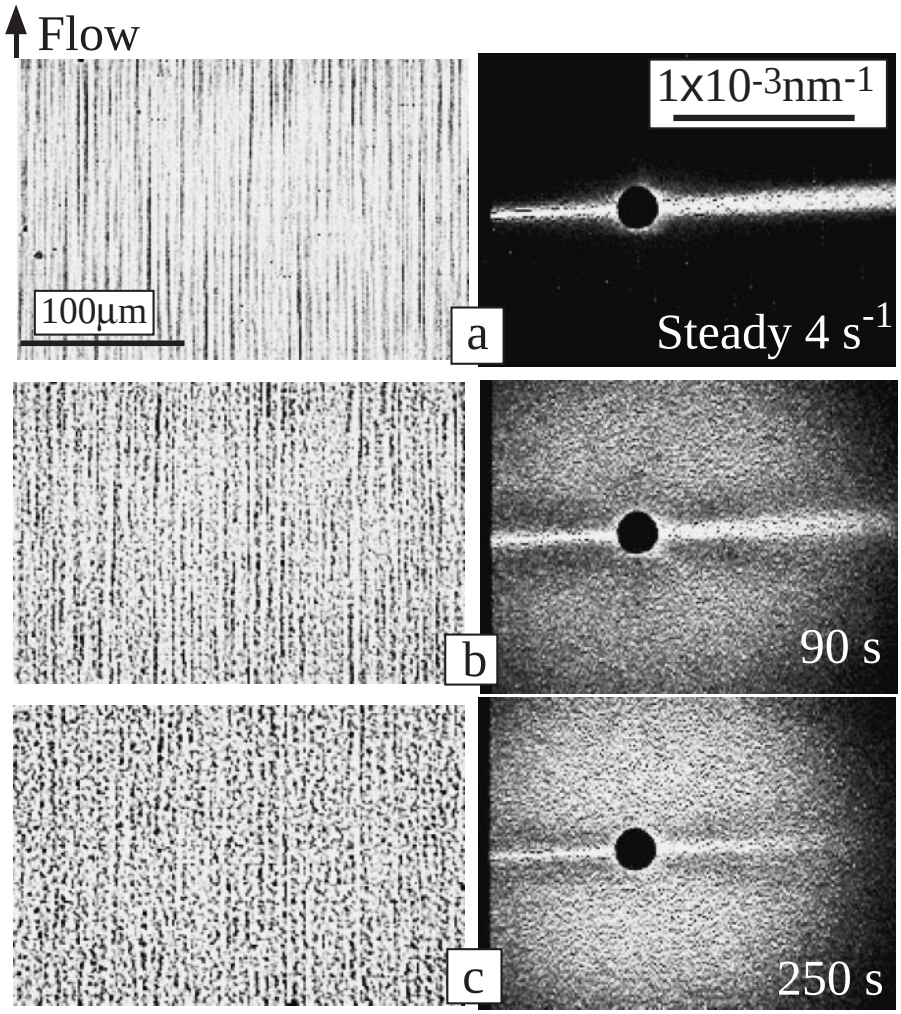

Fig. 18. Microscopic images (left half) and corresponding light scattering patterns (right half) for the PS/PB (80:20) DOP 3.3 wt % solution at $\Delta T = 10$ °C. The optical image and the scattering pattern in part (a) were obtained under steady state shear flow at $\dot{\gamma} = 4$ s^{-1}, while those from (b) and (c) were obtained at 90 s and 250 s after cessation of the steady shear flow at $\dot{\gamma} = 4$ s^{-1}, respectively.

the scattering intensity from the droplets and the decrease of the scattering vector at the maximum intensity along flow. The diffusion and coalescence of the droplets eventually leads to macroscopic phase separation, as shown in the left edge of Fig. 16.

The early stage of the instability of strings induced by shear cessation may be described as Tomotika's instability.[81] The linear analysis of Tomotika predicts a characteristic rate of growth in the amplitude of interface undulation Γ_{iu} of the string. We may anticipate that the stable string structure may be available at $\dot{\gamma} \geq \Gamma_{iu}$, where the shear flow suppresses the interface undulation, based on the principle as described earlier.

It is important to clarify why the string structure has not been reported in critical mixtures of small molecules so far. There are a number of possible reasons. (i) The interfacial tension σ_1 is not so small as that in the polymer system. The polymer system[77] has σ_1 of the order of 10^{-4} erg/cm^2. The small σ_1 value makes large domains stable and the large domains can be highly elongated parallel to a flow direction. If σ_1 is not sufficiently small, shear may make droplets smaller than a critical size, below which droplets become unstable, before droplets are highly elongated under shear flow. (ii) Thermal fluctuations, which are stronger in small molecules than in polymers, destabilize the string. (iii) Effective shear-rate and temperature ranges for the string structure to be developed for small-molecule systems may be very small compared with those for polymers. This may be coupled with reasons (i) and (ii).

E. Determination of Shear-Induced Phase Transition: The shear-induced phase transition was determined from both the two-phase state (in Regime IV)[75] and the single-phase state (in Regime V)[79] by analyzing a series of LS profiles $I(q_z)$ along the neutral axis (z-axis) measured as a function of shear rates at steady state. A qualitative observation of the disappearance (appearance, respectively) of the streak-like LS pattern with increasing (decreasing, respectively) $\dot{\gamma}$ in regime IV (V, respectively) is insufficient, because the appearance and disappearance may occur when the scattering objects just come in and out of the windows of our LS observation, respectively. One must indicate quantitatively a change in scattering functions between the two-phase state in Regime IV and the single phase state in Regime V in order to unequivocally assess

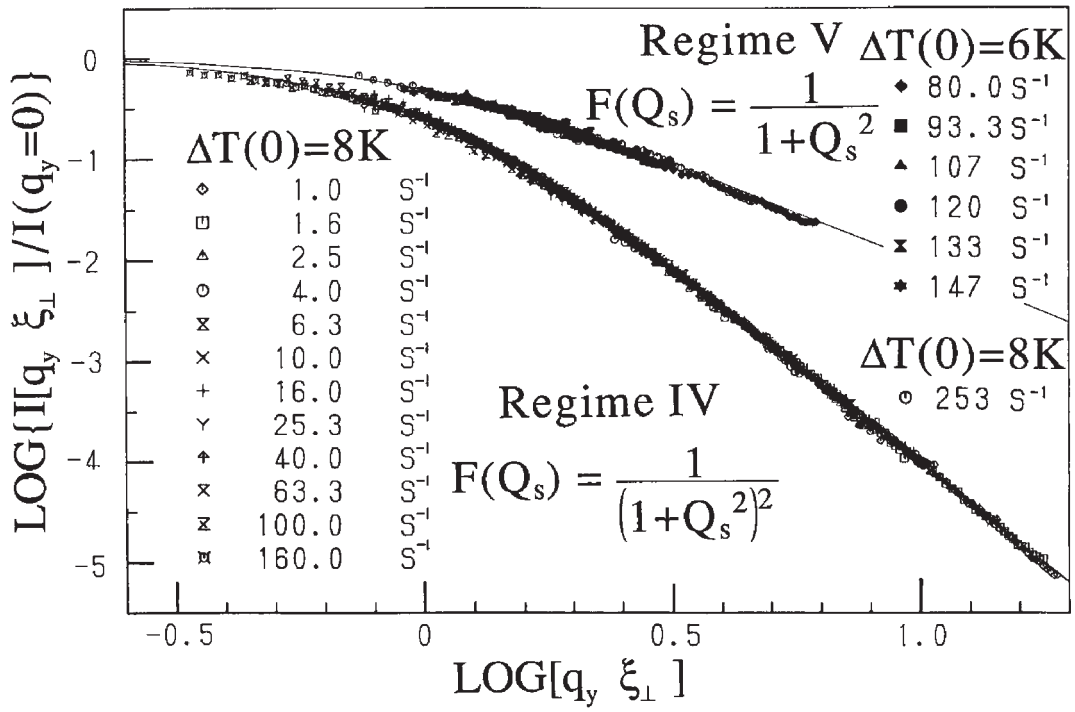

Fig. 19. Scaled structure factors for the PS/PB (50:50)/DOP 3.3 wt % solution under the shear flow in Regime IV at $\Delta T(0) = 8$ K and Regime V at $\Delta T(0) = 6$ and 8 K (from Ref. 78).

$\dot{\gamma}_{c,single}$.

In the two-phase state, the measured profiles $I(q_z)$ were characterized by squared Lorentzian functions (SQL):[72,78]

$$I(q_z) = I(q_z = 0)[1 + q_z^2(\xi_\perp)_d^2]^{-2} \tag{27}$$

where $(\xi_\perp)_d$ is the correlation length along q_z axis which depends on the lateral size of the strings; the greater the size, the larger the value of $(\xi_\perp)_d$. The squared Lorentzian function suggests that the system has a random two-phase structure having well-defined interfaces with the matrix along q_z over the q_z range covered in our experiments. Obviously $I(q_z = 0) \sim (\xi_\perp)_d^3$, and $(\xi_\perp)_d$ depends on $\dot{\gamma}$ and hence the plots $\log I(q_z)$ vs $\log q_z$ give a series of different curves when $\dot{\gamma}$ is varied. However when we reduce $I(q_z)$ and q_z by shear-rate dependent $I(q_z = 0)$ and $(\xi_\perp)_d$, respectively, we should obtain a shear rate-independent master curve of

$$F(Q_s) = [1 + Q_s^2]^{-2} \tag{28}$$

with

$$F(Q_s) \equiv I(q_z)/I(q_z = 0), \quad Q_s \equiv q_z\xi_\perp \tag{29}$$

where $\xi_\perp$ is $(\xi_\perp)_d$ for the two-phase state and $(\xi_\perp)_{fl}$ for the single-phase state (to be discussed later), respectively. Figure 19 shows the master curve of $\log F(Q_s)$ vs $\log Q_s$ obtained at a quench depth of $\Delta T(0) = 8$ K for a quiescent solution and at various shear rates from 1.0 to 160 s^{-1} (see the master curve labeled Regime IV).[72,78]

In the single-phase state, the measured profiles $I(q_z)$ were characterized by Lorentzian functions (**Ornstein-Zernike equation**[79,82])

$$I(q_z) = I(0)_{fl}[1 + q_z^2(\xi_\perp)_{fl}^2]^{-1} \tag{30}$$

where $I(0)_{fl}$ is the $I(q_z = 0)$ in the single phase state and $(\xi_\perp)_{fl}$ is the thermal correlation length along q_z (neutral axis) for the thermal concentration fluctuations under shear. $I(q_z = 0)$ and $(\xi_\perp)_{fl}$ depends on shear rate: $(\xi_\perp)_{fl}$ increases with decreasing $\dot{\gamma}$ toward the critical shear rate $\dot{\gamma}_{c,single}$ for the shear-induced phase transition. However when we scale $I(q_z)$ and q_z with $I(0)_{fl}$ and $(\xi_\perp)_{fl}^{-1}$, respectively, we should obtain a shear-rate independent master curves of

$$F(Q_s) = [1 + Q_s^2]^{-1}. \tag{31}$$

Figure 19 represents the master curve obtained at $\Delta T(0) = 6$ K and at shear rate from 80.0 to 147 s^{-1} and at $\Delta T(0) = 8$ K and at 253 s^{-1}.[72,78]

Thus we find that the shear-induced phase transition dramatically changes the nature of the scattering function along the neutral axis $I(q_z)$. This change in the scattering functions together with the shear-rate dependence of $(\xi_\perp)_d$, $(\xi_\perp)_{fl}$, $I(0)_d$, and $I(0)_{fl}$ enable us to determine unequivocally the shear-induced phase transition.[78] For the fixed q-range of observation with our shear rheo-optical apparatus, the observed profile $I(q_z)$ undergoes a unique shift over the master curve with increasing $\dot{\gamma}$ from regime IV to V as follows: The profile $I(q_z)$ starts from the tail part of the SQL master curve at large Q_s toward the head part of the SQL at small Q_s as $\xi_\perp$ decreases with increasing $\dot{\gamma}$ toward $\dot{\gamma}_{c,single}$. Upon further increase of $\dot{\gamma}$, the phase transition occurs and the profile discontinuously shifts to the tail part of the OZD mater curve at large Q_s. This is followed by shifting toward the head part of the OZD at small Q_s as $\xi_\perp$ again decreases with increasing $\dot{\gamma}$.

4.3 Dynamically Asymmetric Systems. As discussed earlier in sec. 3.6.D, the stress-diffusion coupling and the viscoelastic effects suppress the relaxation or growth rate of concentration fluctuations of dynamically asymmetric systems. This

kind of suppression is anticipated to cause the asymmetric systems to become increasingly susceptible to a weak shear with increasing asymmetry parameter α_a.

When a semidilute solution in a single-phase state is subjected to shear flow with a shear rate greater than a critical shear rate, the solution was found to change from a transparent solution to a turbid solution.[2] It was also reported that this shear-induced turbidity brings a change in the rheological behavior of the solution.[83–85] This intriguing phenomenon, as elucidated from transmitted light intensity and rheological properties as a function of shear rate $\dot{\gamma}$, suggests that the shear flow induces formation of dissipative structures in the solution, reflecting either shear-enhanced concentration fluctuations or shear-induced phase separation.

A. Observation of Shear-Induced Structure Formation: Those experimental studies described above were further advanced by a series of studies using some shear rheo-optical methods as described in sec. 4.1. The shear-LS[65,68,86–88] and shear-SANS[69,71,89] have been employed to elucidate scattering structure factors for systems under shear flow and deformation, while the shear optical microscopy (shear-OM) has been employed to elucidate real-space structures.[90] Figure 20 represents typical experimental results on shear-LS pattern (part a) and shear-OM images (part c to e) in the xz plane for a semidilute solution of a very high molecular weight PS ($\bar{M}_w = 5.48 \times 10^6$ and $\bar{M}_w/\bar{M}_n = 1.15$, $\bar{M}_n$ being the number-average molecular weight) with polymer concentration of 6.0 wt % in dioctyl phthalate (DOP) at 22 °C (θ solvent), a typical asymmetric system. The sample is designated PS548/DOP 6.0 wt %. This concentration is about 40 times higher than the overlap concentration c* and its cloud point is 13.8 °C. The experiments were done in the single-phase region at 27 °C.

The solution at rest (at $\dot{\gamma} = 0\ s^{-1}$) is in a single phase state so that it does not exhibit any appreciable LS even at small angles and no features in the OM image. When one imposes shear flow of $\dot{\gamma} = 0.23\ s^{-1}$, strong scattering appears along the flow direction (x axis) but scattering along the neutral direction (z axis) remains almost unchanged so that the scattering exhibits a so-called **butterfly pattern**, with the butterfly wings spreading along the x axis and with the dark string appearing along the z axis (part a). The OM images shown in (c) to (e) exhibit some anisotropic structures with a characteristic length of order of 10 μm which reflect dissipative structures developed by shear-induced phase separation or concen-

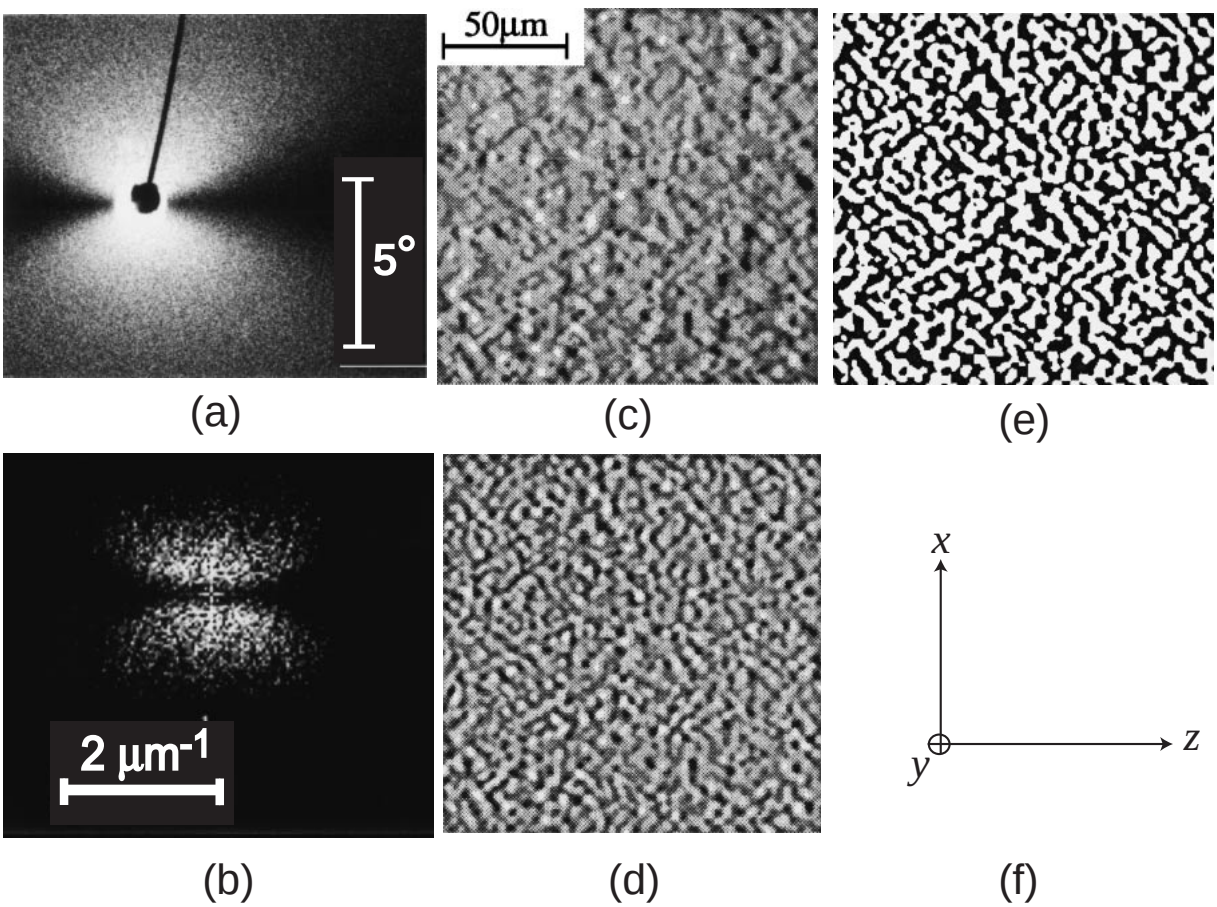

Fig. 20. Typical shear-LS at $\dot{\gamma} = 0.23\ s^{-1}$ (a). FFT pattern of (b) was obtained from shear-OM at $\dot{\gamma} = 0.23\ s^{-1}$ (c). The image (d) is obtained from the image (c) using a bandpass filter that is tuned to the dominant Fourier modes of the system corresponding to the LS pattern in (a). The image (e) is obtained after binarization of the image (d). The bars in part (a), (b), and (c) indicate, respectively, the scattering angle in the solution, the scattering vector in the solution, and the scale common to the OM images. The flow direction and neutral (vorticity) direction are vertical and horizontal, respectively, as shown in (f). The LS pattern (a) was taken with shutter speed of 1/250 s, while the OM images were taken with shutter speed of 10^{-4} s. From Ref. 90.

tration fluctuations at this shear rate. The fact that the structures observed under the OM images reflect true structures developed in the sheared solution can be confirmed by comparing the first Fourier transform (FFT) pattern (part b) of the images in part (c) with the scattering patterns in part a.[90] One can judge that the FFT pattern (b) exhibits the characteristics of the butterfly pattern (a), which assures that the OM image reflects a contrast variation of the transmission image arising from true concentration fluctuations developed in the system under shear flow. The butterfly patterns were observed at various temperatures[91] and concentrations[92] and for various solvents[91] such as cyclohexane and diethyl malonate which are θ solvents for PS at 35 °C, as well as dibutyl phthalate and tricresyl phosphate which are good solvents for PS. They were also observed for semidilute solutions of polyethylene in paraffin as a solvent (athermal solution).[93] They are thus quite general for sheared dynamically asymmetric systems.

B. Origin of Shear-Induced Structure Formation: Figure 21 represents schematically the origin of the butterfly-type scattering.[88] The concentration fluctuations of the single-phase system in quiescent state are small and isotropic as shown in part (a). Consequently the corresponding OM image is featureless, and the scattering is weak and circularly symmetric around the incident beam axis (y-axis) as shown in part (b). The shear flow at shear rates large than critical shear rate $\dot{\gamma}_{c,x}$ enhances plane wave concentration fluctuations along the flow direction (x-axis) but not much along the neutral direction (z-axis), as shown in part (c). These shear-enhanced concentration fluctuations give rise to strong scattered intensity along the x-axis but not much along the z-axis, giving rise to a butterfly-type anisotropic scattering pattern, as shown in part (d), and the contrast variation of the transmission OM image, as shown in part (c). Upon increasing $\dot{\gamma}$, the plane wave fluctuations grow in the directions away from the x-axis so that the butterfly wings are spread over a wider azimuthal angle μ and the OM image undergoes corresponding changes.[90] However the intensity along z-axis is kept unchanged from that for the quiescent solution up to a certain shear rate $\dot{\gamma}_{c,z}$, resulting in the dark streak or sector along the z-axis in the butterfly pattern. The shear rate $\dot{\gamma}_{c,z}$ is the critical shear rate above which the scattering intensity increases even along the z-axis, as will be detailed later.

Figure 22 schematically shows a "**solvent-squeeze model**" for the shear-enhanced concentration fluctuations. The single-phase solution in quiescent state is subjected to thermal concentration fluctuations and thus has regions rich in polymers having more entanglements as shown in gray regions of part (a) and regions poor in polymers having fewer entanglements as shown in bright regions of part (a). Under imposed shear flow, the regions rich in polymers are accompanied by larger stress than the other regions, giving rise to local stress variations. The stress can be relaxed via disentanglements, if $\dot{\gamma}$ is smaller than the disentanglement rate Γ_{dis}. In this case, the concentration fluctuations can be relaxed, and the solution remains homogeneous even under shear flow. However if $\dot{\gamma} > \Gamma_{dis}$, the stress developed in deformed entangled networks swollen by solvents can not have sufficient time to be relaxed by disentanglements. As a consequence, the stress or deforma-

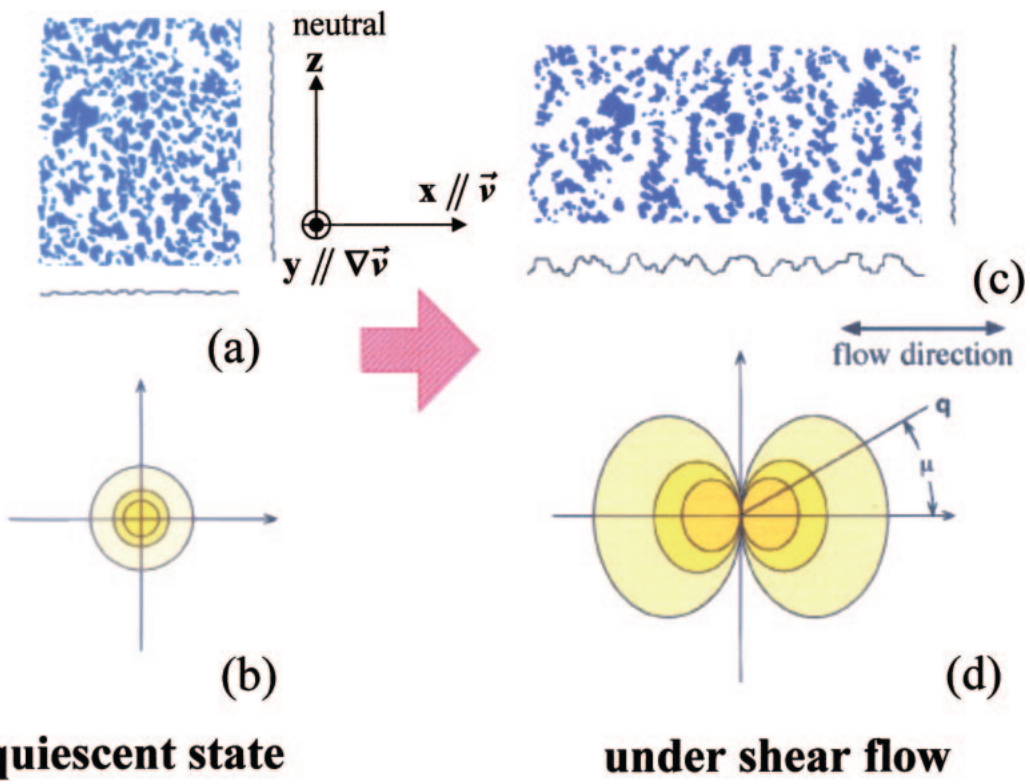

Fig. 21. Sketches of shear-enhanced concentration fluctuations (represented by a change from part a to c) and butterfly-type LS patterns (represented by a change from part b to d) (from Ref. 88). Spatial concentration fluctuations along x and z axes are schematically illustrated respectively beneath and right side of real space patterns (a) and (c).

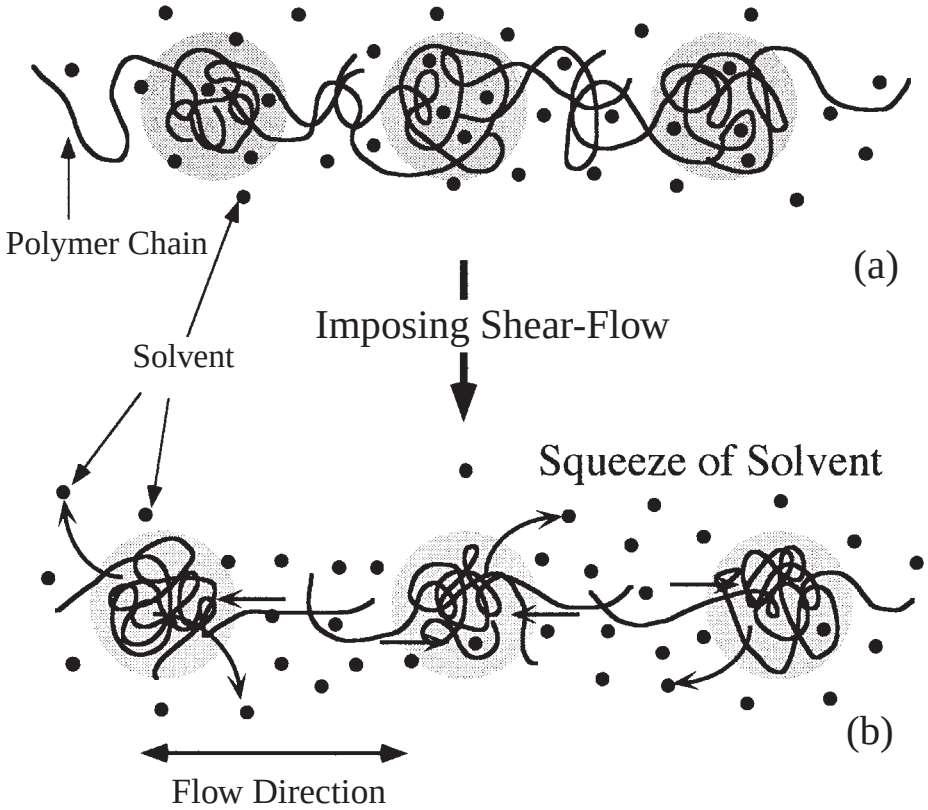

Fig. 22. Solvent-squeeze model for the shear-enhanced concentration fluctuations driven by the stress-diffusion coupling (from Ref. 70).

tion and orientation of the entangled polymers can be relaxed only by squeezing solvents from the regions rich in polymers, having higher elastic energy, into those poor in polymers against osmotic pressure as shown in part (b), resulting in regions rich in polymer becoming even richer and those poor in polymer becoming even poorer. Since deformation of swollen entangled chains are anisotropic, the shear-enhanced concentration fluctuations are also ainsotropic. The Fourier modes of the shear-enhanced fluctuations with wave vector **q** spread over a limited range in azimuthal angle μ in the xz plane, as shown in Figs. 21c and d.

C. Shear-Rate Dependent Steady-State Dissipative Structures: A series of rheo-optical studies[88,94,97] on the system as a function of shear rate revealed that the shear flow effects on the structure formation can be classified into four regimes, I to IV, in the order of increasing $\dot{\gamma}$ as summarized in row (A) of Fig. 23. The figure schematically illustrates scattering patterns in xz plane (row B), contrast-enhanced real-space images (row C), form dichroism and birefringence (rows D and E, respectively). The real scattering data as well as shear viscosity η and coefficient of the first normal stress difference ψ_1 data exist elsewhere.[88,94,97]

In Regime I, the concentration fluctuations or the scattering intensity are essentially identical to those in the quiescent solution, and η as well as ψ_1 are nearly independent of $\dot{\gamma}$. In this regime $\dot{\gamma}$ is smaller than the characteristic relaxation rate Γ (equal to Γ_{ve} or Γ_ℓ) so that shear flow would not affect the fluctuations, as discussed earlier in sec. 4.1. Thus, we observe no strong shear-enhanced scattering, featureless image for homogeneous solution, no form dichroism and no birefringence, as shown in column (a). Regimes II to IV exist at $\dot{\gamma} > \dot{\gamma}_{c,z}$, a critical shear rate above which shear-enhanced scattering is observed together with the decrease of η and ψ_1 with $\dot{\gamma}$. In this regime, $\dot{\gamma} > \Gamma$, so that shear flow affects the concentration fluctuations and hence the state of the solution. As discussed in sec. 3.6.C, the system under consideration is extremely dynamically asymmetric, so that the stress-diffusion coupling would strongly suppress Γ. As a consequence even the shear flow with small shear rates can enhance the concentration fluctuations via the solvent-squeeze mechanism, as elaborated in sec. 4.3.B.

In Regime II, the scattering dramatically increases along the flow direction such that an integrated scattered intensity along x axis, $I_\parallel$, increases by approximately 100-fold.[88,94,97] However, the integrated intensity normal to flow remains the same as that in the quiescent solution, giving rise to the dark streak that appears in the butterfly pattern. The enhanced concentration fluctuations generate dark and bright contrast variations in the transmission optical image as shown in column (b). The critical shear rate above which the enhanced scattering observed along the x-axis but not along the z-axis is specifically defined as $\dot{\gamma}_{c,x}$. ψ_1 and η starts to decrease with increasing $\dot{\gamma}$ above $\dot{\gamma}_{c,x}$. Yet form dichroism and birefringence are still very small. In Regime III, $I_\parallel$ keeps the high intensity level and does not vary much with $\dot{\gamma}$, while $I_\perp$ starts to increase and reaches a constant value with increasing $\dot{\gamma}$. This increase of the scattering intensity and hence of the concentration fluctuations along the neutral or vorticity direction is thought to be a non-linear effect brought about by the enhanced fluctuations along the flow, in the sense that the Fourier modes developed

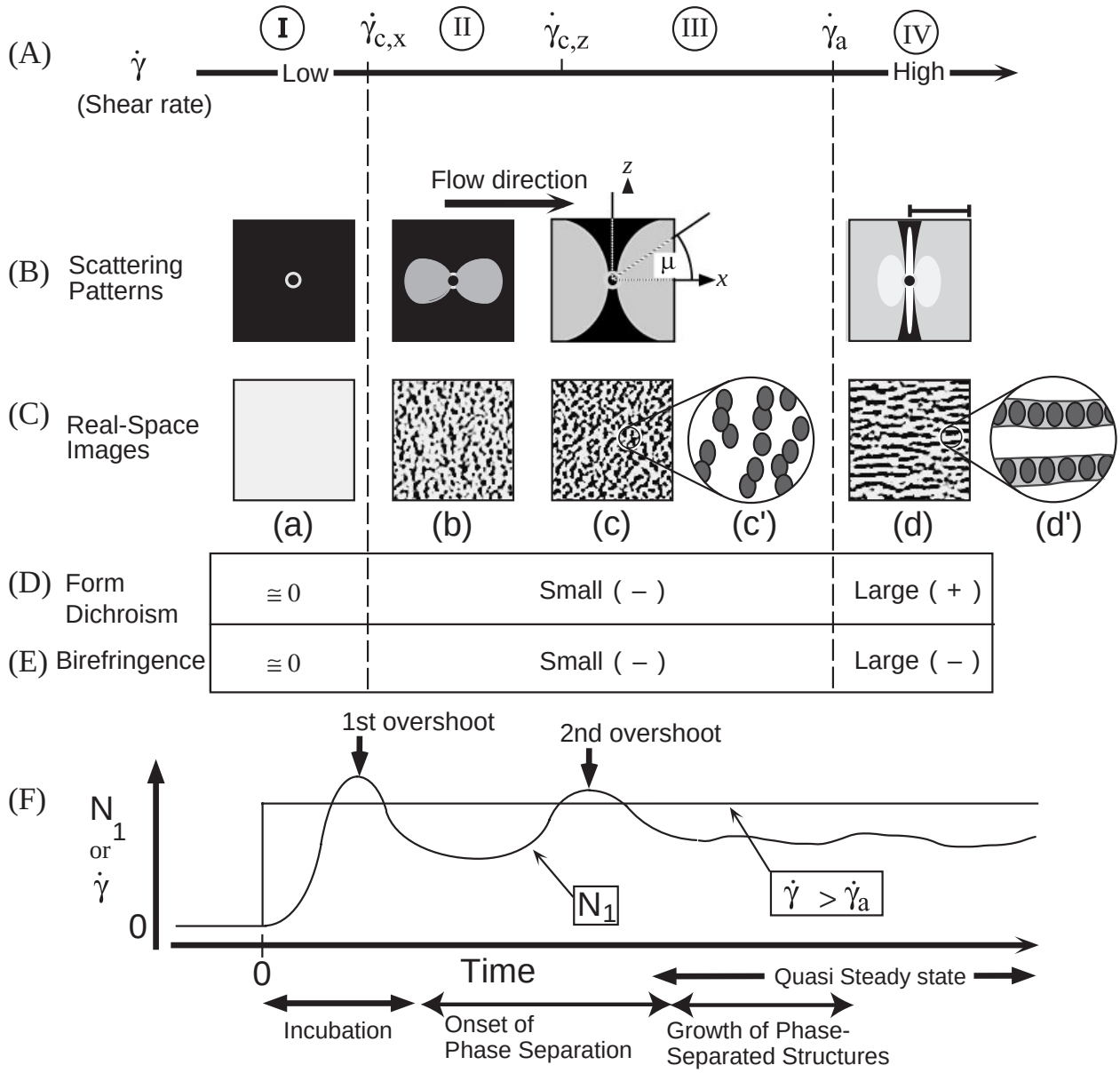

Fig. 23. Dissipative structures formed under steady-state shear flow and time-evolution of transient dissipative structures formed after imposing a step-up shear flow from zero shear rate to a given $\dot{\gamma}$ greater than $\dot{\gamma}_a$. A set of data shown in row (A) to (E) is meant to represent the steady state structures developed in each regime shown in column (a) to (d), while a set of data shown in row (B) to (F) is meant to represent the time evolution of the transient structures shown in column (a) to (d). The shear-rate range covered in the steady state experiments were found to be classified into four regimes of I to IV. The data based upon Refs. 94 and 97.

along the x axis excite those along the z axis. It may be reasonable to attribute the nonlinear effect and the onset of the increased value of $\mathit{l}_\perp(\dot{\gamma})$ to onset of the shear-induced phase separation.[69] In this regime, the butterfly wings spread over a larger μ value and the contrast of the optical image is further enhanced. The critical shear rate, above which this effect occurs, is specifically defined as $\dot{\gamma}_{cz}$. In this regime, ψ_1 and η decrease according to power laws. Consequently, dissipative structures developed under flow tend to decrease the mechanical energy dissipation in this nonequilibrium process. The scattering pattern in Fig. 20a and the OM images in Figs. 20c to 20e belong to this regime. Form dichroism and birefringence are still very small in this regime as well.

In Regime IV at $\dot{\gamma} > \dot{\gamma}_a$, an anomaly is observed in both the scattering and rheological behaviors. The scattering anomaly is seen in a further increase of both $\mathit{l}_\parallel$ and $\mathit{l}_\perp$ by a factor of $\sim$5 and $\sim$10, respectively. The increase of $\mathit{l}_\perp$ is a consequence of evolution of a sharp, strong streak-like scattering along z-axis, as shown in column (d). This anomaly is accompanied also by rheological anomalies. Upon increasing $\dot{\gamma}$ from a value in Regime III to that in Regime IV, the shear stress and normal stress momentarily increase dramatically. However if the solution is kept sheared, they eventually decay with time to reach steady values, though small variations still exist around the steady values. The steady values of η and ψ_1 in Regime IV are larger than those in Regime III and they tend to increases

with $\dot{\gamma}$. A strong streak-like LS pattern along the neutral direction is superposed on the butterfly pattern. The OM image shows string-like structures along the flow direction, as shown in column (d),[80] which is expected to correspond to the strong streak pattern. The scattering pattern and OM image are quite reminiscent of those shown in Fig. 18 obtained after cessation of the sheared symmetric systems which developed the string phase.[80] Thus the butterfly is expected to arise from the internal structures of the string, as schematically shown in part d′ in row (C). In other words, the phase-separated domains whose centers of mass aligned more or less randomly along z axis as shown in c and c′ in row (C) in Regime III tend to align parallel to flow direction with an interdomain distance of order of 1 μm to result in the formation of the string structure in Regime IV, as shown in parts (d) and (d′) in row (C). This string structure is again a rational optimum structure to minimize the mechanical energy dissipation under such strong shear flows.

As a consequence of the string-like structure, the dichroism shows a large positive value. The birefringence shows large negative values, indicative of end-to-end vectors of PS chains in the strings being oriented parallel to the string axis. The PS used are not a crystallizable polymer so that crystallization would not occur in Regime IV. However, if the polymers used are crystallizable as in the case of ultra-high molecular weight polyethylene (UHMWPE) in *n*-paraffin,[93,95] they would be crystallized into fibrillar crystalline superstructures composed of so-called "shishi-kebab" structures.[96] This is well known as shear-induced crystallization of polymer solutions. However, it would be extremely important to recognize a possibility that this shear-induced crystallization may be triggered and followed by the shear-enhanced concentration fluctuations and/or phase separation, especially in the case of polymer solutions.[95] The crystallization is anticipated to start to be triggered in the region rich in polymer concentrations. It may be conceivable that the string-like demixed structures act as a precursory structure for crystallization into the shishi-kebab structure.

D. Time-Evolution of Transient Dissipative Structures: In the preceding section we discussed various dissipative structures developed at steady-state shear flows with varying shear rates. Let us now focus on how the steady-state structures are developed after onset of the shear flow with shear rate larger than the critical shear rate, i.e., $\dot{\gamma} > \dot{\gamma}_{c,z}$ or $\dot{\gamma} > \dot{\gamma}_a$.

Figure 24 shows time-evolution of the first normal stress N_1, as transient rheological properties for the PS548/DOP 6.0 wt % solution at 27.5 °C after the onset of shear flow of a constant shear rate $\dot{\gamma} = 14.3\ s^{-1}$ in Regime III defined in sec. 4.3C.[97] The time-evolution of N_1 as well as σ (though not shown in the

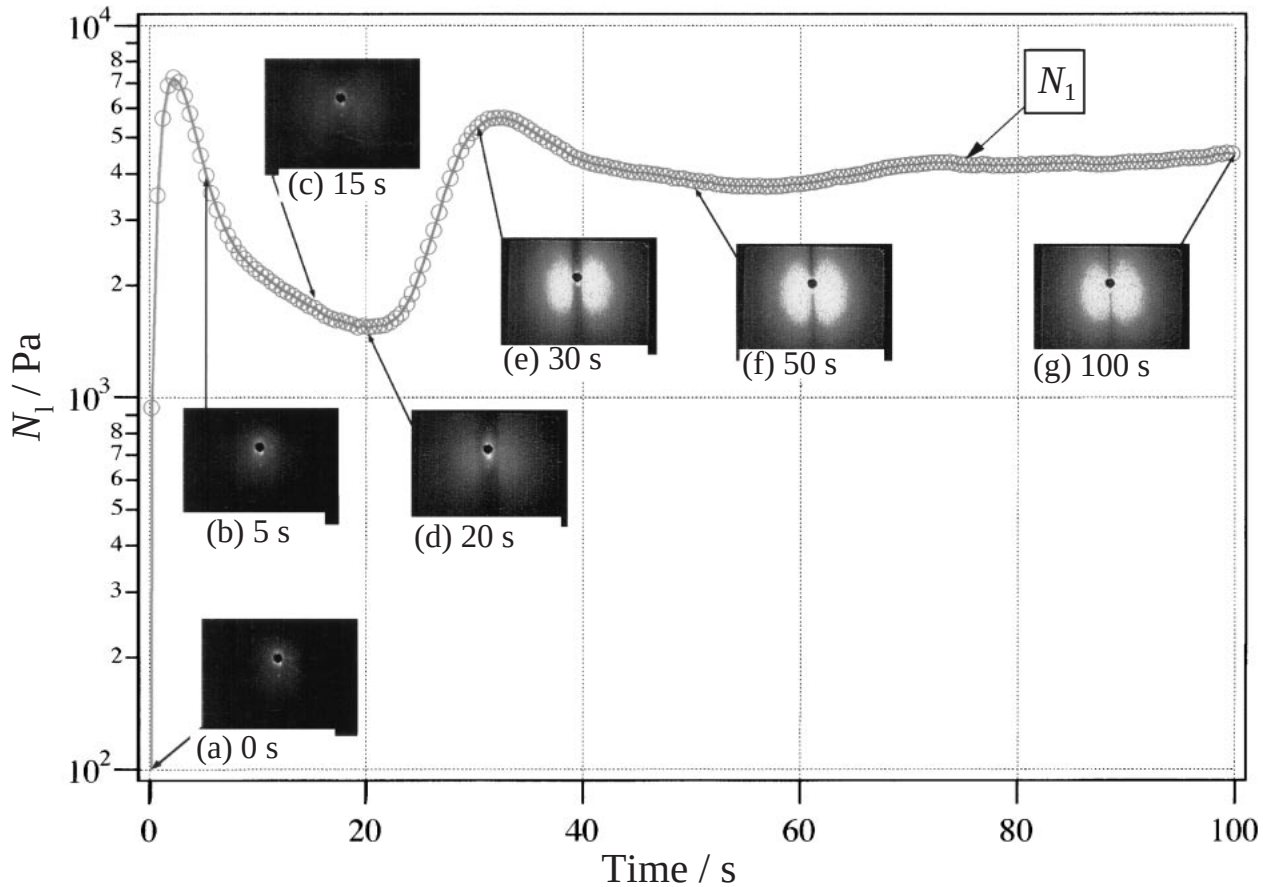

Fig. 24. Time evolution of the normal stress difference N_1 and the butterfly-type LS patterns in the inset to the figure (flow direction being set horizontal) after imposing a step-up shear rate from zero shear rate to 14.3 s^{-1} in Regime III for PS 548/DOP 6.0 wt % at 27.5 °C. The asymmetry of the patterns with respect to the horizontal axis is due to an artifact brought by the shape of the window employed for the temperature enclosure used in this experiment. From Ref. 97.

figure) clearly showed two overshoots at least, and even the third overshoot may be discerned at around 70 s on its approach toward quasi-steady state, as shown in Fig. 24. The first overshoots in σ occurred prior to that in N_1.[97] The structural origin of this intriguing rheological behavior was simultaneously followed up by the shear-LS method. The results are shown in the inset to Fig. 24.

The scattering intensity remains unchanged from that in quiescent solution even shortly after the first overshoot in N_1 (patterns a and b) but started to increase with time at about 15 s (pattern c), and then the butterfly pattern was clearly developed (patterns d to g). Its intensity parallel to flow direction (x axis) increases with time, while the intensity normal to flow direction (z axis) stays weak up to about 30 s, almost at the same intensity level as that for the quiescent solution, giving rise to the dark streak as discussed in the preceding section. The spread of this dark streak narrowed with time around z axis. The results indicate that amplitude of the concentration fluctuations increases with time and the Fourier modes of the fluctuations spread over a wider azimuthal angle μ with respect to flow direction. The intensity along the z axis tends to increase with time beyond 30 s after the onset of the flow, implying that the shear-induced phase separation starts to occur beyond 30 s. Thus, the transient change in the scattering patterns with time seems to be quite similar to the change in the steady-state scattering patterns with shear rate.

The butterfly pattern had a scattering maximum at the scattering vector q_m, its value slightly shifting toward a small q value with time over the q-range covered in this experiment (from $\sim$0.6 to $\sim 0.35 \times 10^{-3}$ nm^{-1}). Thus the characteristic length $2\pi/q_m$ of the shear-induced structure along flow varies from $\sim$10 μm to $\sim$18 μm. From right after the onset of the flow (0 s) to 50 s, the scattered intensity increased by more than 1 order of magnitude. The small-angle scattering patterns, especially the intensity parallel to flow, showed no appreciable changes with time beyond 50 s, indicating that the global dissipative structure had reached a steady-state.

Figure 24 reveals the following results. The butterfly patterns appear and hence shear-induced concentration fluctuations are formed at around the time when the stress levels of N_1 and σ reach near a valley in between the first and second overshoots. As time further elapses, both N_1 and σ increase toward the maximum values at the second overshoot and the butterfly pattern concurrently increases its scattered intensity and the butterfly wings spread over a wider azimuthal angle μ. Thus the rise of the stress level of N_1 and σ with time is related to the growth of the characteristic structures discussed in the preceding paragraph. At around the time when N_1 and σ reach or slightly pass through the peak of the second overshoot, the demixing may start to occur, which may be related to the increase of the intensity along q_z. The demixing appears to decrease the stress levels of N_1 and σ toward their steady values. As the stress levels approach the steady values, the global structures also appear to attain the steady structures at around point (f) in Fig. 24. These steady structures themselves were discussed in the preceding section. However, it may well be that the stress levels and the SALS intensity fluctuate around their steady values, because demixed structures will grow under flow but overgrown structures will be destroyed by the flow, and a dynamical balance between the growth and the destruction will give such fluctuations.

The stress increase in the first stress overshoot process is expected to arise from *uniform deformation* of entangled polymers and resulting orientation of polymer chains in the solution, as the SALS intensity showed no remarkable increase in intensity. The stress relaxation after the first stress overshoot process is expected to be accompanied by the squeezing of the solvent from the regions rich in polymer concentrations and hence to be associated with the building up of the concentration fluctuations against osmotic pressure. This process is responsible for developing the butterfly pattern. The relaxation time for the solvent squeezing process was more clearly elucidated also by large amplitude oscillatory shear flow experiments on the same experimental system.[70,71] In this experiment, the butterfly pattern was observed at strain amplitudes γ_0 greater than a critical value $\gamma_{0,c}$. At $\gamma_0 > \gamma_{0,c}$, the butterfly pattern was observed at angular frequency ω satisfying $\omega_{c,1} < \omega < \omega_{c,u}$ where $\gamma_0\omega_{c,1}$ corresponds to $\dot{\gamma}_{c,x}$ (and hence to Γ_{ve}) and $\gamma_0\omega_{c,u}$ corresponds to the relaxation rate for the solvent squeezing. At $\omega \geq \omega_{c,u}$ the entangled polymer solutions are uniformly stretched and uniformly relaxed under the oscillatory shear flow, giving rise to no concentration heterogeneities, simply because there would be no time available for solvents to be squeezed out in order to relax the stress for the deformed swollen entangled networks.

Even in the case when a step-up constant shear rate imposed to the system exceeds $\dot{\gamma}_a$, the structural evolution process occurs in the same manner as for the case of $\dot{\gamma}_{c,x} < \dot{\gamma} < \dot{\gamma}_a$ as discussed above, except for the fact that the system eventually attains the steady-state string-like structure in this case. Thus the replacement of row (A) by row (F) in Fig. 23: A set of the data from row (B) to (E) together with row (F) summarizes time evolution of LS patterns, OM images, form dichroism, birefringence, and N_1 after a step-up increase of $\dot{\gamma}$ from zero to a value larger than $\dot{\gamma}_a$. The time series of processes leading to the steady state can be summarized as follows:

(i) incubation period as shown in column (a), corresponding to the period involving the first stress overshoots, where entangled polymer chains in solutions are uniformly deformed and oriented, but to the period before the increased stress is relaxed by the solvent squeezing process;

(ii) an early stage of structure formation (column b) corresponding to the period between slightly after the first stress overshoot and before the second stress overshoot, where the shear-induced concentration fluctuations with the characteristic length scale of $\sim$10 μm is observed in the xz plane;

(iii) a late stage of structure formation (column c in the case of $\dot{\gamma} < \dot{\gamma}_a$) or (columns c and d in the case of $\dot{\gamma} > \dot{\gamma}_a$) corresponding to the period after the second stress overshoot being relaxed toward an average steady-state stress level where phase separation starts to occur, phase-separated structures grow and overgrown phase-separated structures are destroyed and the system eventually attained the (quasi) steady-state dissipative structures.

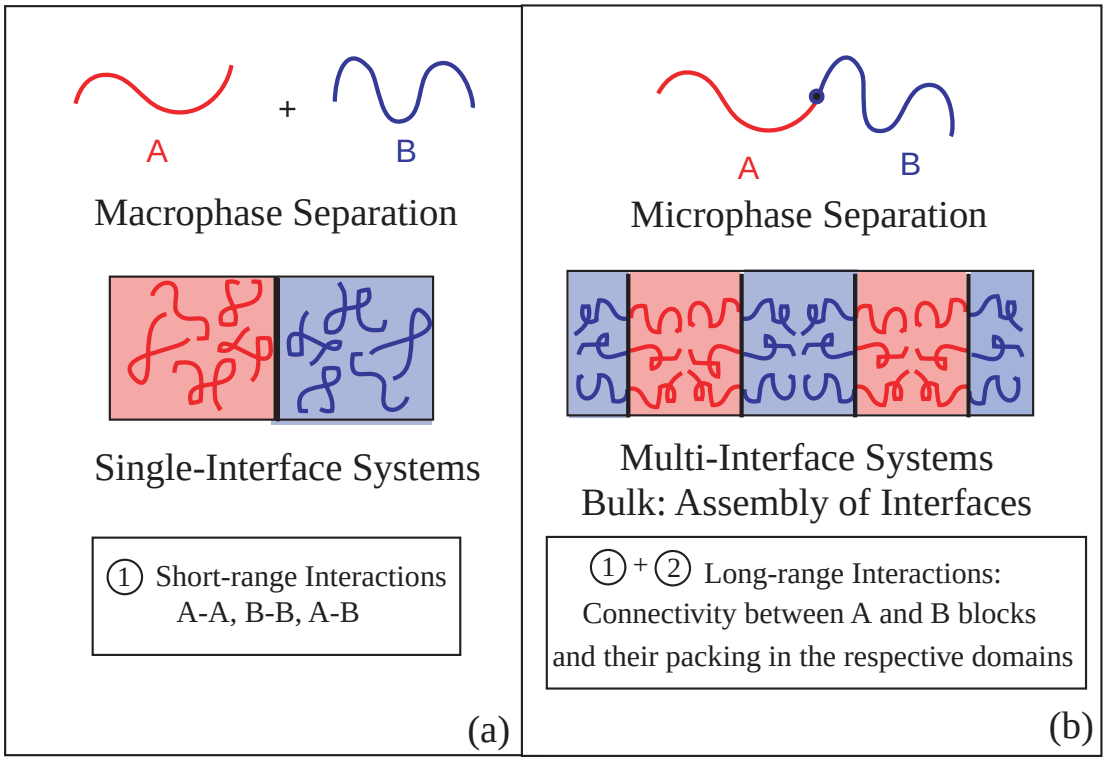

Fig. 25. Effects of connectivity between polymer A and B: (a) macrophase separation in polymer mixtures with a single interface and (b) microphase separation in block copolymers with a numerous number of interfaces.

5. Self-Assembly of Block Copolymer Systems

5.1 Roles of a Single Chemical Bond, Which Connects Different Block Polymers, on Self-Assembly. It is extremely interesting for us to realize that just a single covalent bond between a block polymer A and a block polymer B can strongly alter the physics of these two component polymer systems (see Fig. 25). Without a single covalent bond between polymers A and B (part a), the systems correspond to mixtures of polymers A and B and hence can achieve macrophase separation with a single, macroscopic interface at thermal equilibrium. We can visually recognize coexistence of the two macro-phase, rich in A and rich in B, as shown in Figs. 7b and 25a, if the optical properties of the two phases are sufficiently different. The important physical factors here is competing short-range interactions of segments between A and B, between B and B, and between A and B. On the other hand, with a single covalent bond between A and B (part b), the systems correspond to A-*b*-B block copolymers and can achieve only microphase separation in which the bulk is an assembly of numerous interfaces separating A and B microdomains or an assembly of monolayers of A-B block chains separating across the interface. Thus, in this case, the systems look homogeneous macroscopically but have locally periodic composition fluctuations of A and B.

It is very important to realize that the unique microphase-separated structure with long range order in A-*b*-B is a consequence of an interplay or competition of the short-range interactions inherent in the mixture and the long-range interactions of A and B inherent in A-*b*-B, which arises from the block connectivity and packing effects of A and B in the respective microphases.[98] The long-range interactions involve conformational entropy of block chains, inherent in polymer science. The interplay of these two interactions yields the ordered domain structures with various nano-sized units and symmetries such as face-centered cubic spheres,[99] body-centered cubic spheres (bcc-spheres), hexagonal cylinders (hex-cylinders), double gyroid network structure, or alternating lamellar structure of the microdomains, depending on a relative chain length of A and B blocks.[100]

Figure 26 demonstrates a typical transmission electron microscope (TEM) image obtained on ultrathin sections of a lamella-forming polystyrene (PS)-*block*-polyisoprene (PI) stained with osmium tetraoxide.[101] Small-angle X-ray scattering profiles showed up to the 10th order diffraction maximum, at least, indicating heterogeneity index of domain spacing D, $[HI]_D$, defined by Eq. 32 below is very small, much smaller than that of molecular weight distribution $[HI]_M = \bar{M}_w/\bar{M}_n \cong 1.1$.

$$[HI]_D \equiv \langle D^2\rangle/\langle D\rangle^2 = (\sigma_D/\langle D\rangle)^2 + 1 \cong 1.001. \qquad (32)$$

Thus the interplay of the interactions discussed above tends to compensate effects of molecular weight distribution on the domain size. We conclude that the microdomain structure has unique space-time characteristics: *macroscopically ordered solid* and hence *long-time scale solid-like behavior* but *microscopically disordered* and hence *short-time scale liquid like behavior* when A and B are amorphous polymers. For example chemical junctions of A-*b*-B block copolymers can undergo Brownian motions and hence transnational diffusion along the interfaces as in ordinary liquids, while keeping the long-range spatial order and hence the solid properties. This unique

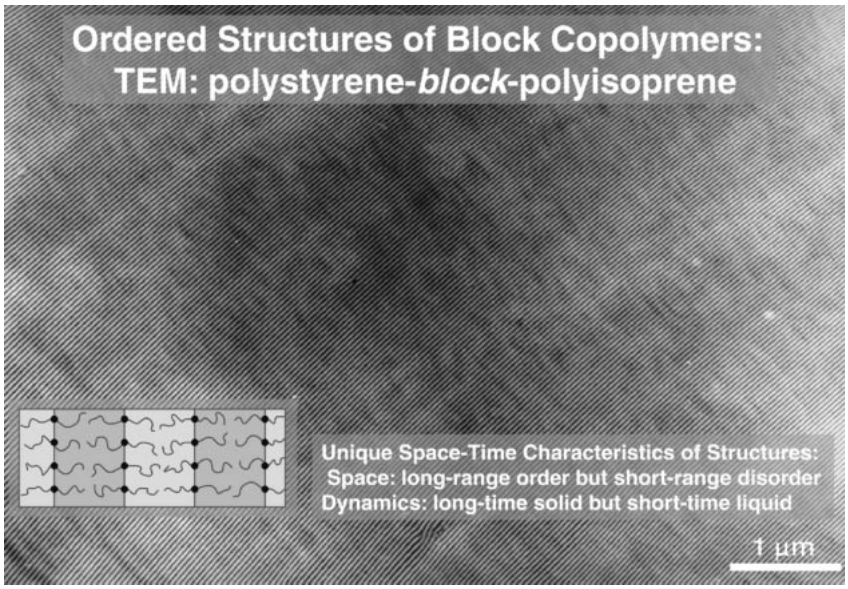

Fig. 26. Typical TEM image of PS-PI block copolymer films cast from a toluene solution (based on Ref. 101).

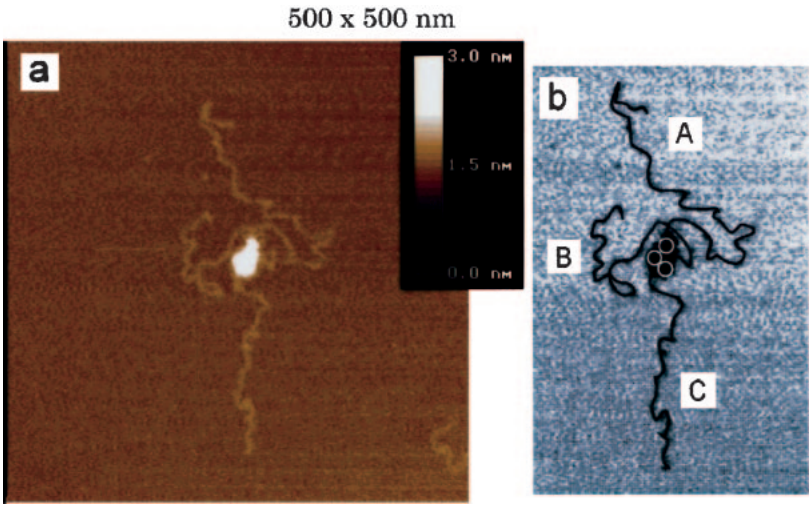

Fig. 27. Direct visualization of three expanded random-coils of PMMA block chains emanating from three PS globules, each of which is comprised of single PS block chains: (a) AFM image and (b) its sketch. From Ref. 103.

characteristics allow us to utilize the *microdomain space as* ***templates*** for further ***nanofabrications*** such as selective incorporations of metal nanoparticles and charge transfer complexes in one of the microdomain spaces, or selective transformation of one of the microdomains into void space, followed by non-electrolytic metal plating, etc.[102]

5.2 Self-Assembly in Neat Block Copolymers. Figure 27 presents a scanning probe microscope (SPM) image (a) and its sketch (b) for a self-assembled structure of three PS-*block*-poly(methyl methacrylate) (PMMA) chains on mica surface.[103,104] The bright object in the center of the image is comprised of 3 PS globules, as shown in the white circles in the sketch (b), where each globule is comprised of a single PS block chain. The three string-like objects, labeled A, B, and C in the sketch, emanating from the three globules are PMMA block chains expanded on the mica surface. The image presents, for the first time, evidence of direct visualization of isolated single chains of a synthetic polymer of ordinary molecular weight ($\bar{M}_n$ of PMMA 3.1×10^5). Thus the study made "conceptual reality" of random coil chains into "true reality" and hopefully will provide stimuli for further studies of visualization of sequence distribution of comonomers in copolymers and for fabrications of "molecular computers".

Direct visualization of isolated poly(2-vinyl pyridine)-*block*-polyisoprene (P2VP-PI) chains adsorbed by isolated palladium nanoparticles were also attained on the mica substrate by using SPM.[105] This promoted studies of configurations of polymer chains adsorbed on metal nano-particles (long tails and loops), stabilization mechanisms of adsorbed polymer chains against coagulation of the particles into larger clusters, and surface activities of the particles.

A series of fundamental works on ordered microdomain structures were conducted by using SAXS and TEM. The results elucidated the following important conclusions:[106] (i) The experimental results for the structures can be explained on the basis of equilibrium statistical mechanical theories in

the context of self-consistent mean-field approximation;[100] (ii) the existence of a very high degree of long-range ordered was elucidated by quantitative analysis of SAXS profiles;[101] (iii) relationships between the space-symmetry of the structures and the chemical compositions was elucidated;[107,108] (iv) a 2/3-power law of domain size vs molecular weight was found;[106] (v) the thicknesses of diffuse interfaces between the coexisting domains were successfully and quantitatively measured for the first time by using SAXS profiles;[106] (vi) equilibrium and nonequilibrium effects on microdomain formation and microdomain structures were clarified.[109] Figure 28 presents the average domain spacing $\bar{D}$ and the characteristic interfacial thickness t as a function of $\bar{M}_n$ of PS-PI diblock copolymers.[106]

Figure 29 represents the first cross-sectional TEM image reported in block copolymer publications. The image provided for the first time the following pieces of evidence:[110] (i) The lamellae comprised of block chains having a smaller surface tension value cover the air surface and (ii) these lamellae at the air surface have a thickness of one half of the thickness of lamellae in bulk. These situations were found to occur even in the case when the lamellae orient with their interfaces normal to the film surfaces. These findings gave fundamental information on subsequent and extensive studies of microdomain structures developed in very thin films.[111,112] In the thin film systems, the short-range interactions involve also interactions of air and substrate surfaces with block polymers A and B, and the long-range interactions also involve finite-size effects of space available to block copolymers in between the air and substrate boundaries. These extra interactions that are effective in thin films interplay among those inherent in bulk; such interplay is anticipated to give a richer variety in controlling structures and orientation of the microdomains in thin films,[113] compared to the case of bulk films.

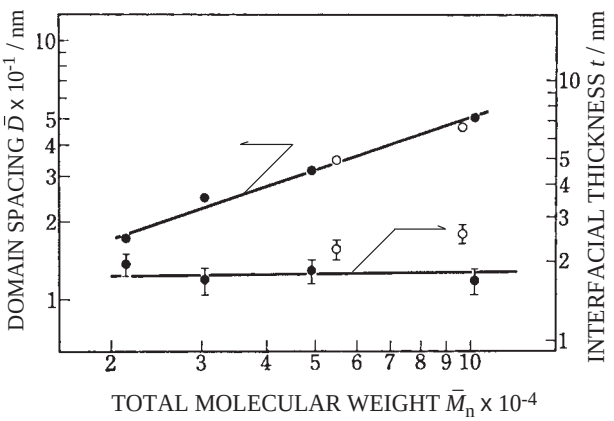

Fig. 28. The domain spacing $\bar{D}$ and the characteristic interfacial thickness t as a function of number average molecular weight for well annealed films prepared by solution-cast lamella-forming block copolymers (from Ref. 106).

5.3 Thermal Fluctuations' Effects on Phase Transitions: Order–Disorder and Order–Order Transitions. Thermal fluctuations are important for various pattern formations in nature, especially under the conditions where the thermodynamic driving forces for ordering of the systems under consideration closely balance with random thermal forces for disordering and randomization. The smaller the length scale of observation is, the more important are the effects. Brazovskii presented a general theory on the effects on phase transitions.[114] Unfortunately however the theory has not been extensively tested experimentally. We can experimentally explore this basic problem by using ***block copolymers as an ideal model system***, because the characteristic length of the system is small, of the order of molecular size $R_g \sim 10$ nm, but even so the dynamics are sufficiently slow. These two factors should enable us to precisely investigate the effects on phase transitions and ordering processes and mechanisms.

We established (i) the USAXS (ultra-small angle X-ray scattering) and SAXS method for characterization of order–disorder transition (ODT) of block copolymers.[115] We succeeded in visualization of (ii) the fluctuation-induced disordered structure (D_F)[115] and of (iii) anisotropic grains of ordered phases (lamellar and cylindrical phases) formed in the disordered matrix phase via a nucleation-growth (NG) process[116] induced by the fluctuation-induced first-order phase transition. We found (iv) the fluctuation-induced order–disorder coexistence over a narrow temperature region at ODT temperature[115] and anomalies in microscopic and macroscopic physical properties at the coexistence temperature region.[117,118] (v) The experimental results in (ii) to (iv) were verified by the computer simulations based upon the

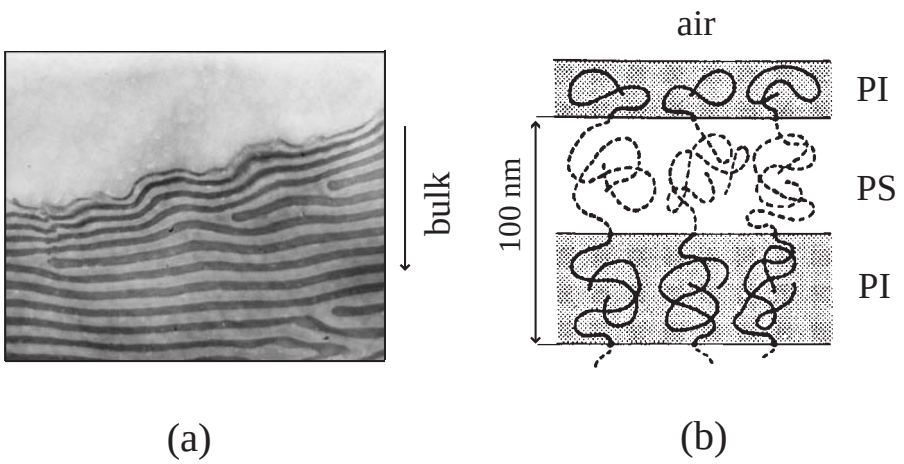

Fig. 29. Cross-sectional TEM image showing PS-PI lamellar morphology close to air surface (a) and its sketch (b) (from Ref. 110).

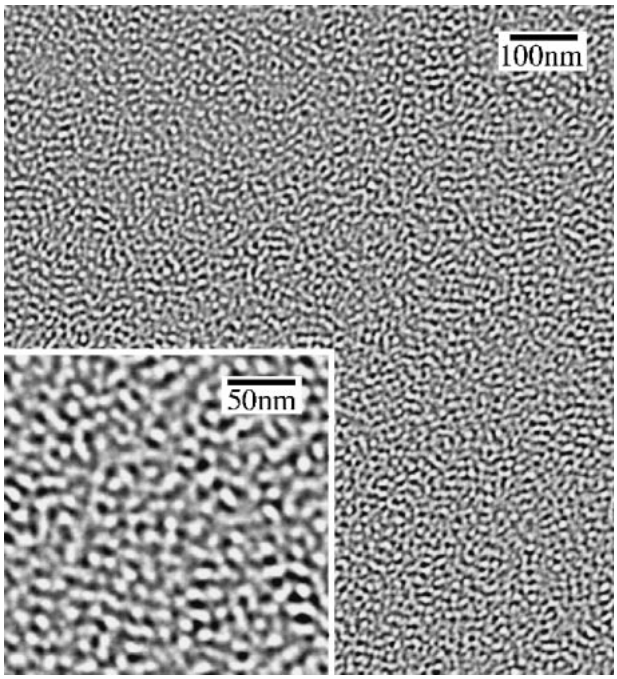

Fig. 30. TEM image showing a snap-shot of the thermal-fluctuation-induced disordered structures D_F for flash-freezing a lamella forming PS-PI melt in the disordered state close to T_{ODT} below its glass transition temperature. The SAXS profiles measured before and after the freezing confirmed no essential structure changes occurring in the freezing process (from Ref. 116).

Hohenberg–Swift theory.[115,119]

Figure 30 presents the D_F structure observed for a PS-PI diblock copolymer,[115,116] which was formed in the disordered state very close to the ODT temperature (T_{ODT}). This D_F structure was observed in the temperature region where well-ordered lamellae are predicted to exist in the context of the mean-field theory, which ignores the thermal fluctuations' effects. The bright and dark domains in the TEM image represent a snapshot of the vitrified D_F structures of the domains rich in PS and PI block chains unstained and stained with osmium tetraoxide, respectively. The inset shows a micrograph with a higher magnification. The domains reflect a frozen dynamical structure with no clear interfaces and without a long-range order.[116] The domains are developed and relaxed or exchange their positions one another with a characteristic time. Thus the thermal fluctuations transformed lamellae with long range order into the dynamical structure with only short range order.

Figure 31 represents an isolated ordered nuclei of lamellae developed in disordered phase having the D_F structures in the early stage of NG process.[116] The grain that developed after an induction period is highly anisotropic, having a prolate ellipsoidal shape with its long axis parallel to lamellar normal, because of some anisotropy of the interfacial tension between the ordered grain and disordered matrix. As time elapses, the number of the nuclei increases, resulting in the network-type ordered grains in the disordered phase. The ordered grains grow at the expense of the disordered phase to create volume filled anisotropic grains of the ordered lamellae.

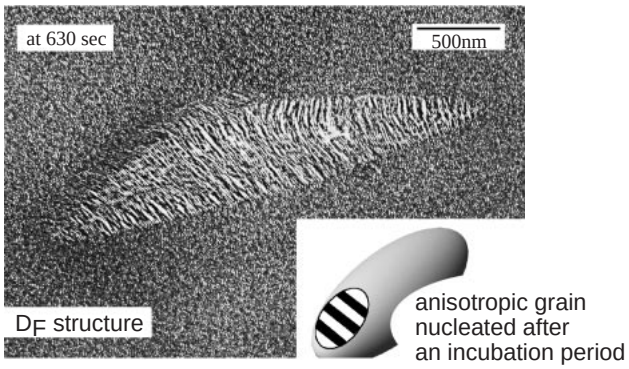

Fig. 31. Anisotropic grain of ordered lamellae nucleated in the D_F matrix as a consequence of the fluctuation-induced first-order phase transition (from Ref. 116).

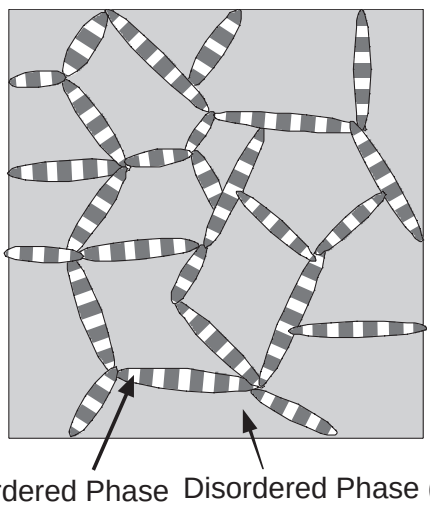

Fig. 32. Schematic illustration of coexistence of ordered lamellar networks and the disordered matrix having the D_F structure in the very narrow temperature region at T_{ODT} (Ref. 118).

Anomalies in the order–disorder coexistence region were found in such microscopic properties as (i) thermal diffuse scattering (TDS) at $q = 0$, which reflects isothermal compressibility or group velocity of acoustic phonons; (ii) up-turn of the USAXS intensity with decreasing q toward $q = 0$, which reflects the existence of long range density fluctuations; and (iii) the characteristic length $\Lambda_m = 2\pi/q_m$; as well as in such a microscopic property as (iv) the specific volume. All the anomalies were found to occur only in the coexistence region. Strikingly, the **ordering of PI-PS diblock copolymers** is analogous to the **ordering of water** into ice: the ordering causes an increase of volume. The ordering of block copolymers causes an increase of the long-range density fluctuations, which is also analogous to the vitrification process of water.

The USAXS profiles revealed the order–disorder coexistence at thermal equilibrium in the narrow temperature region at ODT temperature, and the TEM images on the vitrified specimens reveal a coexistence of network structure comprised of ordered lamellae phases with the disordered phase having the D_F structure, as schematically illustrated[118] in Fig. 32. There must be a small density difference between the two

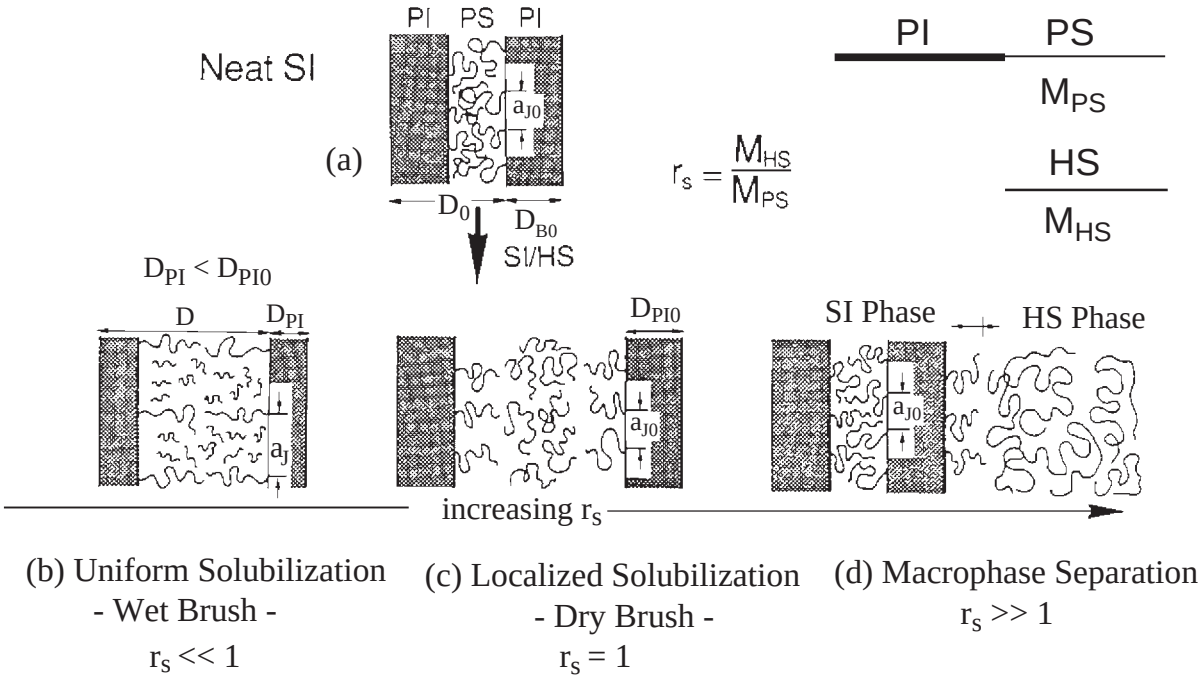

Fig. 33. Three criteria in self-assembly of molecular mixture of a PS-PI block copolymer (SI) and homopolystyrene (HS); (a) neat SI as a reference, and criteria of (b) wet brush, (c) dry brush, and (d) macrophase-separation (from Ref. 123).

phases which causes an upturn in USAXS profiles as $q \to 0$. The volume fraction of the ordered phase X is a function of T. These density fluctuations disappear when X goes to either 1 or 0. This may be a reason why the large scale density fluctuations occur only in the coexistence region. In the vitrification process of water, water molecules form **a temporal network of hydrogen-bondings**, while in our block copolymer systems, this network corresponds to **a temporal network of ordered phases**. Therefore, the two very different systems show an intriguing similarity. In summary, the various anomalies found in our experiments provide new intriguing fundamental problems in physical science.

Phase transitions among different ordered microdomains structures of block copolymers, which are called order–order transitions (OOT), occur by changing temperature. We discovered for the first time the thermally induced OOT of block copolymers, and we elucidated the mechanism and process of the OOT between bcc-spheres and hex-cylinders[120] and that between hex-cylinders and lamellae.[121] The studies triggered further extensive and elaborated studies of OOT involving double gyroid network structure with $Ia\bar{3}d$ space group symmetry,[100] which enriched the phase diagram of block copolymer systems in the parameter space of temperature (or χN, N being total DP of the block copolymers) and block composition f.

5.4 Mixtures Containing Block Copolymers: Micro- vs Macro-Phase Separation, Criterion for Wet Brushes, Dry Brushes, and Macrophase Separation, and Cosurfactant Effects. Addition of A-homopolymers (and/or B homopolymers) or another A-*b*-B block copolymers having different molecular weight and/or block composition into a given A-*b*-B block copolymer system alters only the long range interactions discussed in section 5.1. Hence the addition alters interplay between the short range and long range interactions, giving rise to important changes in the phase transitions and ordered microdomain structures.[122]

A. Block Copolymer/Homopolymer Systems: Figure 33 summarizes effects of polystyrene homopolymers (HS) on ordered structures of PS-PI (SI) block copolymers for the case where neat SI forms lamellae, as shown in part (a).[123] We for the first time elucidated that $r_s \equiv M_{HS}/M_{PS}$ is the most important parameter for the mixture where M_{HS} and M_{PS} are molecular weights of HS and PS block, and we obtained the following conclusions.

In the case when $r_s < 1$, HS's are more or less uniformly dissolved into the PS domain and thus swell the PS block chains, as shown in part (b).[124] Hence this criterion is called the "**wet brush**" criterion. The swelling involves expansion of PS domains both longitudinally and laterally with respect to the interfaces. The lateral expansion involves that of the average distance between chemical junction from a_{Jo} to a_J, which would then decrease PI lamellar thickness D_{PI} in order to satisfy the demand of incompressibility. In the wet brush criterion, the added HS increases the asymmetry of the volumes occupied by PS and PI block chains and hence causes increasing curvatures of the interface, leading to transitions from lamellae to double gyroid, hex-cylinder, bcc-spheres and eventually to micelles of PI with liquid-like short range order with increasing fraction of HS.

In the case when $r_s \cong 1$, homopolymers HS are solubilized into PS domains but the localized solubilization occurs preferentially in the middle of PS domains as shown in part (c).[125] HS's do not essentially swell PS brushes (block chains) emanating from the interface and therefore this criterion is called a "**dry brush**" criterion. In this case a_J remains equal to a_{Jo}, so that the PI lamellar thickness D_{PI} is kept equal to that of neat block D_{PIo}, and lamellar spacing D expands. As the amount of added HS increases and D expands, the individual PI lamellae have freedom to bend at the length scale larger

than their persistence length, just as in the case of bimolecular vesicles. Thus the system serves as **a good model system for cell membranes and membranes in surfactant systems**. Increasing asymmetry in the effective volumes occupied by PS and PI block chains would cause transformation from lamellar vesicles to cylindrical and spherical vesicles.[123]

In the case when $r_s \gg 1$, only a limited amount of HS can be solubilized into the PS domains, owing to a penalty of large conformational entropy loss of the solubilized HS chains, and a majority of HS is segregated out from the SI lamellae.[123] Consequently SI and HS undergo macrophase separation, as shown in part (d). We have elucidated various macrophase-separated structures.

B. Block Copolymer/Block Copolymer Systems: We elucidated for the first time that there are two criteria in the binary mixtures of A-*b*-B block copolymers of different block composition and/or molecular weights, designated (A-*b*-B)$_\alpha$ and (A-*b*-B)$_\beta$: one in which (A-*b*-B)$_\alpha$ and (A-*b*-B)$_\beta$ are molecularly mixed with each other and share common interfaces of a single microdomain and the other in which (A-*b*-B)$_\alpha$ and (A-*b*-B)$_\beta$ undergo macrophase separation.[126] In the former criterion, we found "**cosurfactant effects**":[127] The chemical junctions of minority block copolymers, e.g., (A-*b*-B)$_\alpha$, share the common interfaces formed by the majority block copolymers, e.g., (A-*b*-B)$_\beta$, and effectively change the interface curvatures and hence the morphology of domain structures of (A-*b*-B)$_\beta$. Such intriguing cosurfactant effects originate from competing long range interactions between α and β block copolymers in the microdomain space.

The cosurfactant effects can decrease or increase the interface curvatures, depending on systems, and provide a principle to decouple the morphology of microdomains and the overall composition of A and B. Figure 34 represents the case where the effects increase the interface curvature: specifically mixing of two lamella-forming block copolymers of (PI–PS)$_\alpha$ having $\bar{M}_n = 10^5$ and $f_{PS} = 0.47$, as shown in part (a), and (PI–PS)$_\beta$ having $\bar{M}_n = 1.45 \times 10^4$ and $f_{PS} = 0.46$, as shown in part (b), with blend composition of 60/40 wt %/wt % creates the hex-cylinder, as shown in part (c), even in the case when the overall PS weight fraction of the mixture is 0.47 and hence is a case where our intuition expects lamellar morphology.[127] Here again an important parameter is the ratio of molecular weights $r = \bar{M}_{n,\alpha}/\bar{M}_{n,\beta}$ and the molar ratio of $\alpha/\beta = 18/72$ mol/mol in the mixture. We found that the greater the value r is, the more effective are the cosurfactant effects.

Part (d) schematically illustrates the physics underlying in the cosurfactant effects. A slight asymmetry in the volume occupied by PS and PI block chains in the majority block copoly-

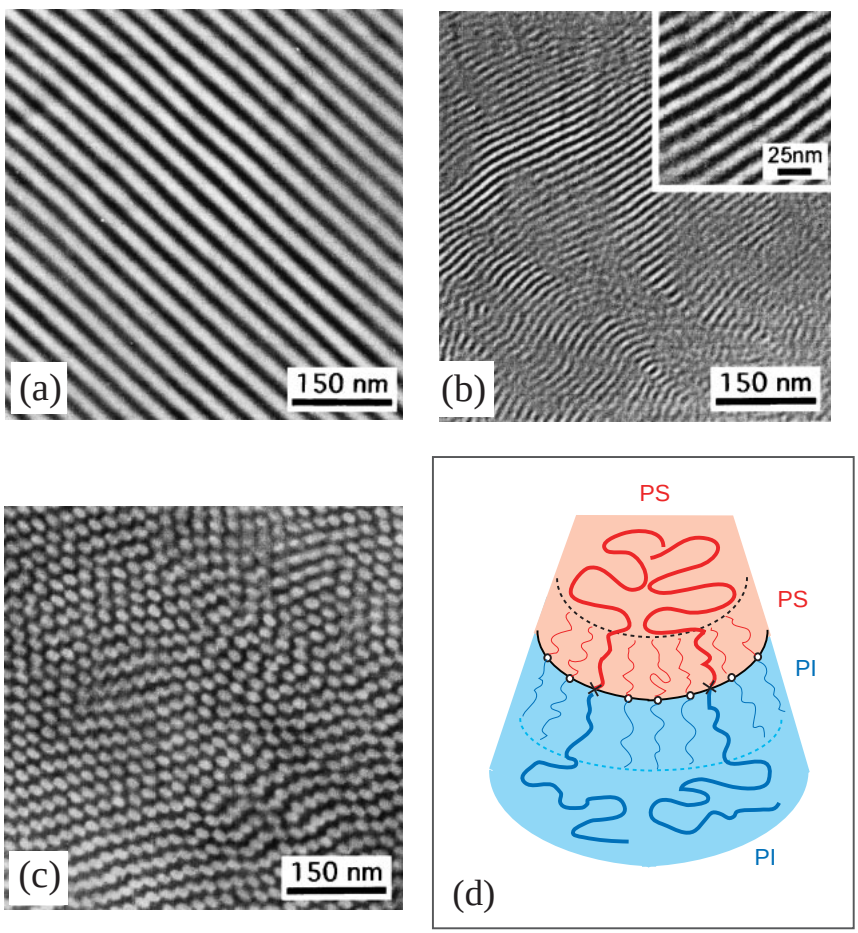

Fig. 34. TEM images showing a cosurfactant effect: A 60/40 wt %/wt % (or 18/72 mol%/mol%) mixture of lamella-forming PI-PS block copolymers (parts a and b) exhibited hex-cyl of PS in the marix of PI (part c). Part (d) explains the physical intuition for the cosurfactant effect. From Ref. 127.

mers $(PI–PS)_\beta$ having a shorter chain length tends to cause a spontaneous curvature of hex-cylinders of PS blocks. However, this curvature cannot be stabilized by the neat $(PI–PS)_\beta$ block copolymer itself, because the curvature creates a density deficiency in the central region of PS cylinders, if the PS block chains are not stretched to fill the central region and because either the density deficiency or the chain stretching involves free energy costs. However, the minority block copolymer $(PI–PS)_\alpha$ that has a longer chain length can stabilize the curvature by filling the empty space of the cylinder formed by the majority copolymer $(PI–PS)_\beta$, while keeping their stable chain conformations and the spontaneous curvature.

We have elucidated for the first time the criteria for the macrophase separation and microphase separation in the parameter space of r, blend composition, and temperature for the mixtures with their component block copolymers having symmetric block compositions,[126,128,129] i.e., $f_{PS,\alpha} \cong f_{PS,\beta} \cong 1/2$ as well as those having asymmetric block compositions,[130] $f_{PS,\alpha} \cong 1 - f_{PS,\beta} \neq 1/2$. Figure 35 demonstrates an intriguing commensuration found for a mixture with its component block copolymers having the symmetric block compositions.[126,131] The large PS and PI lamellae of $(PS–PI)_\alpha$ commensurate with the small PS and PI lamellae of $(PS–PI)_\beta$ at the macroscopic interface running diagonally in the TEM image in order to minimize the interfacial free energy. We found that small amounts of $(PS–PI)_\beta$ are solubilized in $(PS–PI)_\alpha$ lamellae but not vice versa,[126] which is a consequence of the competing long-range interactions discussed earlier in this section.

5.5 Nanoscience and Nanotechnology of Block Copolymers. We have been focusing on applications of block copolymers to **nanotechnologies**. Our objectives in the nanoscience of block copolymers here are to explore basic methods and principles concerning fabrications of ordered structures of block copolymers having the various symmetries with the nano-sized periodicity to create new materials with interesting structures and properties. We call this kind of fabrication as **nano-fabrication**. In other words we aim to utilize self-organized microdomain structures of block copolymers in bulk and in thin films as **templates**[102] for further nano-fabrications toward advanced devices and materials, such as tunable photonic crystals, quantum dots and nanowires, nanohybrids with inorganic materials, photovoltaics, and photoluminescence. We shall give below a brief summary on some of our researches along this line.

A. Vacant Nanochannels and Nanotexture: Figure 36 shows a computer graphics (CG) illustration of a repeat unit of the double gyroid structure constructed on the basis of differential geometry[38] (part a), its 3d cross-sectional image cut parallel to the (211) crystallographic plane (part b), and a typical image observed under a field-emission scanning electron microscopy (FE-SEM) on the freeze-fractured surface of ozone-degraded PS-PI block copolymer film (part c) having

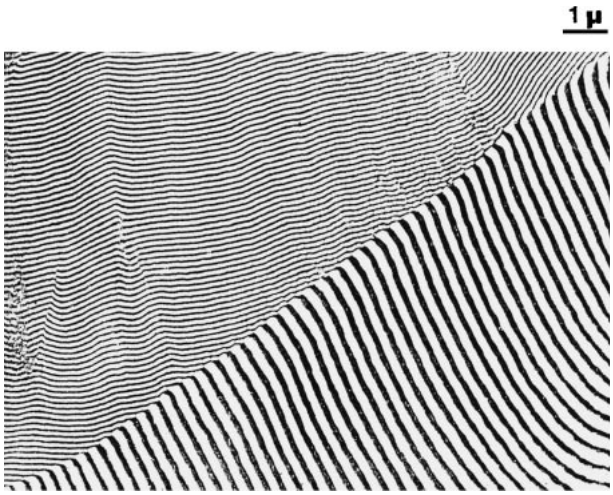

Fig. 35. TEM image showing a commensuration of the lamellar interfaces of the macrophase-separated lamellae of small (top-left half) and large molecular weight PS-PI block copolymers (bottom-right half) at the "macro-interface" running from the left-bottom to right-top corner of the figure (from Ref. 131).

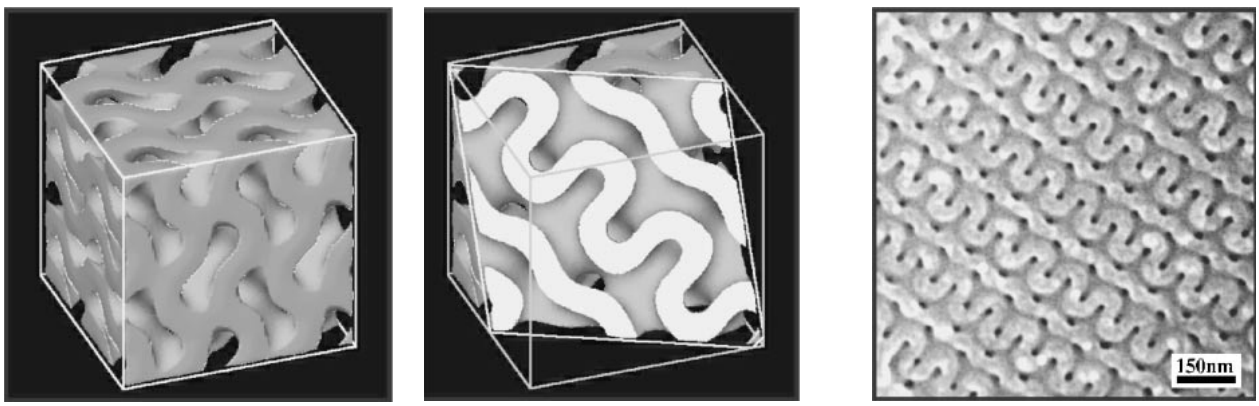

Fig. 36. Computer graphics of one-repeat unit of double groid network; (a) the network phase (bright phase) is made empty space and (b) shows a cross-section of (a) cut parallel to (211) plane where the area fraction of the matrix phase (bright phase) becomes minimum. Part (c) represents a typical FE-SEM image on the freeze-fractured surface of ozone degraded PS-PI block copolymer films having a double gyroid network structure. From Ref. 132.

the double gyroid structure comprised of PI blocks in the matrix of PS blocks.[132] In part (a), two sets of gyroid networks are made empty and appear bright, while the existing matrix phase appears dark. In part (b), the bright phase corresponds to the matrix, while the gray phase corresponds to the empty space made out of the double gyroid networks. The matrix phase indicates a set of bright waves with large and small amplitudes, periodically arranged perpendicular to the axes of the waves. The pattern (c) in the real world exactly reproduced the pattern predicted by the mathematical gyroid. Thus, we can conclude as follows: The ozonolysis selectively degraded the double gyroid network phase of PI blocks and transformed it into regular, vacant nano-channels with their volume fraction of 0.33, as shown in the CG in part (a). The plane on which the "double-wave" pattern appears turns out to be a cleavage plane which has a least area of the matrix phase, according to our computer analysis. Thus this pattern is the most probable pattern to be observed on the freeze-fracture surface of the specimens.

An interesting texture called "**nanotexture**" having double gyroid network structure can be created in empty space by selectively degrading the matrix phase of the structure.[133] The free-standing double networks may be stabilized in texture through its grain boundary structure.[102] The texture has a very large void fraction of 0.67.

B. Nanohybrids with Metal Nanoparticles: Figure 37 shows palladium nanoparticles (small dark dots having a diameter of about 5 nm) incorporated selectively into the P2VP lamellae (appearing dark in the TEM image) of the lamellar forming P2VP-PI diblock copolymers (part a) and the corresponding sketch of the nanohybrid (part b).[102] The PI lamellae appear bright because the TEM image was obtained on the unstained ultrathin sections. The nanohybrid was prepared by casting a solution of a small amount of P2VP-PS block copolymers that coordinate Pd nanoparticles, Pd–(P2VP-PS), and a large amount of the same P2VP-PS block copolymers that form the lamellar templates. In the pattern of part (c), the PI lamellae phase was further transformed into empty space by applying the ozonolysis to the system as follows. In order to attain a large concentration of Pd nanoparticles in the system as shown in part (c), we first subjected the films containing the lamellar morphology to the crosslinking reaction with diiodobutane, by which the P2VP lamellar phase is crosslinked, and then to the ozonolysis for the selective degradation of the PI lamellar phase. Then the films were soaked in benzene containing bis(acetoacetato)palladium, [Pd(acac)$_2$], and 1-propanol as a reducing agent of palladium; finally, the solution was refluxed at 85 °C for reduction of palladium ions.[133]

C. Tailoring Lamellar Orientation: Bulk Specimens: The tailoring of lamellar orientation was conducted by applying an external field in the ordering process of block copolymers from disordered melts both in bulk[134,135] and in thin films.[113] In the case of bulk block copolymer solids, we used moving temperature gradient (∇T) as the external field. Parts (a) and (b) in Fig. 38 schematically presents the conventional ordering process and the controlled ordering process under moving ∇T, respectively, while part (c) demonstrates a typical TEM image of the lamellar single crystal prepared under the ∇T field.

The conventional ordering involves a temperature drop from a temperature (T_u) (e.g., 190 °C) above T_{ODT}, where the systems are in the disordered melt (the left part of a), to a temperature (T_ℓ) (e.g., 5 °C) below T_{ODT}, where ordering occurs via NG and lamellar grains with a random orientation (the center part of a) grow into volume-filled polygrains of lamellae (the right part of a).[116] In this case, only the morphology of lamellae and the thickness of each lamella were chemically tailored by controlling the molecular weight of each block in polymerization chemistry.

On the contrary, "***super-tailoring***" of lamellae involves not only the "***chemical tailoring***" of block copolymer molecules themselves but also the "***physical tailoring***" of the ordering process via the moving ∇T field for example. We applied a large ∇T between T_u and T_ℓ over a narrow distance along z. In the left edge of part (b), the ∇T edge exists in the left hand side of the sample so that the whole sample is in the disordered melt. If the ∇T edge moves slightly toward the right hand side along the ∇T direction (z axis), the left edge of the sample is now brought into ordered state (see the middle illustration of

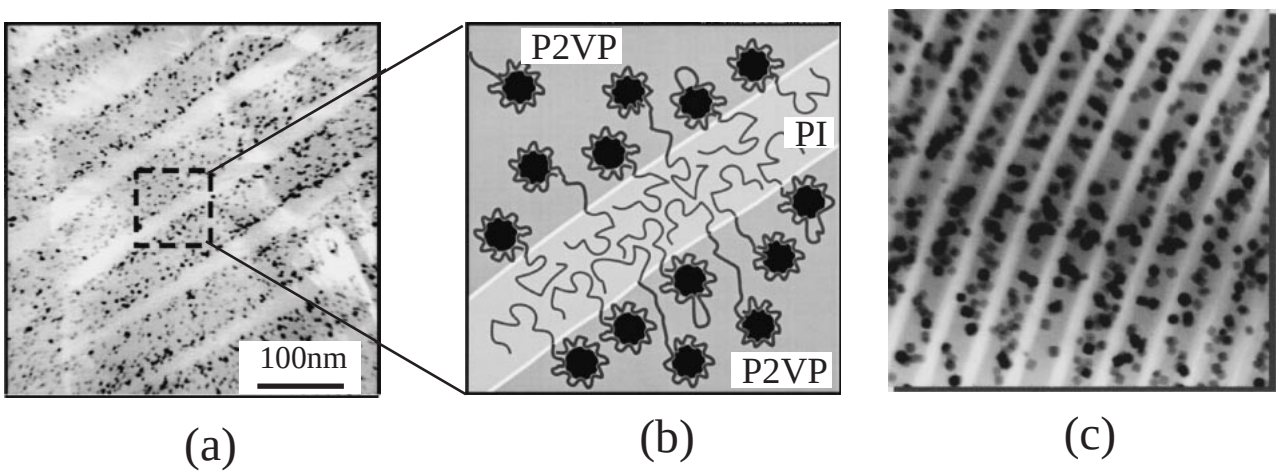

Fig. 37. TEM image showing nanohybrids of lamellar microdomains of PS-P2VP and Pd nanoparticles (a), and its sketch (b) showing Pd particles selectively coordinated by P2VP block chains and located in the P2VP lamellae. In part (c), the PI lamellae in part (a) were further transformed into empty space via ozone degradation of PI lamellae.

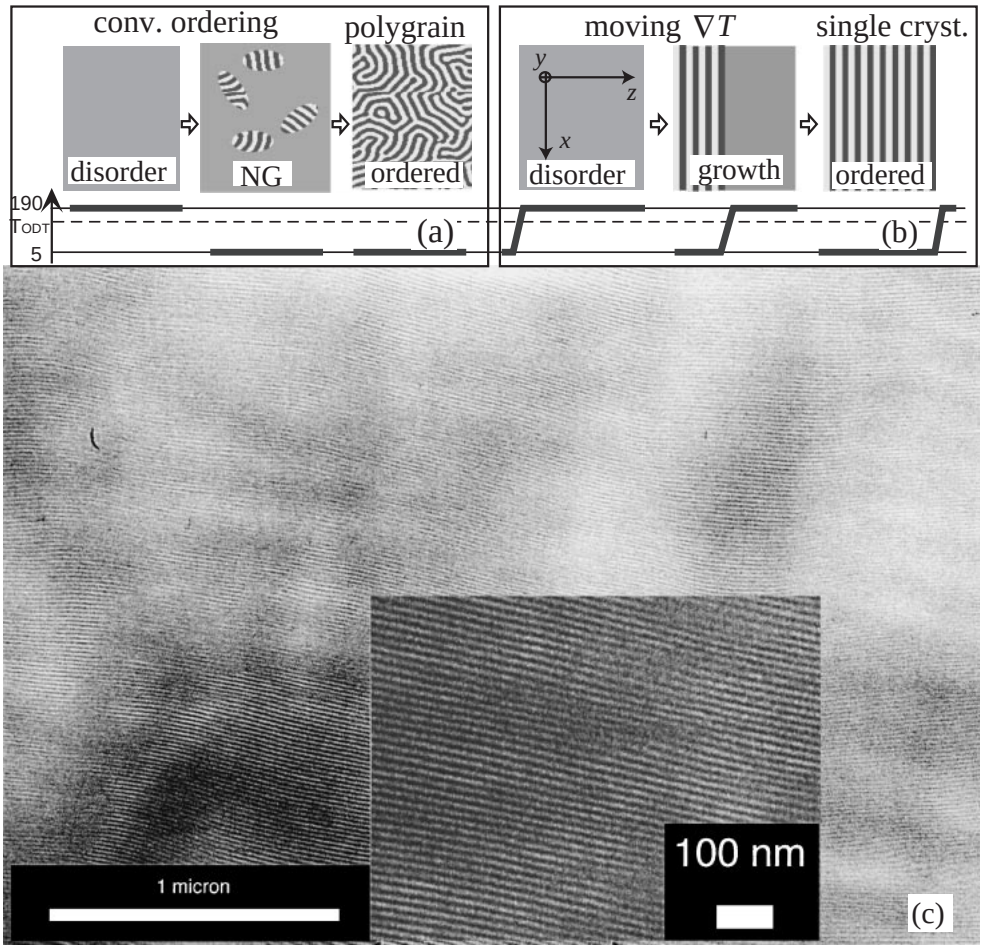

Fig. 38. Schematic representation of conventional ordering (a) and tailored ordering under a moving temperature gradient field (b). Part (c) shows a TEM image of a part of single crystal lamellae formed through the process (b). From Ref. 135.

part (b)). The ordering is forced to occur only in the narrow region whose temperature varies between T_ℓ and T_{ODT}, and this region moves more slowly than the characteristic growth rates of the lamellae from the left edge of the sample toward the right hand side of the sample along the z axis. The left edge of the sample contacts with a piece of glass with its smooth surface (xy plane) aligned normal to z axis. Under this situation, both the surface-directed ordering and the ∇T-directed ordering are coupled to orient the lamellae with the lamellar normals parallel to the z axis and with the lamellar interfaces perpendicular to the bulk film surface (xz-plane), as shown in the center part of part (b).[134] However the right hand side of the ∇T edge is still left at T_u and hence the specimen is kept in the disordered melt. As the ∇T edge moves along z, the growing lamellar front also moves accordingly to end up with formation of the lamellar single crystal as shown in the right part of (b).

The moving rate of the ∇T field should be smaller than the slowest growth rate of lamellae. Otherwise the sample in the left hand side of the ∇T edge could be left in the disordered state, although its temperature is lower than T_{ODT}, and hence such a conventional ordering as shown in part (a) might occur in this region. The lamellar single crystal obtained has a size of 6, 2, and 2 mm along x, y, and z axes, respectively, where x and y axes are set along width and thickness of the sample, respectively.

D. Tailoring Lamellar Orientation: Thin Film Specimens: In the case of thin films of lamella-forming block copolymers, we can think that roughness of the substrate could play a role for lamellar orientation, because the roughness affects both the short range and long range interactions and hence their competition and interplay.[98] We discovered, for the first time, that annealed PS-PMMA diblock copolymer thin films spun-cast on substrates, such as indium tin oxide, or polyimide, that have the roughness greater than the critical roughness $(q_0R)_c$ had "perpendicular lamellae" with the lamellar interfaces oriented perpendicular to the film surface.[113] On the contrary, the annealed thin films spun-cast on smooth substrates having the roughness smaller than $(q_0R)_c$ give "parallel lamellae" with their interfaces parallel to air and substrate surface. One can selectively introduce metal nanoparticles,[136] charge-transfer complexes,[137] etc. in one of the lamellae of the perpendicular orientation. Such patterns may have future applications as "**patterned media**" in order to create advanced opto-electronic devices with a superlarge memory density.

We may be able to interpret the role of the rough substrate on the lamellar orientation as follows. Figure 39 highlights the physical factors underlying the system. We consider the following case: (i) The short range interactions between the substrate and the block chains are sufficiently weak, yet the sub-

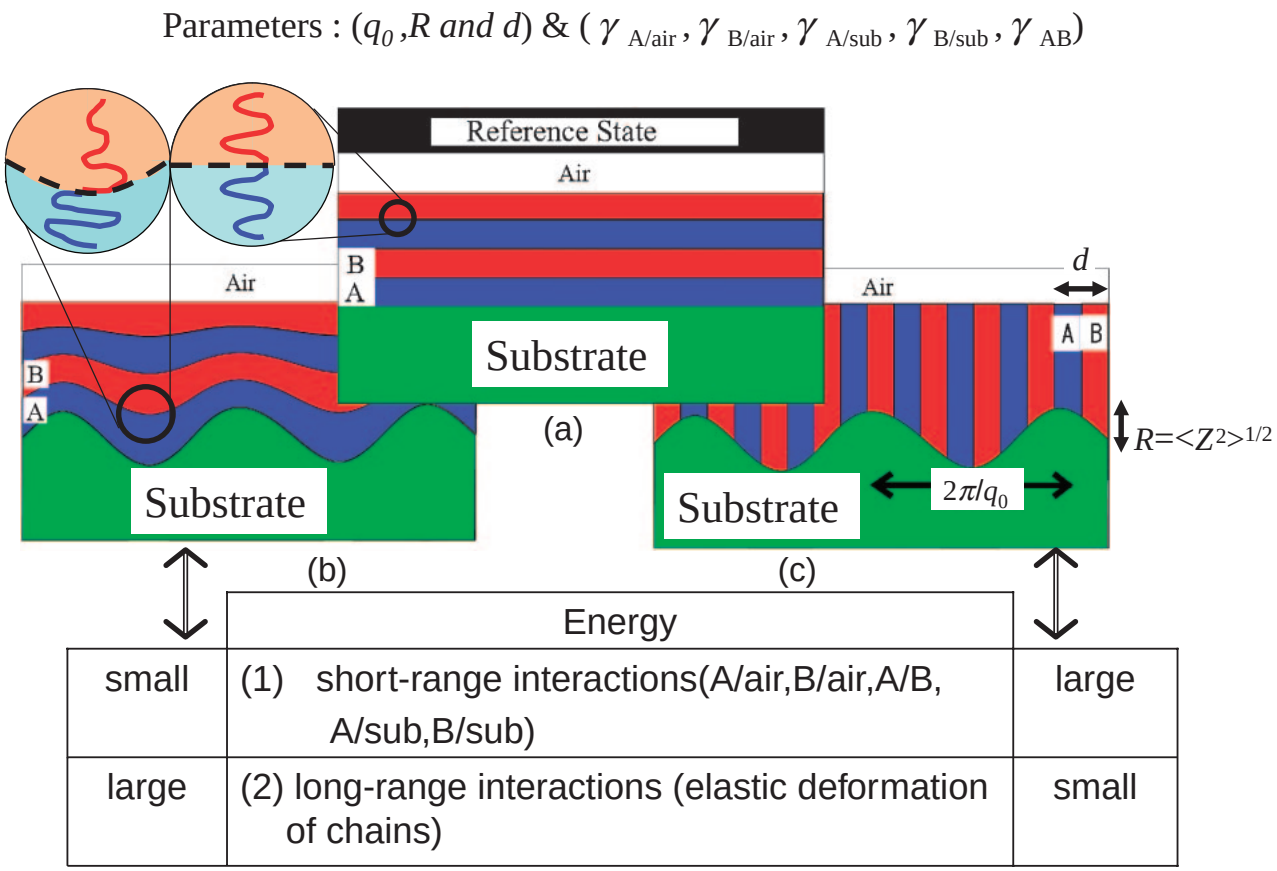

Fig. 39. Effects of surface roughness of substrates on lamellar orientation of spun-cast block copolymer thin films.

strate selectively favors one of the lamellae (e.g., A) due to competitive short-range interactions between A/substrate ($\gamma_{A/sub}$) and B/substrate ($\gamma_{B/sub}$), where $\gamma_{K/sub}$ (K = A or B) is interfacial tension; (ii) The substrate has a roughness as characterized by a root-mean squared amplitude of roughness R and a characteristic wave number q_0. We compare the free energy of the following two systems on a rough substrate: system (b) having parallel lamellar orientation with a wavy lamellar interface in order to follow the topography of the rough substrate and system (c) having perpendicular lamellar orientation with the straight lamellar interface. The comparisons are made relatively to a reference system (a) where the parallel lamellae exist on the smooth substrate. In system (b), the short range interactions are small, because of A blocks with $\gamma_{A/sub} < \gamma_{B/sub}$ covering substrate, but the long-range interactions are large because of the bending of the lamellae, which causes elastic deformation of block chains and hence a cost of the elastic energy. On the contrary, in system (c), the short-range interactions are large because of a contribution of $\gamma_{B/sub}$ but the long-range interactions are small. As R increases for a given q_0, the free energy cost due to the elastic deformation becomes larger than that due to the short-range energetic interactions, which would then cause the perpendicular lamellae (b) to become more stable than the parallel lamellae (c). This happens for the substrate with R larger than the critical roughness R_c. In more detail, short range interactions with air ($\gamma_{K/air}$, K = A or B) as well are generally important. Here it is important to note that the monomolecular layer of block chains (e.g., B) having a lower surface tension covers the air surface regardless of the lamellar orientation. The lamellar orientation in thin films can be controlled by a balance of various parameters, q_0, R, and d (lamellar spacing) as well as $\gamma_{K/air}$ and $\gamma_{K/sub}$, as summarized in Fig. 39, which gives enormous flexibilities in the orientation control.

Figure 40 presents a through view image of TEM on the annealed spun-cast PS-PMMA thin films (part a) on the rough substrate, where the PS and PMMA lamellae have perpendicular orientations as schematically shown in part (c). The dark dots are palladium nanoparticles selectively introduced into PS lamellae microdomains that appear gray. The bright microdomains in part (a) are PMMA lamellae. The nanoparticles are prepared by reduction of [Pd(acac)$_2$] via exposition of the thin films with sublimated [Pd(acac)$_2$] at 200 °C, as schematically shown in Fig. 40c. The small bright particles in the AFM image of part (b) correspond to Pd particles on the surface of the PS domains. The particles were found to be created both on the surface and in the interior of the PS lamellae.

6. Summary and Perspectives

Figure 41 schematically summarizes the work presented here and possible future directions. We presented a part of our studies on the ***mechanics*** (dynamics, kinematics, and statics) ***of molecular assembly*** of *soft matters* both under quiescent state and shear flow as one of the *external fields*. The systems under quiescent state represent those of *thermally equilibrium systems*, while the systems under shear flow represent

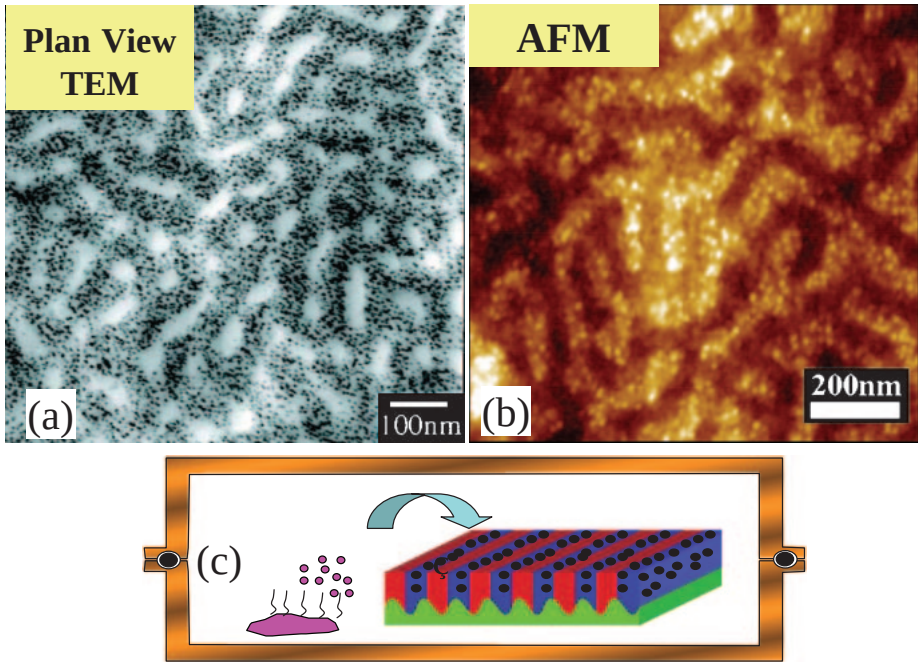

Fig. 40. Through view TEM image (a) and AFM image (b) of perpendicular lamellae of PS-PMMA block copolymer thin films in which Pd nanoparticles were selectively incorporated in the PS lamellae. The particles are incorporated by sublimation of $Pd(acac)_2$ into the PS-PMMA films and in-situ reduction at 200 °C, as shown in part (c).

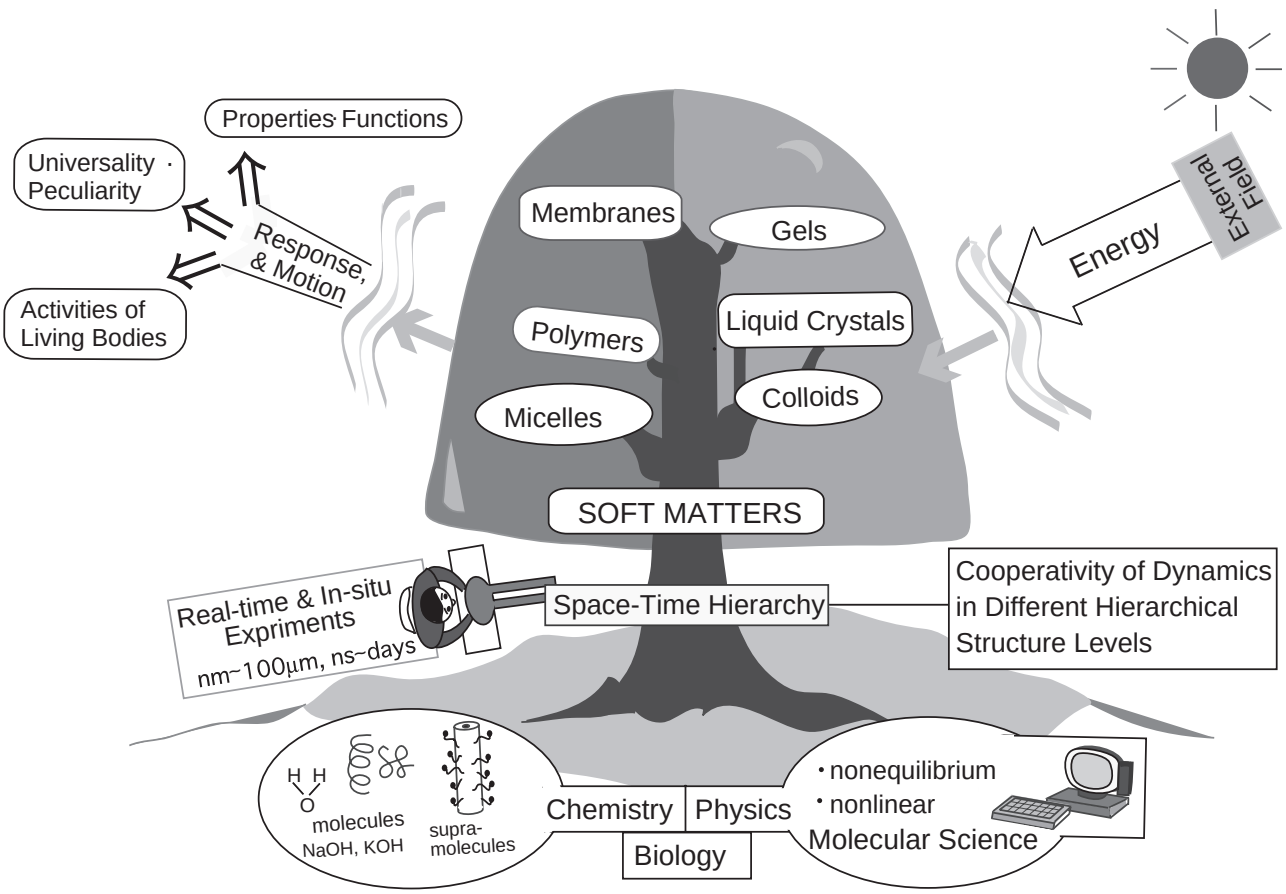

Fig. 41. Summary of present studies and perspectives of mechanics of molecular assembly in soft matters.

those of *open nonequilibrium systems*. We presented summaries of a series of our works on *real-time and in-situ* analyses on response and motion of *space-time hierarchy* of molecular assembly in various systems. We hope these studies will promote basic understanding of properties and of soft matters, the universality and peculiarity underlying the responses and motions of various soft-matters, and eventually the principles of activities of living bodies and organisms. Especially clarification of principles underlying cooperativity of dynamics in different hierarchical structure levels is believed to be among the most important future problems in soft-matter science. All these researches are concerned with one of the non-equilibrium and non-linear phenomena left to be clarified in this new century, and can be considered as an interdisciplinary area of chemistry, physics, and biology. In each of the three systems covered in secs. 3 to 5, we highlighted polymer systems that provide good model systems for deep explorations and understandings of non-equilibrium and non-linear phenomena in small molecule systems.

References

1 A. Silverberg and W. Kuhn, *J. Polym. Sci.*, **13**, 21 (1954).
2 G. Ver Strate and W. Phillipoff, *J. Polym. Sci., Polym. Lett. Ed.*, **12**, 267 (1974).
3 D. Beysens and M. Gbadamassi, *J. Phys. Lett.*, **40**, L565 (1979).
4 M. Szwarc, M. Levyy, and R. Milkovich, *J. Am. Chem. Soc.*, **78**, 2656 (1956).
5 J. W. Cahn and J. E. Hilliard, *J. Chem. Phys.*, **29**, 258 (1958).
6 J. W. Cahn, *J. Chem. Phys.*, **42**, 93 (1965).
7 H. E. Cook, *Acta Metall.*, **18**, 297 (1970).
8 J. D. Gunton, M. San Miguel, and P. S. Sahni, "Phase Transitions and Critical Phenomena," ed by C. Domb and J. Lebowitz, Academic Press, N.Y. (1983), Vol. 8, p. 269.
9 L. D. Landau and E. M. Lifshitz, "Statistical Physics," Pergamon, New York (1964).
10 T. Hashimoto, "Materials Science and Technology," ed by R. W. Cahn, P. Haasen, and E. J. Kramer, "Vol. 12, Structure and Properties of Polymers," Vol. ed by E. L. Thomas, VCH, Weinheim (1993), Chap. 6, p. 251.
11 P. J. Flory, "Principles of Polymer Chemistry," Cornell University Press, Ithaca, N.Y. (1967).
12 Y. C. Chou and W. I. Goldburg, *Phys. Rev. A*, **23**, 858 (1981).
13 K. Binder and D. Stauffer, *Phys. Rev. Lett.*, **33**, 1006 (1974).
14 T. Hashimoto, M. Itakura, and N. Shimidzu, *J. Chem. Phys.*, **85**, 6773 (1986).
15 T. Hashimoto, *Phase Transitions*, **12**, 47 (1988).
16 H. Jinnai, H. Hasegawa, T. Hashimoto, and C. C. Han, *Macromolecules*, **24**, 282 (1991).
17 P. G. de Gennes, "Scaling Concept in Polymer Physics," Cornell University, Ithaca (1979).
18 M. Doi and S. F. Edwards, "The Theory of Polymer Dynamics," Clarendon Press, London (1986).
19 J. D. Ferry, "Viscoelastic Properties of Polymers," Wiley, N.Y. (1980).
20 P. G. de Gennes, *J. Chem. Phys.*, **72**, 4756 (1980).
21 P. Pincus, *J. Chem. Phys.*, **75**, 1996 (1981).
22 K. Binder, *J. Chem. Phys.*, **79**, 6387 (1983).
23 A. Z. Akcasu, *Macromolecules*, **22**, 3682 (1989).
24 M. Takenaka, T. Izumitani, and T. Hashimoto, *J. Chem. Phys.*, **92**, 4566 (1990).
25 T. Hashimoto, H. Jinnai, H. Hasegawa, and C. C. Han, "Proceeding of the Fifth International Symposium on Advanced Nuclear Energy Research, Neutron as Microscopic Probes," Mito, Japan, March (1993).
26 T. Hashimoto, H. Jinnai, H. Hasegawa, and C. C. Han, *Physica A*, **204**, 261 (1994).
27 T. Hashimoto, K. Koga, H. Jinnai, and Y. Nishikawa, *IL Nuovo Cimento*, **20**, 1947 (1998).
28 Y. C. Chou and W. I. Goldburg, *Phys. Rev. A*, **20**, 2105 (1979).
29 N.-C. Wong and C. M. Knobler, *Phys. Rev. A*, **24**, 3205 (1981).
30 C. M. Knobler and N.-C. Wong, *J. Phys. Chem.*, **85**, 1972 (1981).
31 T. Koga and K. Kawasaki, *Physica A*, **196**, 389 (1993); T. Koga, K. Kawasaki, M. Takenaka, and T. Hashimoto, *Physica A*, **198**, 473 (1993).
32 K. Kawasaki and T. Ohta, *Progr. Theor. Phys.*, **59**, 362 (1978).
33 J. S. Higgins and H. C. Benoit, "Polymers and Neutron Scattering," Clarendon, Oxford (1994).
34 S. Sakurai, H. Jinnai, H. Hasegawa, T. Hashimoto, and C. C. Han, *Macromolecules*, **24**, 4839 (1991).
35 T. Hashimoto, *J. Polym. Sci., Part B: Polym. Phys.*, **42**, 3027 (2004).
36 T. Hashimoto, M. Takenaka, and H. Jinnai, *J. Appl. Cryst.*, **24**, 457 (1991).
37 H. Jinnai, Y. Nishikawa, H. Morimoto, T. Koga, and T. Hashimoto, *Langmuir*, **16**, 4380 (2000).
38 S. Hyde, K. Anderson, K. Larsson, Z. Blum, T. Landh, S. Lidin, and B. W. Ninham, "The Language of Shape," Elsevier, Amsterdam (1997).
39 T. Hashimoto, H. Jinnai, Y. Nishikawa, and T. Koga, *Macromol. Symp.*, **190**, 9 (2002).
40 T. Hashimoto, H. Jinnai, Y. Nishikawa, T. Koga, and M. Takenaka, *Progr. Colloid Polym. Sci.*, **106**, 118 (1997).
41 T. Koga, H. Jinnai, and T. Hashimoto, *Physica A*, **236**, 369 (1999).
42 B. Kirste and G. Porod, *Kolloid-Z.Z. Polym.*, **184**, 1 (1962).
43 H. Tomita, *Progr. Theor. Phys.*, **72**, 656 (1984).
44 K. Kumano, H. Jinnai, and T. Hashimoto, unpublished results.
45 Y. Hirokawa, H. Jinnai, Y. Nishikawa, T. Okamoto, and T. Hashimoto, *Macromolecules*, **32**, 7093 (1999).
46 S. H. Chen, D. D. Lee, K. Kimishima, H. Jinnai, and T. Hashimoto, *Phys. Rev. E*, **54**, 6526 (1996).
47 H. Jinnai, T. Hashimoto, D. Lee, and S. H. Chen, *Macromolecules*, **30**, 130 (1997).
48 H. Jinnai, Y. Nishikawa, S. H. Chen, S. Koizumi, and T. Hashimoto, *Phys. Rev. E*, **61**, 6773 (2000).
49 T. Hashimoto and N. Mitsumura, unpublished results.
50 T. Hashimoto, T. Izumitani, and K. Oono, *Macomol. Symp.*, **98**, 925 (1995).
51 M. Teubner and R. Strey, *J. Chem. Phys.*, **87**, 3195 (1987).
52 S. H. Chen, D. D. Lee, and S. L. Chang, *J. Mol. Struct.*, **296**, 259 (1993).
53 A. Onuki, "Phase Transition Dynamics," Cambridge Univ. Press., Cambridge, UK (2002).

54 H. Yoshida, N. Ise, and T. Hashimoto, *J. Chem. Phys.*, **103**, 10146 (1995).
55 B. V. Derjaguin and L. Landau, *Acta Physiochim.*, **14**, 633 (1941).
56 E. J. W. Verwey and J. Th. G. Overkeek, "Theory of the Stability of Lyophobic Colloids," Elsevier, Amsterdam (1948).
57 H. Tanaka, *Macromolecules*, **25**, 6377 (1992).
58 N. Toyoda, M. Takenaka, S. Saito, and T. Hashimoto, *Polymer*, **42**, 9193 (2001).
59 M. Takenaka, H. Takeno, H. Hasegawa, S. Saito, T. Hashimoto, and M. Nagao, *Phys. Rev. E*, **65**, 021806-1 (2002).
60 T. Izumitani and T. Hashimoto, *J. Chem. Phys.*, **83**, 3694 (1985).
61 M. Doi and A. Onuki, *J. Physique II*, **2**, 1631 (1992).
62 A. Onuki, *J. Non-Crystalline Solids*, **172**, 1151 (1994).
63 S. K. Ma, "Modern Theory of Critical Phenomena," Benjamin-Cummings, MA (1976).
64 T. Hashimoto, T. Takebe, and S. Suehiro, *Polym. J.*, **18**, 123 (1986).
65 T. Kume, K. Asakawa, E. Moses, K. Matsuzaka, and T. Hashimoto, *Acta Polym.*, **46**, 79 (1995).
66 T. Hashimoto, S. Okamoto, K. Saijo, K. Kimishima, and T. Kume, *Acta Polym.*, **46**, 463 (1995).
67 S. Suehiro, K. Saijo, T. Seto, N. Sakamoto, T. Hashimoto, K. Ito, and Y. Amemiya, *J. Synchrotron Rad.*, **3**, 225 (1996).
68 K. Matsuzaka and T. Hashimoto, *Rev. Sci. Instr.*, **70**, 2387 (1999).
69 S. Saito, T. Hashimoto, I. Morfin, P. Lindner, and F. Boue, *Macromolecules*, **35**, 445 (2002).
70 S. Saito, K. Matsuzaka, and T. Hashimoto, *Macromolecules*, **32**, 4879 (1999).
71 S. Saito, S. Koizumi, K. Matsuzaka, S. Suehiro, and T. Hashimoto, *Macromolecules*, **33**, 2153 (2000).
72 T. Takebe, K. Fujioka, R. Sawaoka, and T. Hashimoto, *J. Chem. Phys.*, **93**, 5271 (1990).
73 T. Hashimoto, T. Takebe, and K. Fujioka, "Dynamics and Patterns in Complex Fluids," ed by A. Onuki and K. Kawasaki, Springer, Berlin (1990), p. 86.
74 T. Hashimoto, K. Matsuzaka, and K. Fujioka, *J. Chem. Phys.*, **108**, 6963 (1998).
75 T. Hashimoto, T. Takebe, and S. Suehiro, *J. Chem. Phys.*, **88**, 5874 (1988).
76 K. Matsuzaka, T. Koga, and T. Hashimoto, *Phys. Rev. Lett.*, **80**, 5441 (1998).
77 T. Hashimoto, K. Matsuzaka, E. Moses, and A. Onuki, *Phys. Rev. Lett.*, **71**, 126 (1995).
78 T. Hashimoto, T. Takebe, and K. Asakawa, *Physica A*, **194**, 338 (1993).
79 T. Takebe, R. Sawaoka, and T. Hashimoto, *J. Chem. Phys.*, **91**, 4369 (1989).
80 T. Kume and T. Hashimoto, "Flow-Induced Structure in Polymers," ACS Symp. Series, 597 (1995), p. 35.
81 S. Tomotika, *Proc. Roy. Soc. London*, **150**, 322 (1935).
82 L. S. Ornstein and Z. Zernike, *Proc. Akad. Sci. (Amsterdam)*, **17**, 783 (1914); *Phys. Z.*, **19**, 134 (1918); *Phys. Z.*, **217**, 761 (1926).
83 R. Schmidt and B. A. Wolf, *Colloid Polym. Sci.*, **257**, 1187 (1979).
84 C. Rangel-Nafaile, A. B. Metzner, and K. F. Wissbrun, *Macromolecules*, **17**, 1187 (1984).
85 H. Kramer and B. A. Wolf, *Makromol. Chem. Rapid Commun.*, **6**, 21 (1985).
86 T. Hashimoto and K. Fujioka, *J. Phys. Soc. Jpn.*, **60**, 356 (1991).
87 X.-L. Wu, D. J. Pine, and P. K. Dixon, *Phys. Rev. Lett.*, **66**, 2408 (1991).
88 T. Hashimoto and T. Kume, *J. Phys. Soc. Jpn.*, **61**, 1839 (1992).
89 I. Morfin, P. Lindner, and F. Boue, *Macromolecules*, **32**, 7208 (1999).
90 E. Moses, T. Kume, and T. Hashimoto, *Phys. Rev. Lett.*, **72**, 2037 (1994).
91 M. Endo, S. Saito, and T. Hashimoto, *Macromolecules*, **35**, 7692 (2002).
92 S. Saito and T. Hashimoto, *J. Chem. Phys.*, **114**, 10531 (2001).
93 H. Murase, T. Kume, T. Hashimoto, Y. Ohta, and T. Mizukami, *Macromolecules*, **28**, 7724 (1995).
94 T. Kume, T. Hashimoto, T. Takahashi, and G. G. Fuller, *Macromolecules*, **30**, 7232 (1997).
95 H. Murase, Y. Ohta, and T. Hashimoto, submitted to *Macromolecules*.
96 A. J. Pennings and A. M. Kiel, *Kolloid Z. Z. Polym.*, **205**, 160 (1965); A. Keller and M. J. Machin, *J. Macromol. Sci. Phys.*, **B1**, 41 (1967).
97 T. Kume, T. Hattori, and T. Hashimoto, *Macromolecules*, **30**, 427 (1997).
98 T. Hashimoto, K. Yamauchi, D. Yamaguchi, and H. Hasegawa, *Macromol. Symp.*, **201**, 65 (2003).
99 Y.-Y. Huang, H.-L. Chen, and T. Hashimoto, *Macromolecules*, **36**, 764 (2003).
100 I. Hamley, "The Physics of Block Copolymers," Oxford Univ. Press, Oxford (1988).
101 T. Hashimoto, H. Tanaka, and H. Hasegawa, *Macromolecules*, **18**, 1864 (1985).
102 T. Hashimoto and H. Hasegawa, *Trans. Mater. Res. Soc. Jpn.*, **29**, 77 (2004).
103 J. Kumaki, Y. Nishikawa, and T. Hashimoto, *J. Am. Chem. Soc.*, **118**, 3321 (1996).
104 J. Kumaki and T. Hashimoto, *J. Am. Chem. Soc.*, **125**, 497 (2003).
105 T. Hashimoto, A. Okumura, and D. Tanabe, *Macromolecules*, **36**, 7324 (2003).
106 T. Hashimoto, M. Shibayama, and H. Kawai, *Macromolecules*, **13**, 1237 (1980).
107 T. Inoue, T. Soen, T. Hashimoto, and H. Kawai, *J. Polym. Sci., A2*, **7**, 1283 (1969).
108 H. Hasegawa, H. Tanaka, K. Yamasaki, and T. Hashimoto, *Macromolecules*, **20**, 1651 (1987).
109 T. Hashimoto, M. Shibayama, and H. Kawai, *Macromolecules*, **16**, 1093 (1983).
110 H. Hasegawa and T. Hashimoto, *Macromolecules*, **18**, 589 (1985).
111 A. Menelle, T. P. Russell, S. H. Anastasiadis, S. K. Satija, and C. F. Majkvzak, *Phys. Lev. Lett.*, **68**, 67 (1992).
112 P. Mansky, O. K. C. Tsui, T. P. Russell, and Y. Gallot, *Macromolecules*, **32**, 4832 (1999).
113 E. Sivaniah, Y. Hayashi, M. Iino, T. Hashimoto, and K. Fukunaga, *Macromolecules*, **36**, 5894 (2003).
114 S. A. Brazovskii, *Soviet Phys. JETP*, **41**, 85 (1975).
115 T. Hashimoto, T. Koga, T. Koga, and N. Sakamoto, "The Physics of Complex Liquids," ed by F. Yonezawa, K. Tsuji, K. Kaji, M. Doi, and T. Fujiwara, World Sci., Singapore (1998), p. 291.

116 N. Sakamoto and T. Hashimoto, *Macromolecules*, **31**, 3815, 8493 (1998).
117 T. Koga, T. Koga, and T. Hashimoto, *J. Chem. Phys.*, **110**, 11076 (1999).
118 T. Hashimoto, *Macromol. Symp.*, **174**, 69 (2001).
119 G. H. Hohenberg and J. B. Swift, *Phys. Rev. E*, **52**, 1828 (1995).
120 S. Sakurai, H. Kawada, T. Hashimoto, and L. J. Fetters, *Macromolecules*, **26**, 5796 (1993).
121 S. Sakurai, T. Momii, K. Taie, M. Shibayama, S. Nomura, and T. Hashimoto, *Macromolecules*, **26**, 485 (1993).
122 H. Hasegawa and T. Hashimoto, "Comprehensive Polymer Science," Second Supplement, ed by S. R. Aggarwal and S. Russo, Pergamon (1996), Chap. 14, p. 497.
123 S. Koizumi, H. Hasegawa, and T. Hashimoto, *Makromol. Chem. Macromol. Symp.*, **62**, 75 (1992).
124 H. Tanaka, H. Hasegawa, and T. Hashimoto, *Macromolecules*, **24**, 240 (1991).
125 T. Hashimoto, H. Tanaka, and H. Hasegawa, *Macromolecules*, **23**, 4378 (1990).
126 T. Hashimoto, K. Yamasaki, S. Koizumi, and H. Hasegawa, *Macromolecules*, **26**, 2895 (1993).
127 T. Hashimoto, D. Yamaguchi, and F. Court, *Macromol. Symp.*, **195**, 191 (2003).
128 D. Yamaguchi and T. Hashimoto, *Macromolecules*, **34**, 6495 (2001).
129 D. Yamaguchi, H. Hasegawa, and T. Hashimoto, *Macromolecules*, **34**, 6506 (2001).
130 S. Koizumi, H. Hasegawa, and T. Hashimoto, *Macromolecules*, **27**, 4371, 6532 (1994).
131 T. Hashimoto, S. Koizumi, and H. Hasegawa, *Macromolecules*, **27**, 1562 (1994).
132 T. Hashimoto, K. Tsutsumi, and Y. Funaki, *Langmuir*, **13**, 6869 (1997).
133 M. Adachi, A. Okumura, E. Sivaniah, and T. Hashimoto, to be submitted.
134 T. Hashimoto, J. Bodycomb, Y. Funaki, and K. Kimishima, *Macromolecules*, **32**, 952 (1999).
135 J. Bodycomb, Y. Funaki, K. Kimishima, and T. Hashimoto, *Macromolecules*, **32**, 2075 (1999).
136 E. Sivaniah, S. Matsubara, H. Kitano, and T. Hashimoto, unpublished results.
137 T. Matsushita, H. Hasegawa, and T. Hashimoto, *Kobunshi Ronbunshu*, **59**, 669 (2002).

Takeji Hashimoto received degrees from Kyoto University (B.S. in 1965 and M.S. in 1967 with Prof. H. Kawai) and from the University of Massachusetts (M.S. in 1969 and Ph.D in 1971 with Prof. R. S. Stein). After postdoctoral work with Prof. R. S. Stein, he was appointed as a Research Associate in 1971 in the Faculty of Engineering, Kyoto University and was promoted to Full Professor in 1994. Since then he has been in the same Faculty and University. He was a director of the Hashimoto Polymer Phasing Project, ERATO, JST from 1993 to 1998. He has been appointed as a group leader and invited researcher for the Project, "Neutron Scattering and Structure-Functionality of Soft Matters" at Advanced Science Research Center, Japan Atomic Energy Research Institute, Tokai, since 2003. His awards include The Soc. Polym. Sci. Jpn Award (1986), The High Polymer Physics Award (Ford Prize) from the Am. Phys. Soc. (1987), The Award for Young Rheologist, Soc. Rheology, Jpn (1989), The Soc. Fiber Sci. Jpn Award (1990), The Osaka Science Award (1992), The Chemical Society of Japan Award (2002), The Turner Alfrey Award from Midland Molecular Inst., Midland Section of ACS, The Fraser Price Memorial Award from Univ. Massachusetts (2003), and The Japanese Society for Neutron Science Award (2004).